

Volume-based electrodes for enhancing limiting currents in electrochemical conversion reactions

Ligthart, N.E.G.

DOI

[10.4233/uuid:78652653-76d9-49bb-bcee-31cf5a91cb8d](https://doi.org/10.4233/uuid:78652653-76d9-49bb-bcee-31cf5a91cb8d)

Publication date

2025

Document Version

Final published version

Citation (APA)

Ligthart, N. E. G. (2025). *Volume-based electrodes for enhancing limiting currents in electrochemical conversion reactions*. [Dissertation (TU Delft), Delft University of Technology].
<https://doi.org/10.4233/uuid:78652653-76d9-49bb-bcee-31cf5a91cb8d>

Important note

To cite this publication, please use the final published version (if applicable).
Please check the document version above.

Copyright

Other than for strictly personal use, it is not permitted to download, forward or distribute the text or part of it, without the consent of the author(s) and/or copyright holder(s), unless the work is under an open content license such as Creative Commons.

Takedown policy

Please contact us and provide details if you believe this document breaches copyrights.
We will remove access to the work immediately and investigate your claim.

VOLUME-BASED ELECTRODES

for enhancing limiting currents in electrochemical
conversion reactions

Nathalie van der Plas-Ligthart

**VOLUME-BASED ELECTRODES FOR ENHANCING
LIMITING CURRENTS IN ELECTROCHEMICAL
CONVERSION REACTIONS**

VOLUME-BASED ELECTRODES FOR ENHANCING LIMITING CURRENTS IN ELECTROCHEMICAL CONVERSION REACTIONS

Proefschrift

ter verkrijging van de graad van doctor
aan de Technische Universiteit Delft,
op gezag van de Rector Magnificus Prof. dr. ir. T.H.J.J. van der Hagen,
voorzitter van het College voor Promoties,
in het openbaar te verdedigen op
maandag 10 februari 2025 om 12:30 uur

door

Nathalie Elsa Gertrude LIGTHART

Master of Science in Chemische Wetenschappen,
Universiteit Utrecht, Nederland
geboren te Leiden, Nederland

This dissertation has been approved by the promotor.

Composition of the doctoral committee:

Rector Magnificus	chairperson
Prof. dr. ir. J.T. Padding	Delft University of Technology, promotor
Dr. ir. D.A. Vermaas	Delft University of Technology, promotor

Independent members:

Prof. dr. V. Garbin	Delft University of Technology, Netherlands
Prof. dr. ir. J.R. van Ommen	Delft University of Technology, Netherlands
Dr. R. Kortlever	Delft University of Technology, Netherlands
Prof. dr. V. Presser	Saarland University / INM - Leibniz Institute for New Materials, Germany
Dr. B.H. Ern�	Utrecht University, Netherlands

This project has received funding from the European Research Council (ERC) under the European Union's Horizon 2020 research and innovation programme (Grant agreement No 852115). This work reflects the authors' view and the ERC Executive Agency is not responsible for any use resulting from the information it contains.



Keywords: mass transfer limitation, volume-based electrode, suspension electrode, flow-through electrode, electrochemical conversion

Printed by: Proefschriftspecialist

Front & Back: Nathalie E.G. Ligthart

Copyright   2025 by N.E.G. Ligthart

ISBN 978-94-93391-95-6

An electronic version of this dissertation is available at
<http://repository.tudelft.nl/>.

CONTENTS

1	General introduction	1
1.1	The need for electrifying our society	1
1.2	Challenges in applying electrochemical systems	2
1.3	Existing technologies are complicated to scale up.	3
1.4	Our concept: volume-based electrodes	3
1.5	Thesis outline and research questions	5
	References	7
2	Practical potential of suspension electrodes	11
2.1	Introduction	13
2.2	Concept.	14
2.3	Methods	16
2.3.1	Modelling	16
2.3.2	Experiments	17
2.4	Results and Discussion	19
2.4.1	Ratio of reaction and conduction resistances is key in electrode utilization.	19
2.4.2	Particle size and shape impact conductivity and flowability trade-off	20
2.4.3	AC and CB give good modelled reaction distributions	23
2.4.4	Suspension electrodes show low selectivity for CO ₂ reduction	24
2.5	Conclusions.	26
2.6	Supporting Information.	28
	References	39
3	Combining flow-through, suspensions, and surfactants	45
3.1	Introduction	47
3.2	Methods	48
3.3	Results and discussion	48
3.4	Implications and conclusions.	51
3.5	Supporting Information.	53
	References	58
4	Boosting limiting currents with flow-through electrodes	63
4.1	Introduction	65
4.2	Methods	66
4.3	Results and Discussion	68
4.3.1	Flow-through configuration improves the H ₂ O ₂ production.	68
4.3.2	Electrode configuration and flow conditions enhance mass transfer.	70

4.3.3	Catalyst concentration and stability	72
4.3.4	AC suspensions break down H_2O_2	72
4.3.5	Comparing limiting current densities to Sherwood correlations . . .	74
4.3.6	Implications for scale up	76
4.4	Conclusions.	78
4.5	Supporting Information.	80
	References	87
5	Imaging concentration boundary layers at 3D electrodes	91
5.1	Introduction	93
5.2	Methods	94
5.3	Results and discussion	95
5.3.1	Boundary layer and plume formation	96
5.3.2	Concentration profile near the particle	100
5.3.3	Capacitance-driven Faradaic reactions	101
5.4	Conclusions.	105
5.5	Supporting Information.	107
	References	116
6	Conclusions	121
	Summary	127
	Samenvatting	131
	Acknowledgements	135
	Curriculum Vitæ	137
	List of Publications	139

1

GENERAL INTRODUCTION

1.1. THE NEED FOR ELECTRIFYING OUR SOCIETY

The negative impact of our large-scale use of fossil fuels and chemicals on the environment is driving our need to decarbonize society and accelerate the energy transition. Although sustainable alternatives are emerging for many applications, such as electric cars and heat pumps to reduce the use of petrol and natural gas, many energy-intensive and environmentally unfriendly industrial processes and essential hydrocarbons cannot be discarded, nor are they easy to replace. Here, one could think of fuel for cargo ships or planes, precursors for carbon-based products (*e.g.* paints, pharmaceuticals, plastics), or synthesis processes of vital chemicals like fertilizers or disinfectants. Replacing such processes and chemicals by green alternatives is an ongoing challenge and will be crucial for mitigating the climate crisis.

Electrochemistry can provide a direct bridge between renewable electricity and material synthesis, and it can aid in the transition from our carbon-based industry to an electrified green industry. Electrochemistry uses electrons, which can be generated from renewable sources, to drive reactions or other processes to provide a sustainable alternative to established industrial processes. A well-known example is water electrolysis to produce hydrogen as a green fuel, but electrochemical systems can be used for many more applications such as ammonia production[1, 2], energy storage[3, 4], water desalination[5], and (microbial) fuel cells[6, 7].[8]

Two specific processes are studied in this thesis.

1. Electrochemical carbon dioxide (CO_2) reduction, used to produce carbon-based chemical compounds (CO , CH_4 , CH_3OH etc.) that are otherwise obtained from fossil fuels. Converting and utilizing CO_2 that has been captured from the atmosphere through direct air-[9] or oceanic[10] capture closes the carbon cycle and lowers CO_2 emissions while it enables us to continue using conventional fuels and materials.[11]

2. The oxygen reduction reaction (ORR), which is a sustainable method for hydrogen peroxide (H_2O_2) production. H_2O_2 is a green oxidant in high and increasing demand for use in a wide variety of applications, including chemical synthesis[12], advanced water treatment methods[13], and fuel cells[14].[15] The currently used production process for H_2O_2 is highly energy-intensive, environmentally unfriendly, and in great need of replacement by a green alternative such as the electrochemical ORR.[16]

1.2. CHALLENGES IN APPLYING ELECTROCHEMICAL SYSTEMS

Although they are promising, electrochemical processes are challenging to industrialize due to the high benchmarks posed to achieve economic viability and to become cost competitive with current established processes. Keeping with the example of CO_2 electrolysis, a CO_2 electrolyzer should have a Faradaic efficiency (FE) of at least 95% at high current densities of at least 200 mA/cm^2 while operating at a low cell potential of maximum 3 V[17], and being able to operate at these standards for several years to be considered economically viable.[18–20] Some of these requirements can be fulfilled at lab scale, but they are hard to maintain in larger systems.

Water-based electrochemical systems offer the advantages of easily achieved ionic conductivity, separation of gaseous products, and heat management, but they suffer from low solubility and slow diffusion of reagents. The reagents used in these technologies, including CO_2 and O_2 electrolyzers, are often gases and are poorly soluble in aqueous electrolytes, which results in very low reagent concentrations in the bulk. The consumption rate at the electrode increases with the applied current density, and the reagent concentration at the catalyst surface decreases accordingly when diffusion towards the electrode is slower, as shown in Figure 1.1. This intensifies competition with undesired parasitic reactions, such as the hydrogen evolution reaction (HER) in the case of aqueous CO_2 reduction, at higher current densities.

The highest current that can be achieved, the limiting current density, is thus often dependent on how fast the reagent can be resupplied to the surface. This depends on its mass transfer rate from the bulk (where the concentration is at its maximum) to the surface (where the concentration is low). How fast this transport is, depends on the distance that needs to be travelled (the diffusion boundary layer thickness) and the concentration difference that drives diffusion across this distance.

The limiting current density is therefore highly dependent on reagent solubility and mass transport. In aqueous CO_2 reduction, the typical diffusion boundary layer thickness is in the order of 100-1000 μm and the maximum concentration of CO_2 at atmospheric pressure is 34 mM. This combination of a thick diffusion boundary layer with such low solubility leads to a limiting current density of only 2 mA/cm^2 in systems that rely on forced convection and diffusion.[21] This is considerably lower than the required 200 mA/cm^2 . Significant improvements are needed to realize economically viable systems.

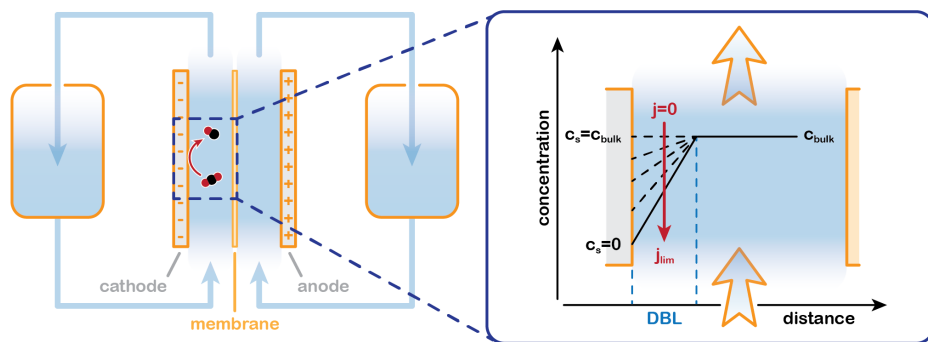


Figure 1.1: Schematic of an aqueous CO₂ electrolyzer and a zoom-in, showing the influence of increasing the applied current density (j) on the concentration gradient inside the diffusion boundary layer (DBL) and on the resulting surface concentration (c_s) of the reagent. The limiting current density (j_{lim}) is reached when $c_s = 0$ M.

1.3. EXISTING TECHNOLOGIES ARE COMPLICATED TO SCALE UP

Some systems that overcome mass transfer limitations are currently under development. These systems usually employ a Gas Diffusion Electrode (GDE), in which the low solubility and slow mass transport are resolved by feeding the reagent in the gas phase instead of dissolved in an electrolyte.[22, 23] The gas is flowed past a hydrophobic porous electrode that prevents flooding and allows gas to pass through to reach catalytically active particles that are deposited on the other side. This significantly increases the reagent flux towards the active surface and boosts the achievable current density and FE as a result.

Although the results are promising, these systems are delicate and difficult to scale to industrially relevant proportions due to multiple issues. Especially water management[24, 25] and stability issues pose challenges. These include flooding due to the difference in hydrostatic pressure over the porous GDE and electrowetting[24–26], salt formation[27], electrode degradation[26], and drying out of ionic separators[28, 29]. These challenges in gas-fed systems, and the intrinsic advantage of stable water management and salt control in aqueous-based systems, inspired us to search for an alternative route for mitigating mass transfer limitations, while providing a more robust and scalable system.

1.4. OUR CONCEPT: VOLUME-BASED ELECTRODES

In this thesis, we study a new strategy to boost the limiting current: by bringing the catalyst towards the reagent instead of depending on slow mass transfer towards the electrode. We achieve this by extending the electrode deeper into the channel, which brings both the current and the catalyst deeper into the channel. This effectively increases the amount of available reagent, not by raising its concentration, but by involving a larger electrolyte volume in the reaction compared to when a planar electrode is used. Ideally, the electrolyte over the full thickness of the channel is close enough to the electrode to allow reaction in the entire channel volume, indicated by the red shaded area in Figure 1.2

(right). For comparison, conventional electrochemical flow cells have a planar electrode incorporated at the edge of the channel, along which the electrolyte is flowing. Only the reagent molecules in a thin layer of electrolyte are close enough to reach the electrode and react during their passing, see Figure 1.2 (left).

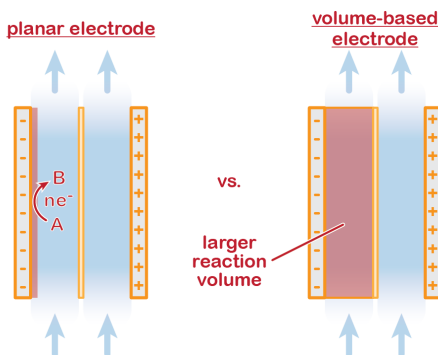


Figure 1.2: A planar electrode (left) results in a significantly smaller reaction volume (red shaded area) than a volume-based electrode (right) that spans over the entire channel depth.

To achieve a larger reaction volume, the electrically conductive material must be extended into the channel while the ionic conductivity is maintained as well. We can realize such a volume-based electrode in various ways: with 1) a flow-through (foam-based, Figure 1.3a), or 2) a flow-with (suspension-based, Figure 1.3b) electrode concept. Both concepts consist of a solid electrically conductive phase that is surrounded by an ionically conductive electrolyte, but differ in the nature of the solid phase. In the flow-through concept, the solid phase is composed of a continuous porous foam through which an electrolyte is flowed. In the flow-with concept, the solid phase consists of discrete electrically conductive microparticles that are suspended in the flowing electrolyte. The entire suspension is pumped through the system and the suspended microparticles temporarily form conductive networks as they pass a current collector.

Flow-through electrodes are used in several existing technologies, such as redox flow batteries[3, 30, 31], water treatment[32], and water electrolysis[33], and offer multiple advantages. Flow-through electrodes have excellent electric conductivity and their large surface to volume ratio offers much larger catalytic surface area than planar electrodes. This improves electrode-electrolyte contact, and lowers local current densities.[34, 35] Additionally, the porous nature of the foam shortens the mass transfer distances[36] and it disrupts the development of a diffusion boundary layer (DBL), which can both lead to improved mass transfer.[37] On the other hand, the porous structure can be a disadvantage for gas-evolving reactions, as bubbles can get trapped in the pores and form gas pockets in which the active surface area is blocked and the ionic conductivity is significantly diminished.

As an alternative to flow-through electrodes, suspension electrodes possess an even larger electrochemical surface area in relation to their volume, as they typically consist of suspended microparticles with a surface area of 200-2000 m²/g, which also lends the suspension considerable capacitance.[38] This has led to successful application of sus-

pension electrodes in multiple capacitance-based applications such as Electrochemical Flow Capacitors (EFCs)[39], Flow Electrode Capacitive Deionization (FCDI)[5, 40], Redox Flow Batteries (RFBs)[41] and Microbial Fuel Cells (MFCs)[6, 42]. Although the dynamic nature of the conductive networks in suspension electrodes offers less electric conductivity than the static network in foam electrodes, it greatly improves bubble removal and offers an advantage for use in gas-evolving systems.

The combination of ionic- and electric conductivity, improved electrode-electrolyte contact, large surface area, and the opportunity for electrolyte flow lends both systems great potential for use as volume-based electrodes for mass transfer-limited reactions such as CO_2 and O_2 reduction.

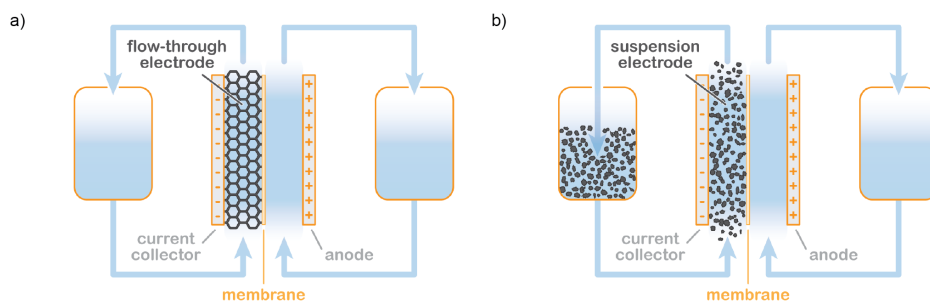


Figure 1.3: Schematic illustration of electrochemical flow cells with a) a flow-through electrode, and b) a suspension electrode incorporated.

1.5. THESIS OUTLINE AND RESEARCH QUESTIONS

The aim of this thesis is to explore to what extent volume-based electrodes, either as flow-through or as flow-with electrodes, can alleviate mass transfer limitations and boost limiting currents in electrochemical conversion reactions. The novelty of this work is twofold as it 1) addresses the issue of mass transfer limitations in electrochemical conversion systems through a new strategy, and 2) applies suspension electrodes in a new field of research. We explore the opportunities of volume-based electrodes and investigate the requirements to realize their full potential, as well as their influence on the mass transfer limitation, and the limits to their applicability through the following research questions:

1. What are the most relevant criteria to achieve a homogeneous reaction distribution in a flow-with electrode? (Ch. 2)
2. Can replacing the carbon suspension by an inert static conductive network boost the FE and CO_2 reduction current density? (Ch. 3)
3. How do surfactants affect the stability and performance of catalytically active suspensions? (Ch. 3)
4. How does the porous structure of the flow-through electrode influence mass transfer and the limiting current during the ORR? (Ch. 4)

5. What is the impact of improved mass transfer on scaled-up aqueous systems with low reagent concentrations? (Ch. 4)
6. How do the applied current density and electrolyte flow velocity influence the DBL thickness and local concentration profiles? (Ch. 5)

Chapter 2 explores the influence of suspension electrode properties (electric, morphological, and rheological) on the expected performance for CO₂ reduction (RQ1). We investigate the key requirements for the reaction to be properly distributed over the bulk of the suspension and make optimal use of the potential advantages of suspension electrodes. Additionally, we combine electrochemical impedance spectroscopy (EIS) results with rheology measurements to examine the relation between rheological and electrical properties of suspensions with different particle morphology. Finally, we tested several suspension electrodes in a CO₂ electrolyzer. Although the chapter is oriented towards suspension electrodes for CO₂ reduction, our findings are applicable to flow-through electrodes and other conversion reactions as well.

As Chapter 2 is inconclusive about the full potential of suspension electrodes, Chapter 3 investigates the importance of stabilizing agents and the benefit of replacing the carbon suspension by a flow-through electrode that provides a permanent conductive network spanning across the entire channel depth. The catalytic material is kept in suspension, stabilized by surfactants, and flowed through the 3D current collector.

In Chapter 4, we examine the effect of the electrode configurations on mass transfer in more detail. We perform the ORR in flow cells with all three electrode configurations: the conventional flow-by (planar) configuration, and the volume-based flow-through (foam) and flow-with (suspension) electrodes. We compare the electrochemical performance (limiting current density and FE), investigate the influence of flow configuration on mass transfer through Sherwood correlations, and investigate the limitations of the enhanced aqueous system during scale up.

Chapter 5 studies mass transfer around a single carbon particle representing an element of a 3D electrode. We visualize the diffusion boundary layer with Fluorescence Lifetime Imaging (FLIM) and study the effect of applied current density and electrolyte flow velocity on the pH profile around the particle electrode. Our results offer insights into the local reaction environment around an element of a 3D electrode, including reagent depletion, product buildup, and local pH, and into important design parameters for 3D electrodes such as flow-through and suspension electrodes. Additionally, we look into the ability of the electric double layer (EDL) capacitance to maintain an ongoing Faradaic reaction.

REFERENCES

- [1] Huidong Shen, Changhyeok Choi, Justus Masa, Xin Li, Jieshan Qiu, Yousung Jung, and Zhenyu Sun. “Electrochemical ammonia synthesis: Mechanistic understanding and catalyst design”. In: *Chem* 7.7 (2021), pp. 1708–1754.
- [2] Tingting Wu, Wenjun Fan, Yang Zhang, and Fuxiang Zhang. “Electrochemical synthesis of ammonia: Progress and challenges”. In: *Materials Today Physics* 16 (2021), p. 100310.
- [3] Nicholas J. Matteucci, Christopher T. Mallia, Bertrand J. Neyhouse, Madhu V. Majji, and Fikile R. Brushett. “Toward electrochemical design principles of redox-mediated flow batteries”. In: *Current Opinion in Electrochemistry* 42 (2023), p. 101380.
- [4] Volker Presser, Christopher R. Dennison, Jonathan Campos, Kevin W. Knehr, Emin C. Kumbur, and Yury Gogotsi. “The Electrochemical Flow Capacitor: A New Concept for Rapid Energy Storage and Recovery”. In: *Advanced Energy Materials* 2.7 (2012), pp. 895–902.
- [5] Jie Ma, Chunxiao Zhai, and Fei Yu. “Review of flow electrode capacitive deionization technology: Research progress and future challenges”. In: *Desalination* 564 (2023), p. 116701.
- [6] Alexandra Deeke, Tom H. J. A. Sleutels, Tim F. W. Donkers, Hubertus V. M. Hamelers, Cees J. N. Buisman, and Annemiek Ter Heijne. “Fluidized Capacitive Bioanode As a Novel Reactor Concept for the Microbial Fuel Cell”. In: *Environmental Science & Technology* 49.3 (2015), pp. 1929–1935.
- [7] Naef A. A. Qasem. “A recent overview of proton exchange membrane fuel cells: Fundamentals, applications, and advances”. In: *Applied Thermal Engineering* 252 (2024), p. 123746.
- [8] Sukhvinder P. S. Badwal, Sarbjit S. Giddey, Christopher Munnings, Anand I. Bhatt, and Anthony F. Hollenkamp. “Emerging electrochemical energy conversion and storage technologies”. In: *Frontiers in Chemistry* 2 (2014).
- [9] David W. Keith, Geoffrey Holmes, David St. Angelo, and Kenton Heidel. “A Process for Capturing CO₂ from the Atmosphere”. In: *Joule* 2.8 (2018), pp. 1573–1594.
- [10] R. Sharifian, R. M. Wagterveld, I. A. Digdaya, C. Xiang, and D. A. Vermaas. “Electrochemical carbon dioxide capture to close the carbon cycle”. In: *Energy & Environmental Science* 14.2 (2021), pp. 781–814.
- [11] Shuyu Liang, Naveed Altaf, Liang Huang, Yanshan Gao, and Qiang Wang. “Electrolytic cell design for electrochemical CO₂ reduction”. In: *Journal of CO₂ Utilization* 35 (2020), pp. 90–105.
- [12] Ryoji Noyori, Masao Aoki, and Kazuhiko Sato. “Green oxidation with aqueous hydrogen peroxide”. In: *Chemical Communications* 16 (2003), pp. 1977–1986.
- [13] Sara Ann Fast, Veera Gnanaswar Gude, Dennis D. Truax, James Martin, and Benjamin S. Magbanua. “A Critical Evaluation of Advanced Oxidation Processes for Emerging Contaminants Removal”. In: *Environmental Processes* 4.1 (2017), pp. 283–302.

- [14] Xiao Zhang, Yang Xia, Chuan Xia, and Haotian Wang. “Insights into Practical-Scale Electrochemical H_2O_2 Synthesis”. In: *Trends in Chemistry* 2.10 (2020), pp. 942–953.
- [15] Rosaria Ciriminna, Lorenzo Albanese, Francesco Meneguzzo, and Mario Pagliaro. “Hydrogen Peroxide: A Key Chemical for Today’s Sustainable Development”. In: *ChemSusChem* 9.24 (2016), pp. 3374–3381.
- [16] Jose M. Campos-Martin, Gema Blanco-Brieva, and Jose L. G. Fierro. “Hydrogen Peroxide Synthesis: An Outlook beyond the Anthraquinone Process”. In: *Angewandte Chemie International Edition* 45.42 (2006), pp. 6962–6984.
- [17] Danielle Salvatore and Curtis P. Berlinguette. “Voltage Matters When Reducing CO_2 in an Electrochemical Flow Cell”. In: *ACS Energy Letters* 5.1 (2020), pp. 215–220.
- [18] Md Golam Kibria, Jonathan P. Edwards, Christine M. Gabardo, Cao-Thang Dinh, Ali Seifitokaldani, David Sinton, and Edward H. Sargent. “Electrochemical CO_2 Reduction into Chemical Feedstocks: From Mechanistic Electrocatalysis Models to System Design”. In: *Advanced Materials* 31.31 (2019), p. 1807166.
- [19] Richard I. Masel, Zengcai Liu, Hongzhou Yang, Jerry J. Kaczur, Daniel Carrillo, Shaoxuan Ren, Danielle Salvatore, and Curtis P. Berlinguette. “An industrial perspective on catalysts for low-temperature CO_2 electrolysis”. In: *Nature Nanotechnology* 16.2 (2021), pp. 118–128.
- [20] Sumit Verma, Byoungsu Kim, Huei-Ru “Molly” Jhong, Sichao Ma, and Paul J. A. Kenis. “A Gross-Margin Model for Defining Technoeconomic Benchmarks in the Electroreduction of CO_2 ”. In: *ChemSusChem* 9.15 (2016), pp. 1972–1979.
- [21] Lorenz M. Baumgartner, Aron Kahn, Maxime Hoogland, Jorrit Bleeker, Wolter F. Jager, and David A. Vermaas. “Direct imaging of local pH reveals bubble-induced mixing in a CO_2 electrolyzer”. In: *ACS Sustainable Chemistry & Engineering* 11.28 (2023), pp. 10430–10440.
- [22] Drew Higgins, Christopher Hahn, Chengxiang Xiang, Thomas F. Jaramillo, and Adam Z. Weber. “Gas-Diffusion Electrodes for Carbon Dioxide Reduction: A New Paradigm”. In: *ACS Energy Letters* 4.1 (2019), pp. 317–324.
- [23] Byoungsu Kim, Febrian Hillman, Miho Ariyoshi, Shigenori Fujikawa, and Paul J. A. Kenis. “Effects of composition of the micro porous layer and the substrate on performance in the electrochemical reduction of CO_2 to CO ”. In: *Journal of Power Sources* 312 (2016), pp. 192–198.
- [24] Lorenz M. Baumgartner, Christel I. Koopman, Antoni Forner-Cuenca, and David A. Vermaas. “Narrow pressure stability window of gas diffusion electrodes limits the scale-up of CO_2 electrolyzers”. In: *ACS Sustainable Chemistry & Engineering* 10.14 (2022), pp. 4683–4693.
- [25] Bert De Mot, Jonas Hereijgers, Miguel Duarte, and Tom Breugelmanns. “Influence of flow and pressure distribution inside a gas diffusion electrode on the performance of a flow-by CO_2 electrolyzer”. In: *Chemical Engineering Journal* 378 (2019), p. 122224.

- [26] Kailun Yang, Recep Kas, Wilson A. Smith, and Thomas Burdyny. "Role of the Carbon-Based Gas Diffusion Layer on Flooding in a Gas Diffusion Electrode Cell for Electrochemical CO₂ Reduction". In: *ACS Energy Letters* 6.1 (2021), pp. 33–40.
- [27] Eric W. Lees, Benjamin A. W. Mowbray, Fraser G. L. Parlane, and Curtis P. Berlinguette. "Gas diffusion electrodes and membranes for CO₂ reduction electrolyzers". In: *Nature Reviews Materials* 7.1 (2022), pp. 55–64.
- [28] Bert De Mot, Mahinder Ramdin, Jonas Hereijgers, Thijs J. H. Vlucht, and Tom Breugelmanns. "Direct Water Injection in Catholyte-Free Zero-Gap Carbon Dioxide Electrolyzers". In: *ChemElectroChem* 7.18 (2020), pp. 3839–3843.
- [29] Kostadin V. Petrov, Justin C. Bui, Lorenz Baumgartner, Lien-Chun Weng, Sarah M. Dischinger, David M. Larson, Daniel J. Miller, Adam Z. Weber, and David A. Vermaas. "Anion-exchange membranes with internal microchannels for water control in CO₂ electrolysis". In: *Sustainable Energy & Fuels* 6.22 (2022), pp. 5077–5088.
- [30] Barun Kumar Chakrabarti, Evangelos Kalamaras, Abhishek Kumar Singh, Antonio Bertei, J. Rubio-Garcia, Vladimir Yufit, Kevin M. Tenny, Billy Wu, Farid Tariq, Yashar S. Hajimolana, Nigel P. Brandon, Chee Tong John Low, Edward P. L. Roberts, Yet-Ming Chiang, and Fikile R. Brushett. "Modelling of redox flow battery electrode processes at a range of length scales: a review". In: *Sustainable Energy & Fuels* 4.11 (2020), pp. 5433–5468.
- [31] M. Maruthi Prasanna and Sreenivas Jayanti. "Effect of electrolyte circulation rate in flow-through mode on the performance of vanadium redox flow battery". In: *Journal of Power Sources* 582 (2023), p. 233536.
- [32] Zheng-Yang Huo, Xiaoxiong Wang, Xia Huang, and Menachem Elimelech. "Intensifying electrified flow-through water treatment technologies via local environment modification". In: *Frontiers of Environmental Science & Engineering* 18.6 (2024), p. 69.
- [33] Feichen Yang, Myung Jun Kim, Micah Brown, and Benjamin J. Wiley. "Alkaline Water Electrolysis at 25 A cm⁻² with a Microfibrous Flow-through Electrode". In: *Advanced Energy Materials* 10.25 (2020), p. 2001174.
- [34] José Fernando Pérez, Javier Llanos, Cristina Sáez, Conrado López, Pablo Cañizares, and Manuel Andrés Rodrigo. "Towards the scale up of a pressurized-jet microfluidic flow-through reactor for cost-effective electro-generation of H₂O₂". In: *Journal of Cleaner Production* 211 (2019), pp. 1259–1267.
- [35] Chao Zhang, Yonghai Jiang, Yunlin Li, Zhongxin Hu, Lei Zhou, and Minghua Zhou. "Three-dimensional electrochemical process for wastewater treatment: A general review". In: *Chemical Engineering Journal* 228 (2013), pp. 455–467.
- [36] J. W. Haverkort. "A theoretical analysis of the optimal electrode thickness and porosity". In: *Electrochimica Acta* 295 (2019), pp. 846–860.
- [37] D. J. Gunn. "Transfer of heat or mass to particles in fixed and fluidised beds". In: *International Journal of Heat and Mass Transfer* 21.4 (1978), pp. 467–476.

- [38] Monjur Mourshed, Seyed Mohammad Rezaei Niya, Ruchika Ojha, Gary Rosen-garten, John Andrews, and Bahman Shabani. “Carbon-based slurry electrodes for energy storage and power supply systems”. In: *Energy Storage Materials* 40 (2021), pp. 461–489.
- [39] Meng Tian, Yueqing Sun, Chuanfang Zhang, Jitong Wang, Wenming Qiao, Licheng Ling, and Donghui Long. “Enabling high-rate electrochemical flow capacitors based on mesoporous carbon microspheres suspension electrodes”. In: *Journal of Power Sources* 364 (2017), pp. 182–190.
- [40] Wann Zhang, Wenchao Xue, Kang Xiao, Chettiyappan Visvanathan, Jialing Tang, and Lu Li. “Selection and optimization of carbon-based electrode materials for flow-electrode capacitive deionization”. In: *Separation and Purification Technol-ogy* 315 (2023), p. 123649.
- [41] Hongning Chen, Yao Liu, Xuefeng Zhang, Quan Lan, Yue Chu, Yongliang Li, and Qixing Wu. “Single-component slurry based lithium-ion flow battery with 3D cur-rent collectors”. In: *Journal of Power Sources* 485 (2021), p. 229319.
- [42] C. Borsje, T. Sleutels, W. Zhang, W. Feng, C. J. N. Buisman, and A. ter Heijne. “Mak-ing the best use of capacitive current: Comparison between fixed and moving gran-ular bioanodes”. In: *Journal of Power Sources* 489 (2021), p. 229453.

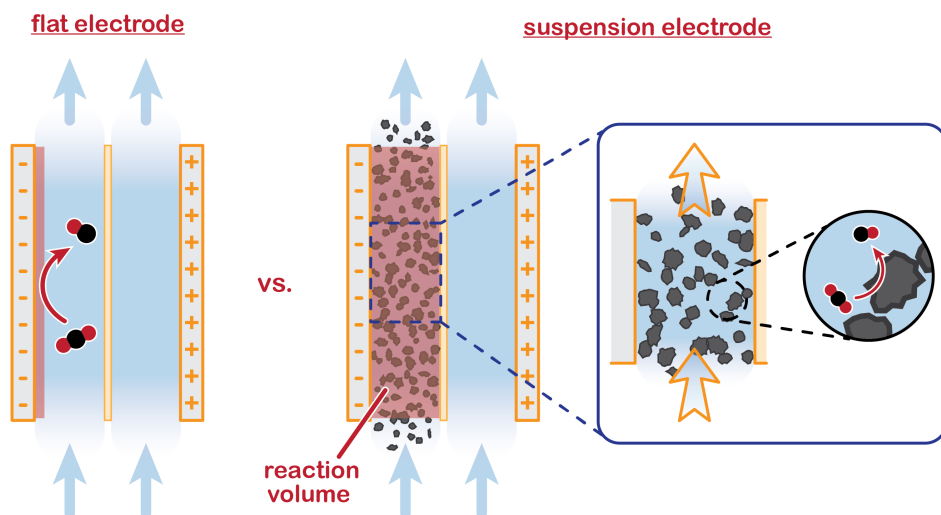
2

PRACTICAL POTENTIAL OF SUSPENSION ELECTRODES FOR ENHANCED LIMITING CURRENTS IN ELECTROCHEMICAL CO₂ REDUCTION

Parts of this chapter have been published as "*Practical potential of suspension electrodes for enhanced limiting currents in electrochemical CO₂ reduction*" by Nathalie E. G. Ligthart, Gerard Prats Vergel, Johan T. Padding, and David A. Vermaas in *Energy Advances*, 2024, 3, 841-853.

ABSTRACT

CO₂ conversion is an important part of the transition towards clean fuels and chemicals. However, low solubility of CO₂ in water and its slow diffusion cause mass transfer limitations in aqueous electrochemical CO₂ reduction. This significantly limits the partial current densities towards any desired CO₂-reduction product. We propose using flowable suspension electrodes to spread the current over a larger volume and alleviate mass transfer limitations, which could allow high partial current densities for CO₂ conversion even in aqueous environments. To identify the requirements for a well-performing suspension electrode, we use a transmission line model to simulate the local electric and ionic current distributions throughout a channel and show that the electrocatalysis is best distributed over the catholyte volume when the electric, ionic and charge transfer resistances are balanced. In addition, we used electrochemical impedance spectroscopy to measure the different resistance contributions and correlated the results with rheology measurements to show that particle size and shape impact the ever-present trade-off between conductivity and flowability. We combine the modelling and experimental results to evaluate which carbon type is most suitable for use in a suspension electrode for CO₂ reduction, and predict a good reaction distribution throughout activated carbon and carbon black suspensions. Finally, we tested several suspension electrodes in a CO₂ electrolyzer. Even though mass transport limitations should be reduced, the CO partial current densities are capped at 2.8 mA/cm², which may be due to engineering limitations. We conclude that using suspension electrodes is challenging for sensitive reactions like CO₂ reduction, and may be more suitable for use in other electrochemical conversion reactions suffering from mass transfer limitations that are less affected by competing reactions and contaminations.



2.1. INTRODUCTION

The high level of carbon dioxide (CO₂) in our atmosphere is causing notable climate change all over the world, and levels are still rising. We need to significantly lower fossil fuel emissions by transitioning towards clean energy, in order to mitigate climate change.[1] The most familiar and popular choice of renewable energy is green electricity, but this cannot power all processes. For some applications this is due to intermittency of wind and sunlight, while other sectors cannot run on electricity and are likely to remain dependent on hydrocarbons (*e.g.* cargo ships, planes, plastics and pharmaceuticals).[2]

We can introduce CO₂ circularity by using renewable, synthetically produced hydrocarbons to replace fossil fuels.[2–4] Modern technologies can extract CO₂ from the air[5] or ocean[6], after which the CO₂ can be converted into fuels or chemicals. Electrochemical CO₂ reduction is widely studied as a conversion method because it requires only CO₂, water and electricity as input. Nevertheless, CO₂ electrolysis is only commercially viable when operating at high current densities of at least 200 mA/cm². [2, 7]

The current density at which CO₂ can be converted is limited by the availability of CO₂ at the catalyst surface.[8–10] Because CO₂ has a low solubility in water (34 mM, at ambient temperature and pressure[11]), even low current densities cause CO₂ depletion at the electrode surface in aqueous reactors[11, 12], while the remaining current drives the Hydrogen Evolution Reaction (HER).[3, 8, 9, 13] This limits the maximum CO partial current density to about 2 mA/cm² in aqueous systems that rely on forced convection and diffusion.[14] Bubble-induced mixing[15] and leveraging buffering reactions with bicarbonate[16, 17] can raise this up to tens of mA/cm², which is still well below the required 200 mA/cm². Therefore, our challenge is to accelerate CO₂ mass transport towards the electrode.

Several strategies to enhance mass transport have been investigated, each with their own advantages and challenges. The most widely applied strategy is to supply CO₂ in gas phase instead of dissolved in an electrolyte. Examples of such electrolyzers are flow cells with a Gas Diffusion Electrode (GDE)[18, 19], Membrane Electrode Assemblies (MEAs)[20–22] and Solid Oxide Electrolysis Cells (SOECs)[23–25]. Using a gaseous CO₂ supply significantly raises the CO₂ flux towards the electrode surface and boosts the limiting current density. Although this concept is promising, vapour-fed electrolyzers are delicate and complicated systems. Challenges in scaling up include water management at the porous electrode[26, 27] and drying out of ionic separators[28, 29]. Additionally, stability issues occur due to differential pressure and electrowetting[26, 27, 30], salt formation[9] and degradation of carbon in the porous electrode[30]. These complications in GDE-based CO₂ electrolyzers raise the question whether there are still unexplored strategies to circumvent the mass transfer limitations in aqueous CO₂ reduction.

We propose to use suspension electrodes to alleviate mass transfer limitations in CO₂ electrolyzers and boost the achievable CO₂ reduction current density. In suspension electrodes, electric charges are transported into the bulk of the electrolyte by conductive networks of microparticles, or their capacitive functionality.[31] Using a suspension electrode brings several potential advantages over using a conventional configuration, including 1) the use of dissolved CO₂ in the full volume instead of a thin layer at the cathode, 2) a lower local current density inside the suspension because of the large surface area, and 3) flowing microparticles may induce additional mixing of the electrolyte.

While suspension electrodes have been studied for various applications, including flow capacitors[32, 33], flow batteries[34–36], deionization technology[37, 38] and microbial fuel cells[39, 40], they have not been applied in electrochemical CO₂ reduction. The conductivity and capacitance can be tuned through material choice, particle loading, or addition of conductive additives. High surface area carbon materials have high capacitance, but are usually less conductive than graphitic carbons with lower surface area.[41] The effects of suspension material and loading, and the associated conductive networks, capacitance and viscosity are yet unknown in CO₂ electrolyzers.

In this work, we identify the requirements for a well-performing suspension electrode for electrochemical CO₂ reduction. We do this by measuring important suspension properties, including electric conductivity and viscosity. We use the results to model local current densities inside the electrolyzer channel and find the key parameters that determine when a suspension is used to its full advantage. Finally, we test several suspension electrodes in a CO₂ electrolyzer. Our findings can help in adapting the composition of suspension electrodes for use in mass transfer limited electrochemical processes.

2.2. CONCEPT

We propose to combine a CO₂ reduction flow cell with an electrocatalytic suspension electrode. In such a configuration, the flow cell consists of two flow channels through which electrolyte is pumped continuously. The compartments are separated by an ion exchange membrane. Our concept makes use of a relatively inert current collector (such as glassy carbon or graphite), while the CO₂ reduction reaction takes place at the surface of suspended microparticles. A schematic representation of such a system is shown in Figure 2.1.

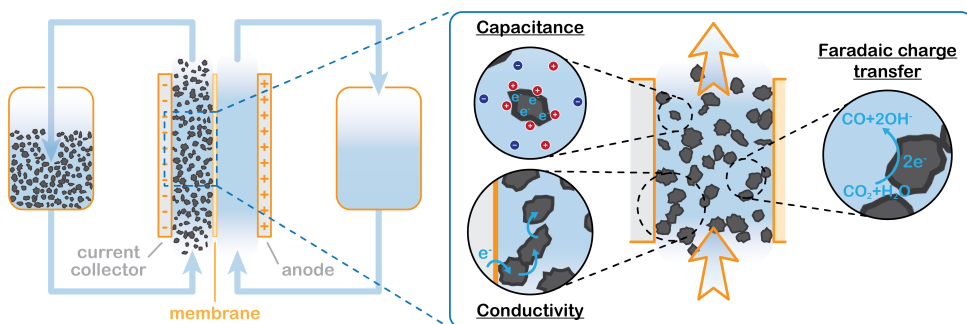


Figure 2.1: Suspension based electrochemical flow system (left) and charge transfer mechanisms inside the flowing suspension electrode (right). Charge transfer takes place through electric double layer charging (capacitive charge storage), electric conductivity via particle networks, and Faradaic charge transfer, in this example CO₂ reduction to CO.

The suspension electrode should consist of electrically conductive and capacitive microparticles (typically between 5 and 20 wt% [42]) that are suspended in an electrolyte. A current is applied to the suspension via a current collector and conducted into the bulk via particle networks.[31] Electric Double Layer (EDL) formation facilitates charge storage inside a particle when it temporarily detaches from a network.[31] This capacitive

effect enables the particle to transfer the charge further into the suspension or continue the reaction. A schematic of the charge transfer mechanisms is shown in Figure 2.1.

Suspension electrodes can be designed for many applications because their properties and functionality rely on their composition.[41] For example, highly porous carbon particles are well-suited for use in applications that rely on high capacitance, such as Electrochemical Flow Capacitors (EFCs) and Flow Electrode Capacitive Deionization (FCDI), while redox active materials can be added to make a Redox Flow Battery (RFB).[35, 38] Suspension electrodes have been shown to work well in Microbial Fuel Cells (MFCs) as well. MFCs benefit significantly from the large surface area provided by the microparticles.[39, 40] The increased surface area allows for lower local current densities and higher capacitance. The EDL acts as electron supply for the microbes while they are not in contact with the current collector, and thus allows for longer reaction time. We expect to see the same advantage in mass transfer limited reactions, like aqueous CO₂ reduction.

Having high electric and ionic conductivity, and low viscosity are important for minimizing Ohmic and pumping losses.[41] Although raising the particle loading significantly enhances both electrical conductivity and capacitance, it also considerably increases viscosity and thus decreases the flowability of the system.[43, 44] Alternatively, conductive additives can be added in low amounts (up to 5 wt%) to boost conductivity. Depending on material, size and shape, some microparticles and additives have a lower impact on viscosity.[45] However, achieving both good electrical and good rheological properties in one suspension remains challenging.

As mentioned in the introduction, we expect higher limiting current densities in suspension electrodes because of three principles. First, using a suspension electrode allows for the current to percolate through the whole flow channel, making CO₂ in the whole channel volume available for reduction. We can estimate how much additional CO₂ is made available for reaction in our suspension cell compared to a plate electrode. For our channel thickness of 3 mm, and CO₂ concentration of 34 mM, the compartment contains 10 μmol of CO₂ per (geometric) cm². Assuming that the electric current in a suspension can reach the full compartment thickness and that the interparticle distance is smaller than the boundary layer thickness (typically 100 μm), the complete 10 μmol of CO₂ per cm² is available for reaction. In contrast, a plate electrode has charge transfer only at the boundary of the channel and CO₂ molecules need to travel towards it before they can be converted. In this case, we need to consider the slow transport across the diffusion boundary layer. We estimate the amount of CO₂ transported to the electrode per second (\dot{n}) from $k = D/\delta = (\dot{n}/\Delta c A)$, with a mass transfer coefficient (k) in the order of 10⁻⁵ m/s for a diffusion coefficient (D) of 10⁻⁹ m²/s and a diffusion layer thickness (δ) of 100 μm[46, 47], and a concentration difference between the surface and bulk (Δc) of 34 mM, on an area (A) of 1 cm². This results in only 0.2 μmol/cm² being able to reach the flat electrode during a residence time of 5 s. This is 50 times less than the 10 μmol of CO₂ that can be reached by the suspension electrode. Hence, suspension electrodes could increase the limiting current density by a factor 50. In addition to having more CO₂ available due to the larger reaction volume, the applied current density is spread over a significantly larger surface area and the local current density can be lowered by an order of magnitude compared to the geometrical current density. This lowers the required

charge transfer overpotential and promotes selectivity towards the desired reaction.[48] Finally, solid phase particles have been shown to induce mixing in the liquid phase in two-phase flows.[49] This can further accelerate CO_2 mass transfer towards the catalytic surface.

2

2.3. METHODS

2.3.1. MODELLING

We model the solid and liquid phase currents throughout the channel to evaluate where the reaction is taking place in suspensions of different particle types and loadings, and electrolyte concentrations. We consider the suspension as a porous electrode and use the Transmission Line Model (TLM) by Alfisi et al. with the corresponding equivalent circuit shown in 2.2b.[50] The model considers two charge transfer pathways, through the solid and liquid phases with resistances (per unit length, Ω/cm) R'_S and R'_L , respectively as shown in 2.2a. We use the solid resistance extracted from Electrochemical Impedance Spectroscopy (EIS) measurements in the next section (2.3.2 Experiments) to account for the temporality and changeability of the porous network in the suspension. The interfacial impedance between solid and liquid phase consists of a volumetric charge transfer resistance R''_{ct} ($\Omega\text{-cm}^3$), which results in the Faradaic current, and a volumetric double layer capacitance C'_{dl} (F/cm^3) in parallel.[50]

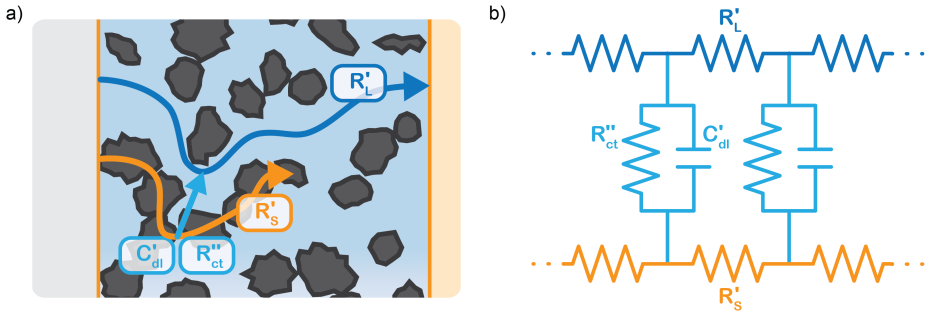


Figure 2.2: Schematics of the charge transfer pathways through the liquid, solid and interface of a suspension electrode, and b) the corresponding equivalent circuit used in the TLM model. The ionic and electric conductances are described using their resistances R'_S and R'_L , respectively, while the interfacial charge transfer consists of a capacitive EDL (C'_{dl}) and Faradaic charge transfer (R''_{ct}).

The following governing equations 2.1 and 2.2 are found by defining the potential drops over infinitesimal elements in the liquid and solid phase, respectively, and linking them through the interfacial impedance[50]:

$$\frac{d^2\phi_S}{dx^2} = -A_C \frac{R'_S}{Z''_S} (\phi_L - \phi_S), \quad (2.1)$$

$$\frac{d^2\phi_L}{dx^2} = -A_C \frac{R'_L}{Z''_S} (\phi_L - \phi_S) \quad (2.2)$$

in which

$$Z_S'' = \left(\frac{1}{R_{ct}''} + C_{dl}' \omega j \right)^{-1} \quad (2.3)$$

Here A_C is the cross-sectional area of the channel (cm^2) and the x direction is taken to be across the flow channel, ranging from $x = 0$ at the current collector to $x = l_e$ at the membrane. We set the potential at $x = 0$ to be the applied potential (V_{app}), and assume a completely ionic current at the membrane, resulting in boundary conditions[50]

$$\phi_S(0, t) = V_{app}, \quad \left. \frac{\partial \phi_S}{\partial x} \right|_{x=l_e} = 0. \quad (2.4)$$

Additionally, we set the liquid potential at the membrane to 0, and assume a completely electric current at the electrode interface, yielding[50]

$$\phi_L(l_e, t) = 0, \quad \left. \frac{\partial \phi_L}{\partial x} \right|_{x=0} = 0. \quad (2.5)$$

With these boundary conditions, we solved the governing equations 2.1 and 2.2 numerically for low frequency ω to approximate DC voltages.

2.3.2. EXPERIMENTS

The slurries were prepared by adding carbon material to 0.5 M KHCO_3 ($\leq 99\%$, ThermoFisher Scientific) as a typical electrolyte for CO_2 reduction[8, 51], under stirring. The suspensions were sonicated (ultrasonic cleaner USC 500 TH, 45 kHz, VWR) for 30 minutes. The slurries consisted of 0-20 wt% Activated Carbon (AC, 20 μm median particle size, 1000 m^2/g , Norit SX Plus CAT, Sigma Aldrich), Carbon Black (CB, average particle size of 50 nm, 250 m^2/g , Vulcan XC-72, Fuel Cell Store), or 0-40 wt% glassy carbon spheres (gC, 10-20 μm glassy carbon spherical powder, Alfa Aesar). In the suspensions used for electrolysis, 25 wt% of the solid content was replaced by Ag nanopowder (20-40 nm, 99.9%, Alfa Aesar) to function as catalyst.

Rheology measurements were performed on carbon suspensions without Ag nanopowder using a stress controlled Dynamic Hybrid Rheometer (TA Instruments, DHR-3). The rheometer was equipped with a Couette geometry consisting of a stainless steel cup (diameter of 30 mm) with Peltier heating element and stainless steel DIN rotor (28 mm diameter, 42.07 mm length). All measurements were performed while maintaining a gap of 5917.1 μm between the rotor and the bottom of the cup, and a temperature of 25 $^\circ\text{C}$. The shear rates of interest ranged between 2 and 1000 s^{-1} and were applied for 3-4 minutes. The suspension was pre-sheared at 2000 s^{-1} before each measurement to erase memory and sedimentation effects.[52]

The suspension impedance was measured under flow conditions in a custom-made flow cell (Figure S9), incorporating only one flow channel (3 mm thick PMMA) and no ion-exchange membrane. The slurries were pumped (peristaltic L/S Precision Pump System, Masterflex) upwards through the channel between two graphite (99.95% rigid graphite, Goodfellow) current collectors with four electrical connections. EIS was performed with an Autolab potentiostat (PGSTAT302N, Metrohm). A sinusoidal perturbation with a frequency range from 0.1 to 10^5 Hz was applied with an amplitude of 5 mV around the Open Circuit Voltage (OCV).

EIS provides insight into properties, such as conductivity and capacitance, of different processes in electrochemical systems. These can be extracted by fitting the EIS data to an equivalent circuit of the system. Because we run the EIS in a potential window with only non-Faradaic reactions, the equivalent circuit deviates from that in 2.2b. A schematic of important processes in suspension electrodes is shown in 2.3a, and can be used to deduce a sensible equivalent circuit. The current applied to the current collector can take various paths, namely it can charge the EDL, with a capacitance $C_{dl,CC}$, and proceed as ionic current through the electrolyte with a resistance R_L . Alternatively, the current can be electrically conducted into the suspension via a contact resistance between the current collector and a particle (R_{CC-p}), after which the current travels through the suspension via particle networks and collisions. These consist of the carbon material resistance (R_p) and contact resistance between particles (R_{p-p}). Instead of transferring to another particle, electrons can be stored in the EDL at a particle surface, which can be described as an imperfect capacitance ($C_{dl,p}$) in a constant phase element (CPE). We combined the electrical elements corresponding to these processes into the equivalent circuit shown in 2.3b and used this to fit the EIS data.

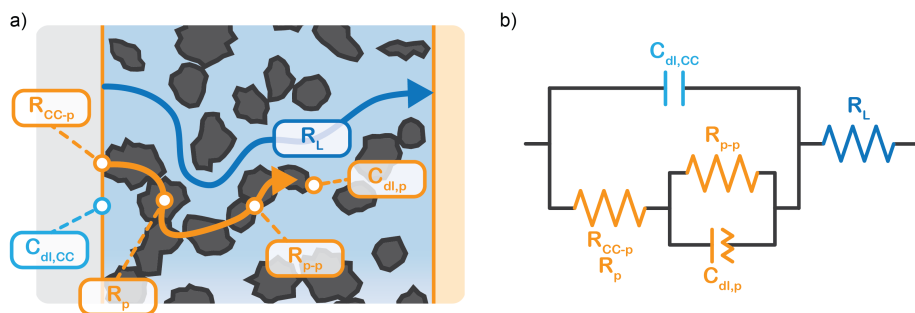


Figure 2.3: Schematics of the a) non-Faradaic charge transfer pathways in a suspension electrode taking place near the Open Circuit Voltage (OCV) and b) the equivalent circuit containing the corresponding electrical elements that was used for fitting the EIS data. The current is transferred between the current collector to particles via a resistance R_{CC-p} . The particles have a material resistance R_p , an interparticle resistance R_{p-p} , and an imperfect capacitance $C_{dl,p}$ that can be fitted with a Constant Phase Element (CPE). The current collector capacitance and electrolyte resistance are fitted as $C_{dl,CC}$ and R_L , respectively.

Electrolysis was performed via chronopotentiometry in the same suspension flow cell equipped with two flow channels (as shown in Figure S2.9) separated by a Selemion anion exchange membrane (100 μm , AGC Engineering) that was pre-soaked in electrolyte. A graphite current collector, an Ir-/Ru-oxide coated Ti-sheet (Permascand) anode, and a leak-free Ag/AgCl reference electrode (LF-1-45, Alvatek) were used for electrolysis. Both the catholyte (suspension) and anolyte (0.5 M KHCO_3) were saturated by sparging 50 mL/min CO_2 for at least 30 minutes before, and continuously purged and recirculated (peristaltic L/S Precision Pump System, Masterflex) during each experiment. A constant current density was applied with an IviumStat.h ($\pm 5\text{A}/\pm 10\text{V}$, Ivium) for 45 minutes, during which samples of the product gases were taken every 3-4 minutes from the headspace of the catholyte reservoir and analyzed with an inline gas chromatograph (CompactGC^{4.0}, Interscience).

2.4. RESULTS AND DISCUSSION

2.4.1. RATIO OF REACTION AND CONDUCTION RESISTANCES IS KEY IN ELECTRODE UTILIZATION

We modelled the local current densities for different ratios of R''_{ct} with R'_S and R'_L to evaluate the influence on electrode utilization and reaction distribution. The current densities in the solid and liquid phases are calculated with equations 2.6 and 2.7 respectively.[50, 53]

$$j_S = -\frac{1}{A_C R'_S} \frac{\partial \phi_S}{\partial x} \quad (2.6)$$

$$j_L = \frac{1}{A_C R'_L} \frac{\partial \phi_L}{\partial x} \quad (2.7)$$

Figures 2.4a-c show the relative contributions to the current that are conducted through the solid (j_S/j_{total}) and liquid (j_L/j_{total}) phase, at different ratios of R''_{ct} with R'_S and R'_L . A factor of $1/(Vl_e)$ is included to match the units and to allow for comparison of the values, where V and l_e are the electrode volume and thickness, respectively. The derivation of this factor is included in the SI. This factor depends on the geometry of the cell, and is close to unity for our case ($V = 2.5 \text{ cm}^3$, $l_e = 0.3 \text{ cm}$). Figures 2.4d-f indicate the local charge transfer from the solid to the liquid phase over the thickness of the channel.

When the normalized charge transfer resistance (R''_{ct}) is much higher than the resistance of the solid and liquid phases (Figures 4a and 4d), the reaction distributes evenly over the full channel. Consequently, the current through the solid phase decreases linearly with increasing distance from the current collector, while the current through the liquid accumulates linearly (Figure 4a). Hence, the Faradaic current is constant throughout the channel (Figure 4d). Such a case resembles a suspension electrode with the reaction occurring over the full channel thickness.

The situation changes slightly when $1/(Vl_e)R''_{ct}$ is in the same order of magnitude as the solid (R'_S) and liquid (R'_L) phase resistances, as shown in Figures 2.4b and 2.4e. In this case, the Faradaic current can still be relatively equally distributed, but the ratio between R'_S and R'_L gains importance and determines at which side of the channel the reaction is favoured. The system minimizes the total resistance, causing the current to be carried longer in the phase with the lowest resistance. For example, when the solid resistance is low, the current tends to transfer from the solid to the liquid phase later in the channel, pushing the main reaction location towards the membrane ($x = 3 \text{ mm}$). Oppositely, the Faradaic charge transfer occurs dominantly near the current collector ($x = 0 \text{ mm}$) in case of a higher solid phase resistance.

This effect is especially visible when $1/(Vl_e)R''_{ct}$ is significantly lower than either phase resistance (Figures 4c and f), in which case the reaction only occurs at the sides of the channel. For small R''_{ct} , the interfacial current is divided over the current collector and membrane region only when R'_S and R'_L are equal, but is otherwise localized at one side. Either situation gives a relatively high local interfacial current, which does not optimally leverage the suspension electrode concept and thus will not help to alleviate mass transfer limitations.

This means that the ratio between $1/(Vl_e)R_{ct}''$ and $R'_{S,L}$ is crucial for spreading the reaction over the whole channel and utilizing the suspension electrode to its full advantage. The suspension electrode would work well in case of a sluggish reaction, or in case of highly conductive solid and liquid phases that ensure that the Faradaic charge transfer is the dominant resistance. Alternatively, the solid and liquid phase resistances should be well-matched whenever they near the charge transfer resistance.

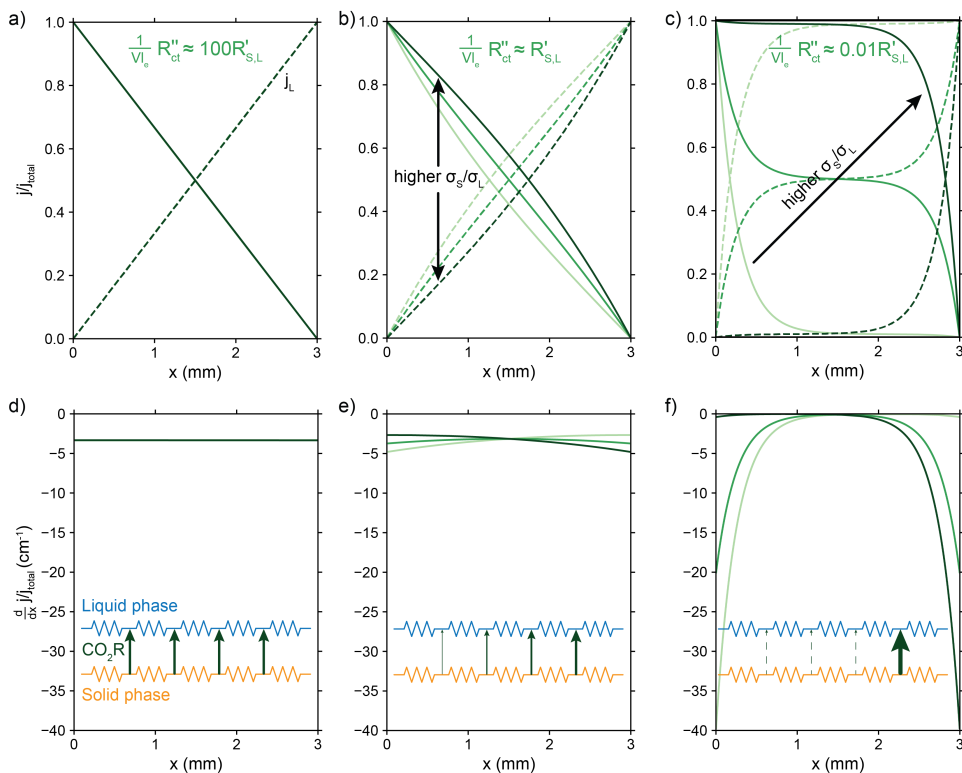


Figure 2.4: Modelled local currents throughout the electrolyzer channel for different ratios of solid and liquid conductivities and charge transfer resistance. Normalized solid and liquid currents (top figures), and the slope (bottom figures) of the solid current fraction that indicates the interfacial current and reaction in that region. A schematic representation of the TLM circuit is displayed at the bottom with the arrows indicating the intensity of the interfacial current and reaction in that region. We show the results for different ratios of solid (σ'_S) and liquid (σ'_L) phase conductivities. a)/d) $1/(Vl_e)R_{ct}''$ is a factor 100 higher than, b)/e) the same magnitude as, c)/f) and a factor 100 lower than R'_S and R'_L .

2.4.2. PARTICLE SIZE AND SHAPE IMPACT CONDUCTIVITY AND FLOWABILITY TRADE-OFF

As seen from the model, achieving electric and ionic conductivity that are sufficiently high to compete with the Faradaic charge transfer is essential for optimizing suspension electrodes. However, producing a high electric conductivity of the suspension with

good flowability is a well-known challenge.[43, 44] Raising the carbon loading is the most effective method for improving conductivity, but it also significantly lowers the flowability. However, we hypothesize that even though both conductivity and viscosity have a relation to enhanced particle-particle interaction, the relation is not necessarily linear and may differ for different materials.[54] Because both properties are highly particle-dependent, we measured the viscosity and conductivity of the three particle types used in this study. We combine the data to determine which particle type has the most favourable flowability-conductivity relation.

The rheology results for Activated Carbon (AC, 2-20 wt%), Carbon Black (CB, 2-15 wt%) and Glassy Carbon spheres (GyC, 2-40 wt%) suspensions are shown in Figure 2.5. Whereas the slurries of all particle types show shear thinning behaviour, we see a large difference in viscosity of several orders of magnitude. The irregularly shaped particles (AC and CB) cause significantly higher viscosity than the spherical particles (GyC) at the same loading. The CB suspension, which contains the smaller of the two irregularly shaped particle types, is the least flowable; this material displays such a high viscosity and paste-like consistency at 20 wt% that the sample could not be tested. The glassy carbon spheres show a considerably lower viscosity, with the most viscous GyC suspension of 40 wt% approximately matching the 15 wt% AC slurry. In addition to being of approximately the same size as the AC particles, the glassy carbon particles have a spherical shape with a smooth surface. This makes the contact areas between the particles smaller and the smoothness of the surface imposes less friction during a collision.[55] Our observations that smaller size and a more irregular shape cause higher viscosity in the carbon suspensions is in good agreement with existing literature.[55]

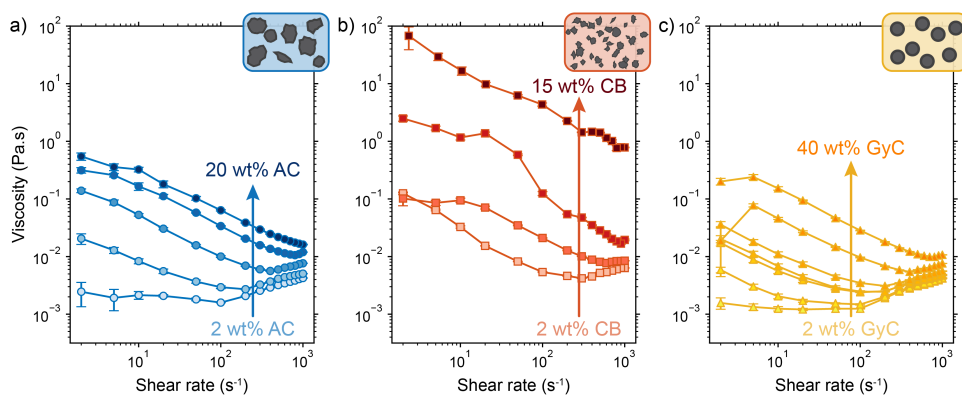


Figure 2.5: Measured viscosity for different shear rates and carbon loadings of a) activated carbon (AC), b) carbon black (CB), and c) glassy carbon spherical (GyC) suspensions. The inserts show an impression of the differences in size and shape between the particle types. We see significantly higher viscosities in smaller and irregularly shaped carbons.

Next, we consider the experimentally obtained electric conductivities in Figure 2.6a for all different concentrations of the various particles. As could be expected from the viscosity results, the glassy carbon spheres show the lowest conductivity due to lack of inter-particle contact. Following the same train of thought and considering the large

difference that was observed in viscosity between AC and CB, it is surprising that both suspension types show similar conductivity up to a concentration of 10 wt%, while CB surpasses AC only at a loading of 15 wt%. The sharp increase in conductivity between 10 and 15 wt% of CB suggests that the critical concentration for forming extensive percolation networks lies in this region.[31, 56] From this graph, one could select CB as the most conductive particle type. However, we should keep in mind that this carbon type also shows the highest viscosity by several orders of magnitude in comparison to the AC and, even more so, in comparison to the GyC suspensions.

We combined the data on rheology and conductivity to address this issue and explore which particle type has the most favourable conductivity-flowability relation. To incorporate the results of our measurements at different pump rates, we plotted the conductivities versus the imposed stress. The stress was estimated by calculating the shear rate in the flow channel at the employed flow speed and extracting the corresponding viscosity from the rheological data. We estimated the shear rate in the rectangular channel using equations (S3) and (S4) in the SI.[57]

The combined conductivity and rheology data are shown in Figure 2.6b. For the AC and CB suspensions, conductivity indeed increases with stress, but not at the same rate. The onset for increasing conductivity in the AC graph is at a considerably lower stress than in the CB graph, showing that the relation between stress and conductivity is indeed dependent on particle type. Although AC does not give the most conductive slurry, it does show a higher increase in conductivity with lower increase in viscosity, and thus a more favourable trade-off between conductivity and flowability. In contrast to Figure 2.6a, here AC appears to be the most suitable particle for a suspension electrode. A measurement with Ag NPs added to a 10 wt% suspension (with a ratio 3:1 AC:Ag) suggests that the Ag NPs can act as a conductive additive and increases the conductivity slightly without significantly influencing the flowability (see Figure S2.4).

Furthermore, Figure 2.6b shows the conductivity at three different pump rates for each particle type and loading, with the data points at higher stress corresponding to those at higher pump rates. Although all suspensions are shear thinning in the region of shear rates ($15\text{--}75\text{ s}^{-1}$) in which we conducted the conductivity measurements, faster pumping of AC suspensions increases the conductivity while decreasing the viscosity. This increased conductivity at faster pumping may be caused by more frequent collisions between particles or more collisions with the current collector at higher flow rates. The trend is different for the CB electrodes. These show an optimum in conductivity at the middle flow rate for most CB loadings, and the highest concentration CB (15 wt%) even causes the conductivity to drop for increased flow rate. We expect that this effect is caused by the interplay between more frequent collisions due to increased flow rate, the breaking of conductive networks when exceeding their yield stress[45], and a higher conductivity dependence on conductive networks due to lower surface area and capacitance compared to AC. Finally, the GyC suspensions are a special case, showing a similar viscosity at 40 wt% as AC at 15 wt% and almost no conductivity in the tested loading range. Although much higher concentrations can be used at high flowability, the conductivity is inferior to AC even for similar stress.

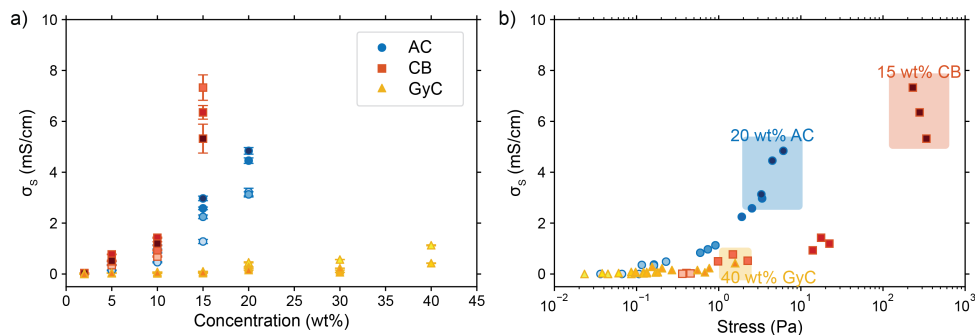


Figure 2.6: Measured conductivities and their dependence on a) carbon loading for AC, CB, and GyC suspensions (darker colours indicate higher flow rates, error bars give the error in the EIS fit) and on b) stress as a result of varying viscosity and shear rates (shear rates between 15 and 75 s^{-1} , as relevant for electrolysis experiments). The results show an increase in conductivity with loading for all carbon types. The relation between conductivity and stress is highly dependent on particle type and most favourable for AC suspensions.

2.4.3. AC AND CB GIVE GOOD MODELLED REACTION DISTRIBUTIONS

We implement the measured conductivities for all carbon types and loadings in the TLM, to determine the expected local current density and how well each suspension would be suited for use in a CO_2 electrolyzer. We used the particle-particle resistances (R_{p-p}) found with EIS and the ion conductivity of the electrolyte, adjusted with the Bruggeman equation (see SI), to define R'_S and R'_L in the TLM. We calculated R''_{ct} with [50, 58]

$$\frac{1}{R''_{ct}} = \frac{a j_0 n F}{RT} \quad (2.8)$$

in which a is the ratio of surface area per volume, j_0 the exchange current density (estimated as shown in SI), n is the number of electrons transferred in the reaction, and F , R , and T are the Faraday constant, universal gas constant and the temperature. For clarity, Figures 2.7a-c show the local current density in the solid phase only. The intersection with the y-axis gives the total current density, which yields the liquid current density via $j_L = j_{total} - j_S$. [59]

The total current shifts to larger values with higher carbon loadings due to lowered total resistance, showing that the loss of electrolyte volume and thus electrolyte conductivity is lower than the gain in solid conductivity upon raising the particle concentration. This is a direct consequence of a relatively low electric conductivity of suspensions (< 8 mS/cm, Figure 2.6) compared to the ionic conductivity that can be reached at high electrolyte concentrations (44 mS/cm at 0.5 M KHCO_3).

We saw that an even reaction distribution can be achieved if all three resistances are in the same order of magnitude, or R''_{ct} is the limiting resistance. Figure 2.7 shows the modelled local current densities (Figures 2.7a-c) and the corresponding slopes (Figures 2.7d-f) of AC, CB, and GyC suspensions at different carbon loadings. The values for R''_{ct} , R'_S and R'_L used in these simulations are listed in table S2.3. $1/(V l_e) R''_{ct}$ and R'_L are of the same order of magnitude in all situations, causing R'_S to be the determining factor in how well the Faradaic current is distributed over the channel. In case of AC and CB

suspensions, the particle loading can be increased sufficiently to lower R'_S into the same order of magnitude as R''_{ct} and R'_L , resulting in a more linear decrease in current density through the channel (Figures 7a and b) and a relatively constant slope (Figures 7d and e). This indicates that even reaction distributions and a significant Faradaic current throughout the whole channel can be achieved in suspensions of 15 and 20 wt% of AC, and 15 wt% of CB.

The resistances are even better matched at a lower electrolyte concentration (0.1 M, see Figure S2.6 in SI). This presents a trade-off: when lowering the electrolyte concentration, the total current is lower, but the current is more evenly distributed over the thickness of the cell, which could allow a higher Faradaic efficiency for CO₂ conversion products. We can extrapolate the TLM results to higher current densities by applying a higher voltage (Figures S7 and S8 for 0.5 and 0.1 M KHCO₃, respectively). This results in a similar shape for all carbon types and concentrations as for the original simulation at -1.5 V. This shows that the reaction distribution is mostly dependent on the ratio of R'_S and R'_L , and is not negatively influenced at higher voltages.

The less conductive GyC suspensions results in a much more localized current near the current collector and a lower total current density. The GyC conductivity is too low to drive the reaction deeper into the channel, even at very high loadings of 30 and 40 wt%. Therefore, we expect that CO₂ reduction can benefit from a suspension electrode consisting of AC or CB particles, of which AC is the most applicable due to its higher flowability.

2.4.4. SUSPENSION ELECTRODES SHOW LOW SELECTIVITY FOR CO₂ REDUCTION

We experimentally assessed several suspension compositions in our CO₂ electrolyzer setup. We show the achieved partial CO current densities in Figure 2.8. Although all suspensions show some activity for CO₂ reduction, they produce considerably larger amounts of H₂ (See Table S2.4 and Figure S2.10). We reached the highest partial CO current density of 2.8 mA/cm² in one experiment with 5 wt% CB, but in general the 15 wt% GyC suspension gave the most consistent trend in performance with the highest partial CO current density at 1.6 mA/cm². This is surprising, as we expected the GyC suspensions to have the lowest performance due to the significantly lower conductivity. Additionally, we expected to see a clear trend in performance with increased AC loading, based on our TLM results. Instead, all suspensions give a similar partial CO current density, with no differences in low and high conductivity, as can be seen clearly from the AC graph (Figure 8a) in which the 2 and 20 wt% AC suspensions reach roughly the same CO current density.

Due to this lack of trend in CO production with increased conductivity, we suspect that a different issue is outweighing the importance of suspension conductivity. This can be a number of engineering issues. For example, the average CO-selectivity is in the order of AC < CB < GyC, which follows the same trend as 1) the specific surface area of the powders, and 2) the concentrations of several metal contaminations in the powders (see Figure S2.11). This makes us suspect that the large amount of active sites provided by the carbon particles and metal contaminations catalyze the HER at the expense of CO₂ reduction. Although high-surface area carbons are often used for adsorption of CO

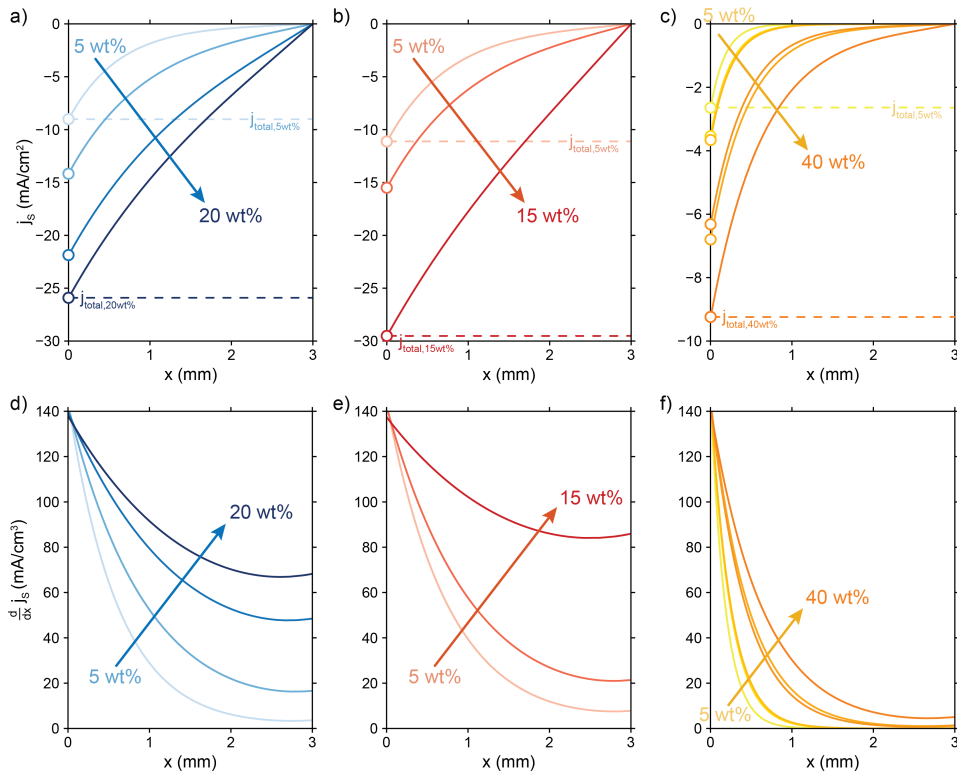


Figure 2.7: Modelled local current densities (top figures show j_s , j_L can be found via $j_L = j_s|_{x=0} - j_s|x$) and interfacial currents (bottom figures) throughout the electrolyzer channel for a/d) AC, b/e) CB and c/f) GyC slurries. The highest currents and best interfacial current distribution can be achieved in 20 wt% AC and 15 wt% CB suspensions, of which the AC suspension is the most applicable due to higher flowability. The CO₂ reduction reaction is localized near the current collector in all GyC suspensions. All simulations have been run at an R_{ct}'' of 10 $\Omega \cdot \text{cm}^3$ and an applied potential of -1.5 V versus the membrane (see SI for remaining input values).

and other compounds, the high FE for H₂ included in Table S2.4 shows that adsorption of CO (and other CO₂ reduction products) is not significantly lowering the j_{CO} that we observe. Additionally, we suspect that our system suffers from a poor CO₂ supply into the flow channel because of two likely causes. 1) Sparging CO₂ into the reservoir may be too slow a saturation method to keep up with the CO₂ consumption rate, causing the bulk CO₂ concentration to drop over time.[60] And 2) vortices indicating backflow were visible near the outlet inside the flow channel during experiments with the slightly more transparent suspensions., Therefore, we suspect that the viscous suspensions prevent efficient flushing with fresh (CO₂-rich) electrolyte in our flow channel design. This hypothesis is supported by an increase in partial current density up to 2.7-3.3 mA/cm² when using a 5 wt% AC suspension in combination with a smaller current collector area (Table S5). Using a smaller electrode area at the same current density lowers the CO₂ consumption and diminishes issues like slow CO₂-resaturation in the reservoir and in-

effective flushing of the flow channel with fresh electrolyte.

Although the TLM predicts two out of three suspension types to have sufficient conductivity for good performance, the practical issues described above are the likely cause for the inconsistency between the TLM predictions and the experimental CO₂ electrolysis results and complicate the engineering of good suspension electrodes. As a result, the suspensions could not match the performance of state of the art GDEs, which can reach current densities of -200 mA/cm^2 . Comparing GDE-based and suspension-based CO₂ electrolyzers, both technologies possess advantages and drawbacks in their operation. The silver loading per geometrical area of our system (7.5 mg/cm^2) is slightly higher than in typical carbon-based GDEs (1 mg/cm^2) before optimization. A lower Ag content (AC:Ag = 10:1) at 20 wt% solids produced similar low CO production (Table S6) which suggest that the amount of Ag is not critical. Hence, the total amount of silver in suspension electrode may be optimized to similar quantities to those in GDEs and significantly lower than in alternative technologies like silver-based GDEs that consist almost completely (97%) of silver.[61] Additionally, GDEs are complex structures to construct and they suffer from stability issues like carbon-degradation and electrowetting.[26–30] Suspension electrodes can be produced from cheap carbon powders and the Ag catalyst can be incorporated by simple mixing, but these capacitive materials often contain contaminations that catalyze the HER to compete with CO₂ reduction, and their flowability and stability during long-term operation are still under investigation.[62, 63] Flowable electrodes with a solid content of 5–20 wt%, depending on the particle type, are used throughout literature without significant clogging issues.[62, 64]

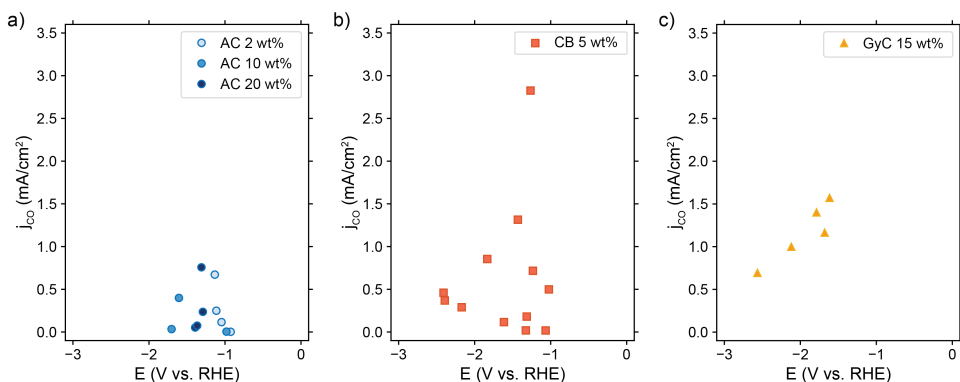


Figure 2.8: Resulting partial CO current densities (j_{CO}) in a) AC, b) CB, and c) GyC suspensions in 0.5 M KHCO₃, in which 1/4 of the solid content consisted of Ag NPs. The cell setup contained 3 mm thick flow channels, separated by a Selenion anion exchange membrane. In each experiment, a graphite or glassy carbon plate current collector was used, and the liquid flow rate was varied between 9 and 18 mm/s (see Table S2.4 for additional experimental conditions).

2.5. CONCLUSIONS

We modelled the local current densities in suspension electrodes with a Transmission Line Model (TLM), and experimentally determined the electrode performances for CO₂

reduction. Ideally, the Faradaic reaction is distributed evenly over the whole depth of the flowable electrode. We used the model to study the required conditions to achieve this situation. We varied the ratio of solid and liquid phase resistances, in combination with high and low charge transfer resistance. The reaction is most evenly distributed when either charge transfer is the dominant resistance, or all three resistances are of a similar magnitude. When the charge transfer resistance is significantly lower than the solid and liquid phase resistivities, the reaction is always localized at the edges, losing the benefits of using a suspension electrode.

Choosing a highly conductive suspension is therefore crucial for the electrolyzer performance. Although the conductivity is most easily improved by increasing the carbon loading, this also significantly affects the viscosity. Unfortunately, the maximum carbon loading that maintains flowability limits the conductivity to 8 mS/cm. Measuring the conductivity and rheology of small (CB) and larger irregularly shaped (AC) particles, and spherical (GyC) particles showed that the most viscous slurries do not necessarily yield the most conductive suspension. The relation between stress and conductivity is not linear and demonstrates that activated carbon has the highest conductivity when compared at equal stress, closely followed by carbon black.

When using experimentally obtained conductivities in the TLM, a good reaction distribution for the more conductive carbon materials is predicted. Instead, suspensions with carbon materials that feature lower conductivity should induce reactions only close to the current collector. Consequently, our modelling results predict the best catalytic performance in 20 wt% AC suspensions or 15 wt% CB.

However, our experiments showed no trends in achieved partial CO current density with carbon loading or conductivity, while we reached the best catalytic performance with j_{CO} of 2.8 and 1.6 mA/cm² with the least conductive suspensions (5 wt% CB and 15 wt% GyC). These contradicting results may have been caused by several engineering limitations, such as flow cell design, metal contaminations in the carbon powders, or poor CO₂-saturation of the electrolyte. We suspect that the CO₂ reduction is too sensitive to contaminations, competing hydrogen evolution at the large surface area of the carbon, and CO₂ dissolution limitations.

Although we achieved poor performance for CO₂ electrolysis, our modelling results suggest that suspension electrodes can be applied in other mass transfer limited reactions. This could be a step towards intensifying electrochemical conversion processes that currently suffer from low limiting currents and are not sensitive to competing reaction and contaminations.

2.6. SUPPORTING INFORMATION

The relevant data is available in the Zenodo repository under DOI 10.1039/D3YA00611E.

2.6.1 MODELLING

The parameters that were kept constant and used in all TLM simulations are shown in Table S2.1.

Table S2.1: Parameters that were kept constant in all TLM situations.

Parameter	value	unit
l_e	3	mm
A_C	8.16	cm ²
C'_{dl}	50	F/cm ³
f (with $\omega = 1 \text{ rad}\cdot f$)	45545	s ⁻¹
V_{app}	1.5	V

2.6.1.1 INVESTIGATING INFLUENCE OF REACTION AND CONDUCTION RESISTANCES

The parameters that were varied to evaluate the influence of the ratio of volumetric charge transfer resistance R''_{ct} to the solid and liquid phase resistances R'_S and R'_L on electrode utilization are summarized in Table S2.2. The unit of R''_{ct} is $\Omega\cdot\text{cm}^3$, (as it represents the charge transfer resistance per surface area) while the unit of R'_S and R'_L is Ω/cm (as it depends on the thickness of the channel). To make the units match, we need to normalize R''_{ct} . The values of R''_{ct} and $R'_{S,L}$ can be compared by adding a factor of

$$\frac{R'_{S,L}}{R''_{ct}} = \frac{\frac{1}{j_{S,L}A_C dx}}{\frac{1}{j_{S,L}a}} = \frac{a}{A_C dx} = \frac{\frac{A_C}{A_C l_e}}{A_C l_e} = \frac{1}{A_C l_e^2} = \frac{1}{V l_e} \quad (\text{S2.1})$$

where $a = \frac{A_C}{A_C l_e}$, $dx = l_e$ is the thickness of the flow channel, and V is the volume of the flow channel. In our system the factor $\frac{1}{V l_e}$ is close to unity at 1.36 cm^{-4} .

2.6.1.2 MEASURING SUSPENSION CONDUCTIVITY AND FLOWABILITY

Each suspension was mixed at a shear rate of 2000 s^{-1} before each measurement and between different shear rates. Pre-mixing was performed for 2 minutes, each shear rate of interest was applied for 3 minutes, and the suspension were again mixed at 2000 s^{-1} for 1 minute between each shear rate, in case of AC and GyC suspensions. This was changed to 3, 4 and 2 minutes, respectively, in case of CB suspensions. The results of such a measurement is shown in Figure S2.1 for 10 wt% AC, CB, and GyC suspensions in 0.5 M KHCO_3 . The highest stress plateaus correspond to the high-shear mixing modes at 2000 s^{-1} . The average values of the flat regions in the lower stress measurements, and the corresponding standard deviations, were used to produce Figure 2.5 in the manuscript.

The solid phase conductivity was calculated from the particle resistance (R_{p-p}), that were obtained by fitting the EIS data to the equivalent circuit described in Figure 2.3 of the manuscript, and cell dimensions via

$$\sigma = \left(R_{p-p} \frac{A_C}{l_e} \right)^{-1} \quad (\text{S2.2})$$

Table S2.2: Suspension parameters used to find the influence of the ratio between reaction and conduction resistance on electrode utilization.

Ratios	R''_{ct} $\Omega \cdot \text{cm}^3$	R'_S Ω/cm	R'_L Ω/cm
$\frac{1}{v l_e} R''_{ct} \approx 100 R'_{S,L}$			
$R'_S = 99\%$ of $R'_S + R'_L$	1000	19.8	0.2
$R'_S = 50\%$ of $R'_S + R'_L$	1000	10	10
$R'_S = 1\%$ of $R'_S + R'_L$	1000	0.2	19.8
$\frac{1}{v l_e} R''_{ct} \approx R'_{S,L}$			
$R'_S = 99\%$ of $R'_S + R'_L$	10	19.8	0.2
$R'_S = 50\%$ of $R'_S + R'_L$	10	10	10
$R'_S = 1\%$ of $R'_S + R'_L$	10	0.2	19.8
$\frac{1}{v l_e} R''_{ct} \approx 0.01 R'_{S,L}$			
$R'_S = 99\%$ of $R'_S + R'_L$	0.1	19.8	0.2
$R'_S = 50\%$ of $R'_S + R'_L$	0.1	10	10
$R'_S = 1\%$ of $R'_S + R'_L$	0.1	0.2	19.8

Some EIS results and fits for 10 wt% AC, CB, and GyC suspensions in 0.5 M KHCO_3 are shown in Figure S2.2.

These results were combined with rheology data to produce Figure 2.6. The rheology measurements were not performed at the exact wall shear rates exerted by the suspensions inside the flow cell. We estimated the average wall shear rate $\dot{\gamma}$ in the rectangular channel with equations S2.3 and S2.4.[57]

$$\dot{\gamma} = \frac{QP\lambda}{8A^2} \quad (\text{S2.3})$$

$$\lambda = \frac{24}{\left(\left(1 - 0.351 \frac{b}{a} \right) \left(1 + \frac{b}{a} \right) \right)^2} \quad (\text{S2.4})$$

which is valid when $\frac{b}{a} < 1.0$, where a and b are the lengths of the long and short sides, respectively. Q is the volumetric flow rate, P is the wetted perimeter, and A the cross-sectional area of the flow channel.

In order to plot the measured conductivity against the stress under flow conditions, we plotted all measured viscosities at shear rates between 2 and 100 s^{-1} and fitted a power function through these datapoints, as shown in Figure S2.3. We estimated the viscosity during pumping by inserting the relevant wall shear rate (resulting from equations S2.2 and S2.3) into this function. Finally, the wall shear stress was calculated by multiplying the viscosity with the shear rate. These results were used in Figure 2.6b.

2.6.1.3 MODELLING REACTION DISTRIBUTION IN REAL SUSPENSIONS

The solid (R'_S) and liquid (R'_L) resistances per unit length used in the simulations for the real carbon suspensions can be calculated with[50]

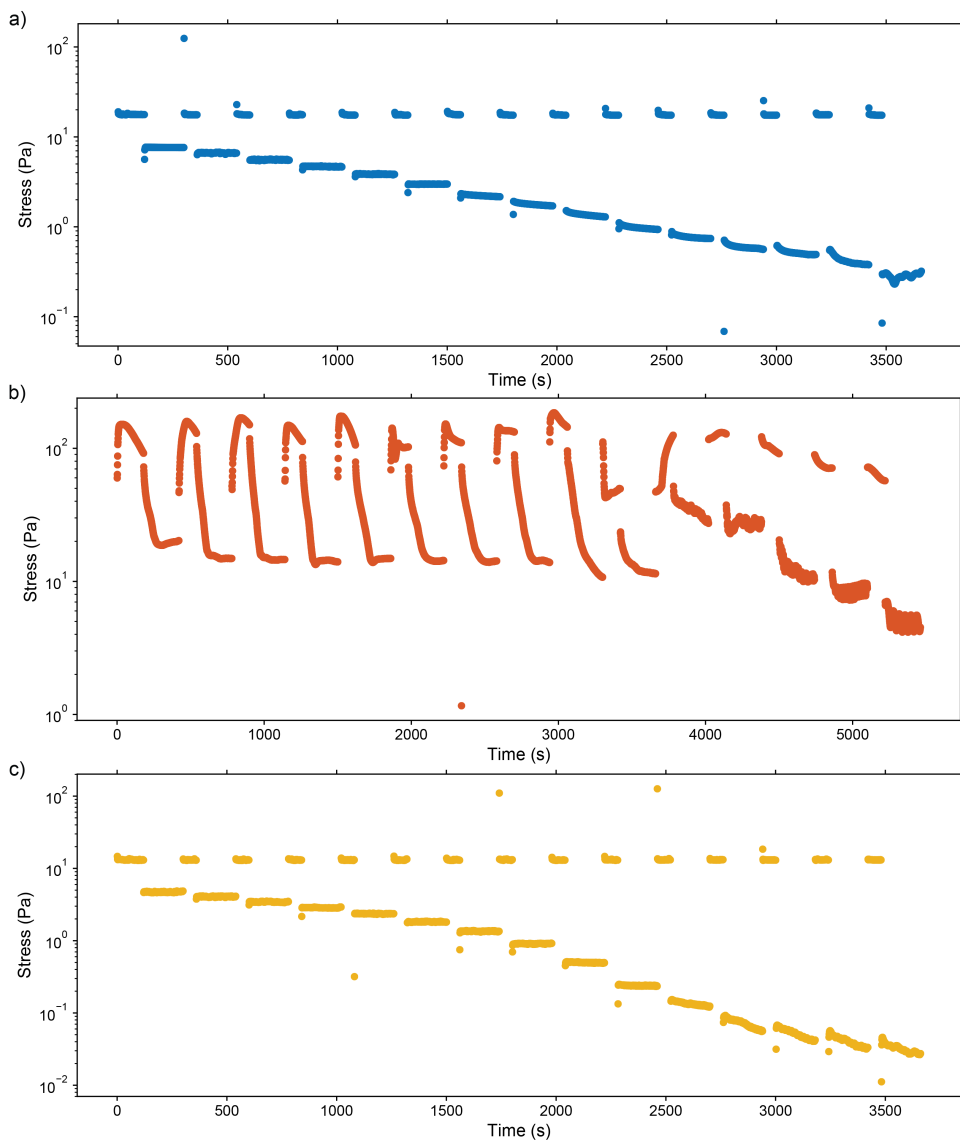


Figure S2.1: Measured stress over time at applied shear rates between 1000 and 2 s^{-1} for 10 wt% a) AC, b) CB, and c) GyC suspensions in 0.5 M KHCO_3 . The suspensions were pre-sheared at 2000 s^{-1} before each new shear rate to prevent memory and sedimentation effects. The values of the applied shear rates can be found in Figure 2.5 in the main paper.

$$R'_S = \frac{R}{l_e} = \frac{1}{A_C \sigma} \quad (\text{S2.5})$$

in which R is the solid resistance, l_e the thickness of the channel, A_C is the cross-sectional area of

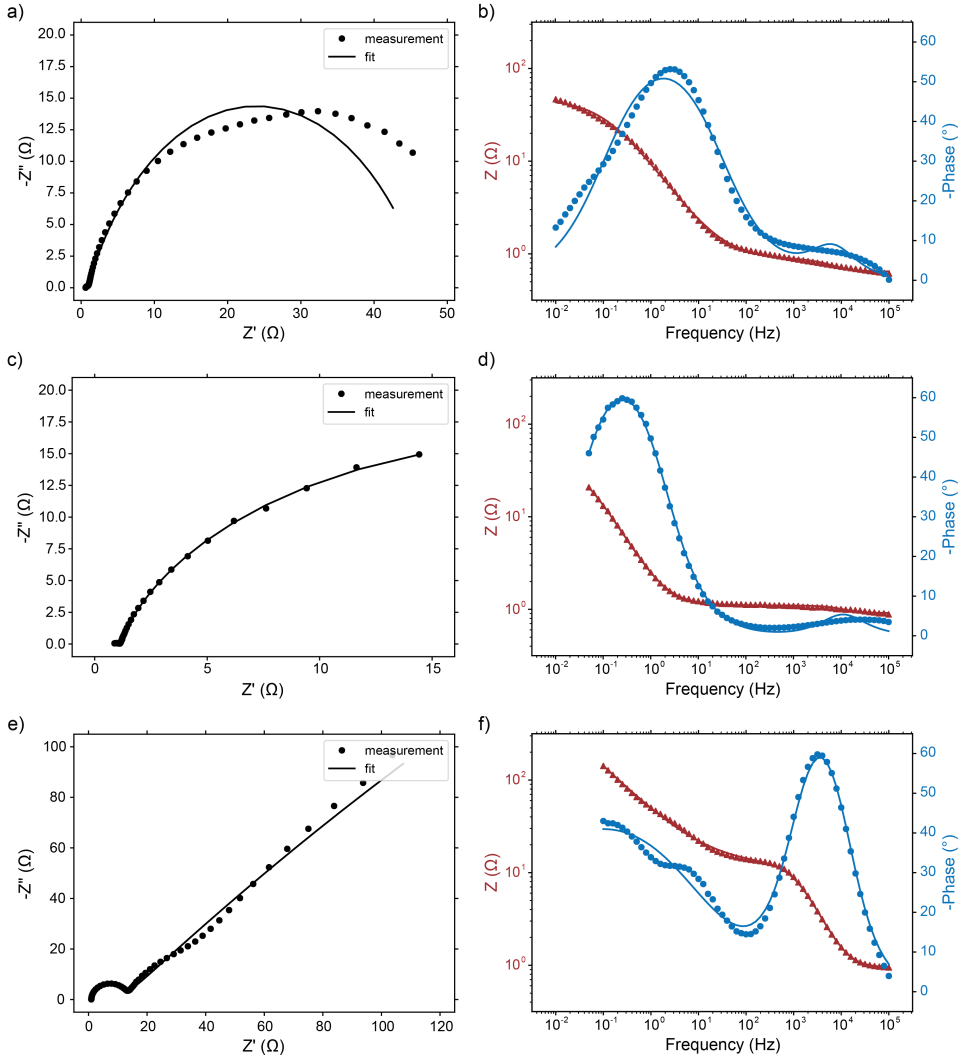


Figure S2.2: Typical EIS measurements and fitting, represented in Nyquist (left) and Bode (right). Results are shown for 10 wt% AC (a/b), CB (c/d), and GyC (e/f) suspensions in 0.5 M KHCO₃.

the electrode and σ is the conductivity of the solid phase. We inserted R_{p-p} for R to account for the voids and changeability of the electrically conductive carbon networks. All calculated values for R'_S can be found in Table S2.3.

The values for R'_L were calculated in a similar manner with

$$R'_L = \frac{R}{l_e} = \frac{\tau}{pA_C\sigma_L} \quad (\text{S2.6})$$

$$\tau = p^{-\frac{1}{2}} \quad (\text{S2.7})$$

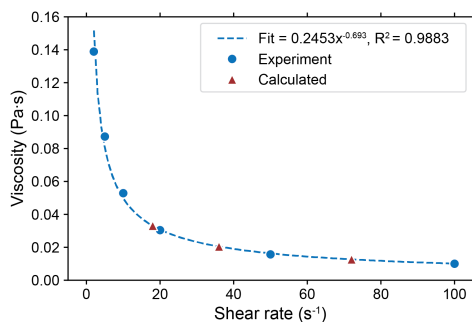


Figure S2.3: Measured viscosities of a 10 wt% AC suspension in 0.5 M KHCO_3 in the stress regime relevant for flow inside the CO_2 electrolysis cell. These datapoints and fit were used to calculate the stress at the flow rates used during the EIS experiments to produce Figure 2.6 in our paper.

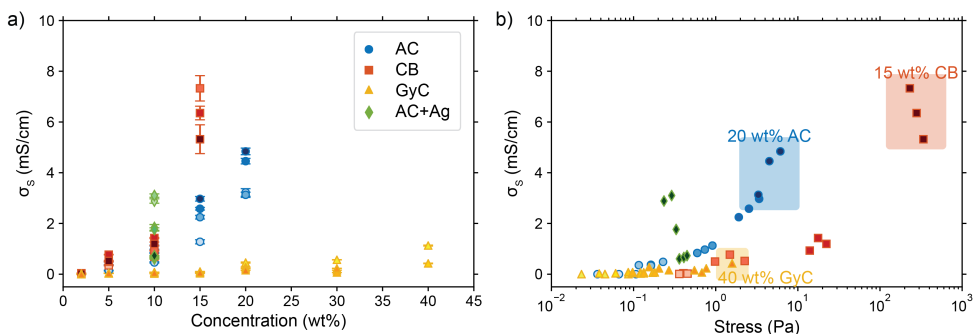


Figure S2.4: Influence of adding Ag NPs to a 10 wt% solids (3:1 AC:Ag) suspension in 0.5 M KHCO_3 on a) the suspension conductivity, and b) the relation between stress and conductivity. Note that adding Ag NPs increases conductivity while the stress remains approximately constant.

in which σ_L is the electrolyte conductivity, p is the porosity and τ is the tortuosity given by the Bruggeman relation, which are included to account for the solid fraction in the electrolyte, which is not ionically conductive.[65] We used conductivities of 0.044 and 0.010 S/cm for the 0.5 and 0.1 M KHCO_3 electrolytes, respectively[66] (calculated at 0.5 and 0.1 M KHCO_3 with 30 mM CO_2). We calculated the porosity with the volume fraction of carbon in water, for which we weighed a known volume of 10 wt% AC, and CB suspensions, assuming a water density of 0.997 g/cm^3 . This resulted in densities of 1.9 g/cm^3 for AC and 1.8 g/cm^3 for CB. We used a density of 1.5 g/cm^3 for the GyC particles.[67] After which the porosity can be calculated as $p = 1 - \phi_{\text{carbon}}$, with ϕ_{carbon} the volume fraction of carbon in the suspension. The resulting values for R'_L are shown in Table S2.3.

We calculated R''_{ct} with equation 2.8 and estimated the exchange current from the Tafel plots shown in Figure S2.5. We used the overpotential range in which we observed CO formation to make a linear fit and extract the exchange current, given by the intercept with the y-axis. This resulted in two R''_{ct} values of 4.6 and $13.3 \Omega \cdot \text{cm}^3$. We used $10 \Omega \cdot \text{cm}^3$ in our suspension simulations.

The simulation results for the suspensions in 0.1 M KHCO_3 are shown in Figure S2.5. The interfacial current graphs are slightly flatter than the results in 0.5 M KHCO_3 , indicating a better

Table S2.3: Suspension parameters used to find the influence of the ratio between reaction and conduction resistance on electrode utilization.

Carbon loading wt%	R''_{ct} $\Omega \cdot \text{cm}^3$	R'_S Ω/cm	R'_L Ω/cm	
			0.1 M KHCO_3	0.5 M KHCO_3
AC				
5	10	317.1	12.6	2.9
10	10	125.4	13.2	3
15	10	47.1	13.8	3.2
20	10	29.6	14.5	3.3
CB				
5	10	205.7	12.7	2.9
10	10	103.5	13.3	3
15	10	19.4	13.9	3.2
GyC				
5	10	3754.7	12.8	2.9
10	10	2119.2	13.5	3.1
15	10	1959.8	14.3	3.3
20	10	557.7	15.3	3.5
30	10	824.4	17.7	4
40	10	288.9	21	4.8

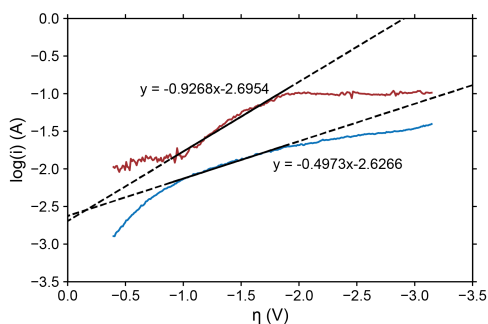


Figure S2.5: Tafel plots and linear fits for two CO_2 reduction experiments. The y-intercept gives the exchange current i_0 that was used for calculating R''_{ct} .

reaction distribution through the channel. However, the top figures show that the achievable total current is lower than in the higher concentration electrolyte, which is due to the higher total resistance. Although the interfacial current is spread out more evenly in all suspensions compared to the case with a higher electrolyte concentration, this does not significantly drive the reaction in GyC suspensions to the middle of the channel. The reaction in GyC suspensions is still highly localized near the current collector.

In addition, Figures S2.6 and S2.7 show that the simulated currents inside carbon suspensions in 0.5 and 0.1 M KHCO_3 can be increased by applying a higher potential. Running the TLM at -10 V increases the current density, while the shapes of the graphs are very similar to the 0.5 and

0.1 M KHCO_3 cases at -1.5 V applied potential. This shows that the current distribution is mainly determined by the ratio of the solid and liquid phase resistances (R'_S and R'_L) instead of by the applied potential.

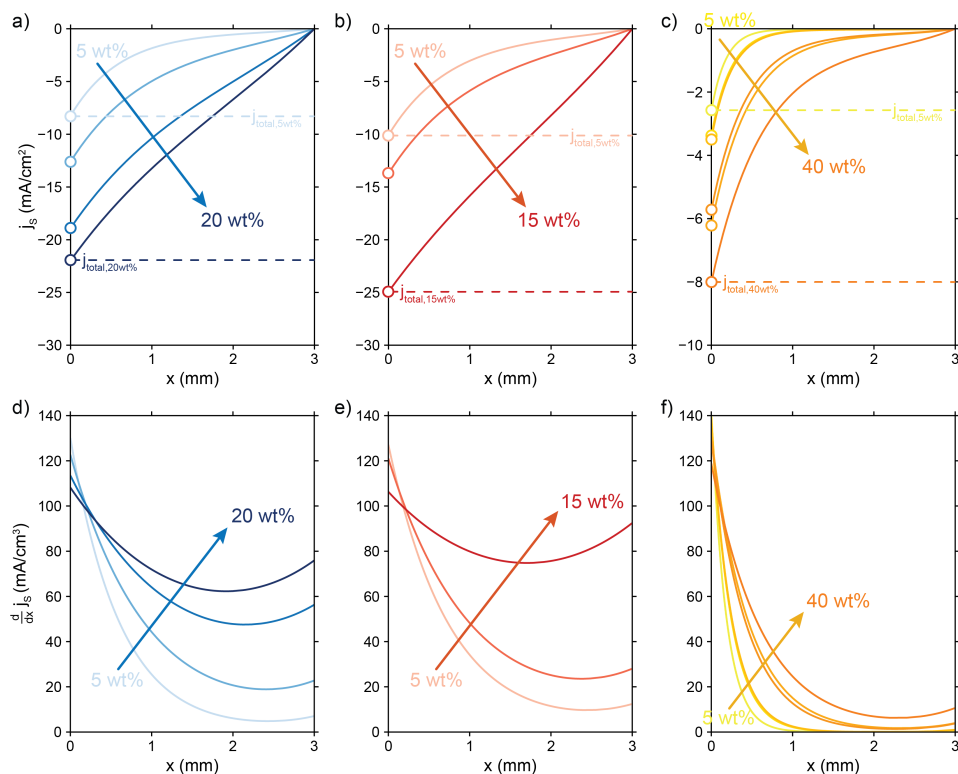


Figure S2.6: Modelled local current densities (top figures show j_S , j_L can be found via $j_L = j_S|_{x=0} - j_S|_x$) and interfacial currents (bottom figures) throughout the electrolyzer channel for a)/d) AC, b)/e) CB and c)/f) GyC slurries in 0.1 M KHCO_3 . Although the total current are lower than in 0.5 M KHCO_3 electrolyte due to higher total resistance, the reaction distribution through the channel is slightly more uniform.

2.6.2 CO_2 REDUCTION EXPERIMENTS

All CO_2 reduction experiments were performed with the setup shown in Figure S2.9a. The system is airtight to allow for inline measurements of gas compositions. Figure S2.9b shows the cell configuration and dimensions. Table S2.4 shows all experimental conditions and results. The partial current densities towards H_2 are shown in Figure S2.10.

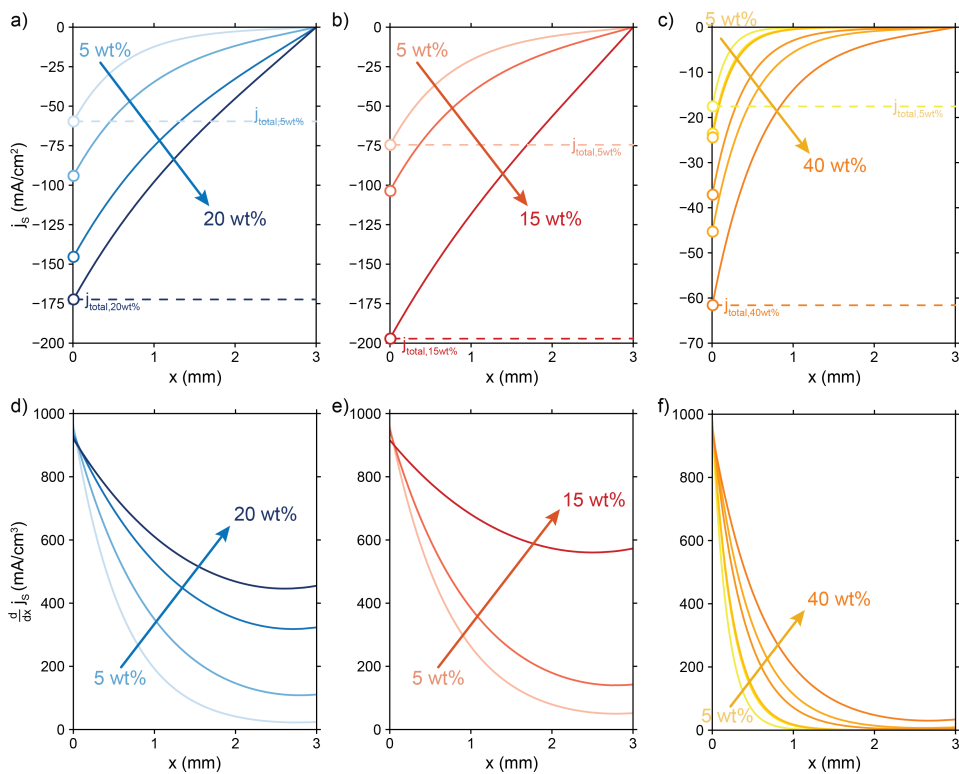


Figure S2.7: Modelled local current densities (top row shows j_s , $j_L = j_s|_{x=0} - j_s|_x$) and interfacial currents (bottom) in the electrolyzer channel for a)/d) AC, b)/e) CB and c)/f) GyC slurries in 0.5 M KHCO₃ at an applied current of -10 V to increase the current density.

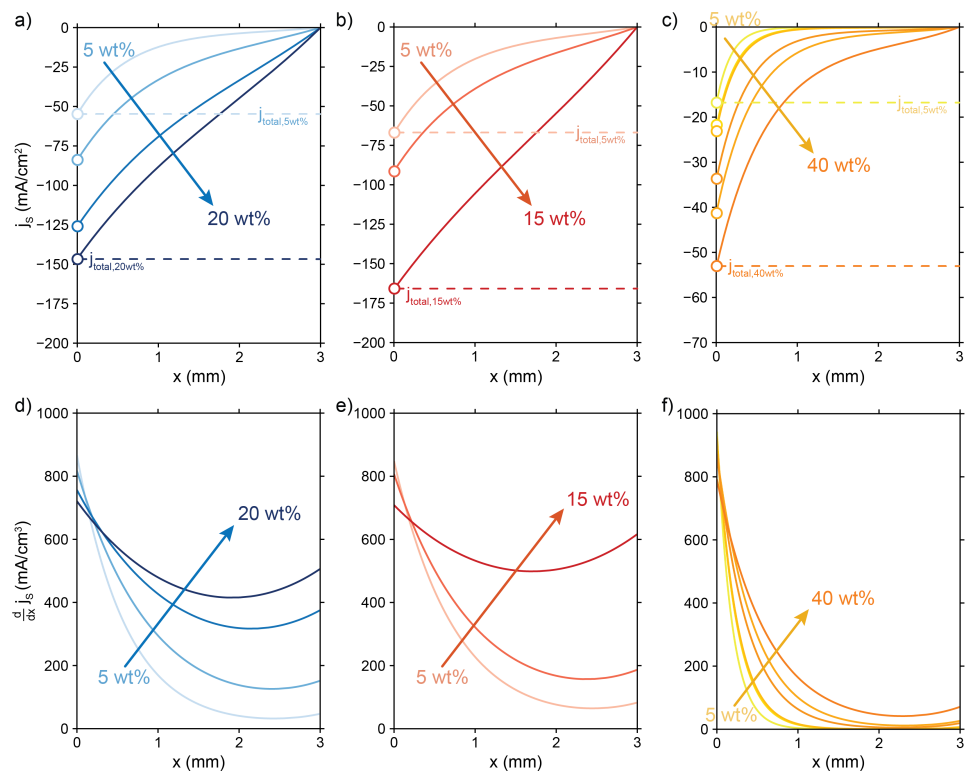


Figure S2.8: Modelled local current densities (top panels shows j_s , $j_L = j_s|_{x=0} - j_s|x$) and interfacial currents (bottom panels) in the electrolyzer channel for a) d) AC, b) e) CB and c) f) GyC slurries in 0.1 M KHCO₃ at an applied current of -10 V to increase the current density.

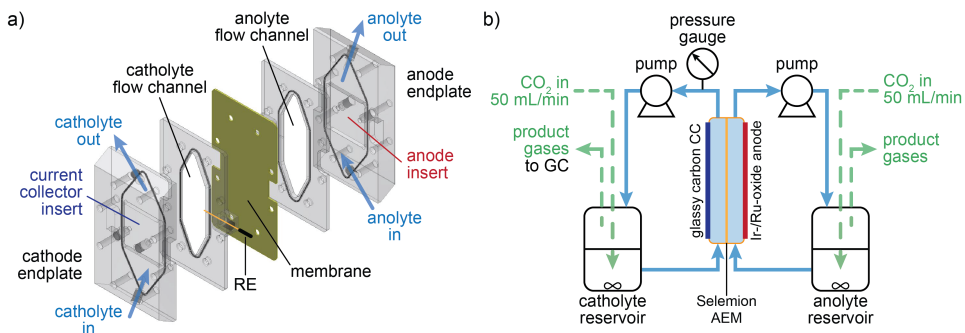


Figure S2.9: Illustration of the a) flow cell and b) setup used for CO₂ electrolysis.

Table S2.4: Experimental conditions and results for the performed CO₂ reduction experiments.

Carbon loading wt%	Run nr.	Current collector material	Flow rate mm/s	j_{applied} mA/cm ²	FE CO (%)	FE H ₂ %	E vs. RHE V
AC							
2	1	Graphite	9	-25	2.7	80.8	-1.1
2	2	Graphite	9	-50	0.5	98.2	-1.1
2	3	Graphite	9	-50	0.2	99.6	-1
2	4	Graphite	9	-25	0	95.8	-0.9
10	1	Glassy carbon	18	-50	0.8	89.2	-1.6
10	2	Glassy carbon	18	-2.5	0.2	39.6	-1
10	3	Glassy carbon	18	-25	0.1	87.5	-1.7
20	1	Graphite	9	-25	3	84.1	-1.3
20	2	Graphite	9	-25	0.9	76.6	-1.3
20	3	Graphite	9	-50	0.1	89.8	-1.4
20	4	Graphite	9	-50	0.1	87.6	-1.4
CB							
5	1	Graphite	18	-50	0.4	95.4	-1.3
5	2	Graphite	9	-50	5.7	89.5	-1.3
5	3	Graphite	9	-25	2	92.2	-1
5	4	Graphite	9	-100	0.7	100.8	-1.2
5	1	Glassy carbon	18	-50	1.7	93.6	-1.8
5	2	Glassy carbon	18	-10	0.2	94.1	-1.1
5	3	Glassy carbon	18	-100	1.3	99.3	-1.4
5	4	Glassy carbon	18	-50	0	95.8	-1.3
5	1	Glassy carbon	18	-50	0.8	81.4	-2.4
5	2	Glassy carbon	18	-25	0.5	85.5	-1.6
5	3	Glassy carbon	18	-100	0.5	100.1	-2.4
5	4	Glassy carbon	18	-50	0.6	89.6	-2.2
GyC							
15	1	Glassy carbon	18	-50	2.1	87.2	-2.1
15	2	Glassy carbon	18	-100	0.7	85.2	-2.6
15	3	Glassy carbon	18	-25	5.8	66.1	-1.8
15	4	Glassy carbon	9	-25	4.9	68.7	-1.7
15	5	Glassy carbon	36	-25	6.5	65.3	-1.6

Table S2.5: Experimental conditions and results of CO₂R on an AC suspension using current collector with a 10 times smaller area.

Carbon loading wt%	Run nr.	Current collector material	Flow rate mm/s	j_{applied} mA/cm ²	FE CO %	FE H ₂ %	E vs. RHE V
5	1	Graphite	9	-22	13.8	47.4	-1.2
5	2	Graphite	9	-44	6.1	74.7	-1.5

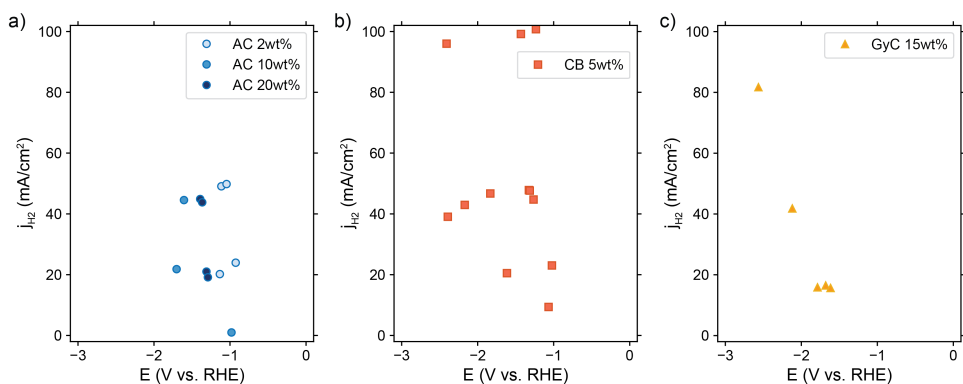


Figure S2.10: Resulting partial H_2 current densities in a) AC, b) CB, and c) GyC suspensions, under the reaction conditions listed in Table S2.4.

Table S2.6: Comparison of achieved partial CO current density for different amounts of Ag nanopowder per electrolyte weight.

Solids loading wt%	AC:Ag wt ratio	Ag concentration g/g electrolyte	j_{applied} mA/cm ²	j_{CO} mA/cm ²
20	10:1	0.023	-25, -25, -50, -50	-0.8, -0.2, -0.1, -0.1
2	3:1	0.005	-25, -50, -50, -25	-0.7, -0.2, -0.1, -0.0

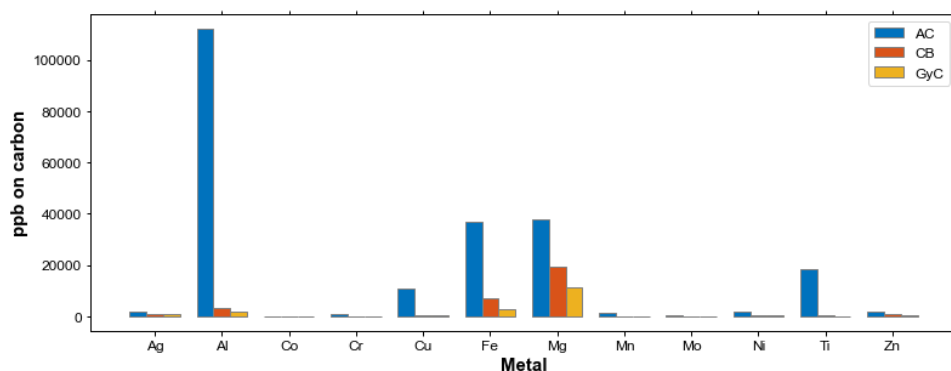


Figure S2.11: Metal contaminations on AC, CB, and GyC powders as measured with ICP-MS.

REFERENCES

- [1] Geoffrey Hammond and Marcus Newborough. "Glasgow climate pact: a step on the way towards a lower carbon dioxide world". In: *Proceedings of the Institution of Civil Engineers - Civil Engineering* 175.1 (2022), pp. 8–8.
- [2] Matthew Jouny, Wesley Luc, and Feng Jiao. "General Techno-Economic Analysis of CO₂ Electrolysis Systems". In: *Industrial & Engineering Chemistry Research* 57.6 (2018), pp. 2165–2177.
- [3] Phil De Luna, Christopher Hahn, Drew Higgins, Shaffiq A. Jaffer, Thomas F. Jaramillo, and Edward H. Sargent. "What would it take for renewably powered electrosynthesis to displace petrochemical processes?" In: *Science* 364.6438 (2019), eaav3506.
- [4] Alexander Otto, Thomas Grube, Sebastian Schiebahn, and Detlef Stolten. "Closing the loop: captured CO₂ as a feedstock in the chemical industry". In: *Energy & Environmental Science* 8.11 (2015), pp. 3283–3297.
- [5] David W. Keith, Geoffrey Holmes, David St. Angelo, and Kenton Heidel. "A Process for Capturing CO₂ from the Atmosphere". In: *Joule* 2.8 (2018), pp. 1573–1594.
- [6] R. Sharifian, R. M. Wagterveld, I. A. Digdaya, C. Xiang, and D. A. Vermaas. "Electrochemical carbon dioxide capture to close the carbon cycle". In: *Energy & Environmental Science* 14.2 (2021), pp. 781–814.
- [7] Sumit Verma, Byoungsu Kim, Huei-Ru "Molly" Jhong, Sichao Ma, and Paul J. A. Kenis. "A Gross-Margin Model for Defining Technoeconomic Benchmarks in the Electroreduction of CO₂". In: *ChemSusChem* 9.15 (2016), pp. 1972–1979.
- [8] Sahil Garg, Mengran Li, Adam Z. Weber, Lei Ge, Liye Li, Victor Rudolph, Guoxiong Wang, and Thomas E. Rufford. "Advances and challenges in electrochemical CO₂ reduction processes: an engineering and design perspective looking beyond new catalyst materials". In: *Journal of Materials Chemistry A* 8.4 (2020), pp. 1511–1544.
- [9] Eric W. Lees, Benjamin A. W. Mowbray, Fraser G. L. Parlane, and Curtis P. Berlinguette. "Gas diffusion electrodes and membranes for CO₂ reduction electrolyzers". In: *Nature Reviews Materials* 7.1 (2022), pp. 55–64.
- [10] David M. Weekes, Danielle A. Salvatore, Angelica Reyes, Aoxue Huang, and Curtis P. Berlinguette. "Electrolytic CO₂ Reduction in a Flow Cell". In: *Accounts of Chemical Research* 51.4 (2018), pp. 910–918.
- [11] N. Gupta, M. Gattrell, and B. MacDougall. "Calculation for the cathode surface concentrations in the electrochemical reduction of CO₂ in KHCO₃ solutions". In: *Journal of Applied Electrochemistry* 36.2 (2006), pp. 161–172.
- [12] Min Liu, Yuanjie Pang, Bo Zhang, Phil De Luna, Oleksandr Voznyy, Jixian Xu, Xueli Zheng, Cao Thang Dinh, Fengjia Fan, Changhong Cao, F. Pelayo García de Arquer, Tina Saberi Safaei, Adam Mepham, Anna Klinkova, Eugenia Kumacheva, Tobin Filleter, David Sinton, Shana O. Kelley, and Edward H. Sargent. "Enhanced electrocatalytic CO₂ reduction via field-induced reagent concentration". In: *Nature* 537.7620 (2016), pp. 382–386.

- [13] Thomas Burdyny and Wilson A. Smith. "CO₂ reduction on gas-diffusion electrodes and why catalytic performance must be assessed at commercially-relevant conditions". In: *Energy & Environmental Science* 12.5 (2019), pp. 1442–1453.
- [14] Lorenz M. Baumgartner, Aron Kahn, Maxime Hoogland, Jorrit Bleeker, Wolter F. Jager, and David A. Vermaas. "Direct imaging of local pH reveals bubble-induced mixing in a CO₂ electrolyzer". In: *ACS Sustainable Chemistry & Engineering* 11.28 (2023), pp. 10430–10440.
- [15] Thomas Burdyny, Percival J. Graham, Yuanjie Pang, Cao-Thang Dinh, Min Liu, Edward H. Sargent, and David Sinton. "Nanomorphology-Enhanced Gas-Evolution Intensifies CO₂ Reduction Electrochemistry". In: *ACS Sustainable Chemistry & Engineering* 5.5 (2017), pp. 4031–4040.
- [16] Tengfei Li, Eric W. Lees, Maxwell Goldman, Danielle A. Salvatore, David M. Weekes, and Curtis P. Berlinguette. "Electrolytic Conversion of Bicarbonate into CO in a Flow Cell". In: *Joule* 3.6 (2019), pp. 1487–1497.
- [17] Yuguang C. Li, Geonhui Lee, Tiange Yuan, Ying Wang, Dae-Hyun Nam, Ziyun Wang, F. Pelayo García de Arquer, Yanwei Lum, Cao-Thang Dinh, Oleksandr Voznyy, and Edward H. Sargent. "CO₂ Electroreduction from Carbonate Electrolyte". In: *ACS Energy Letters* 4.6 (2019), pp. 1427–1431.
- [18] Drew Higgins, Christopher Hahn, Chengxiang Xiang, Thomas F. Jaramillo, and Adam Z. Weber. "Gas-Diffusion Electrodes for Carbon Dioxide Reduction: A New Paradigm". In: *ACS Energy Letters* 4.1 (2019), pp. 317–324.
- [19] Byoungsu Kim, Febrian Hillman, Miho Ariyoshi, Shigenori Fujikawa, and Paul J. A. Kenis. "Effects of composition of the micro porous layer and the substrate on performance in the electrochemical reduction of CO₂ to CO". In: *Journal of Power Sources* 312 (2016), pp. 192–198.
- [20] Lei Ge, Hesamoddin Rabiee, Mengran Li, Siddhartha Subramanian, Yao Zheng, Joong Hee Lee, Thomas Burdyny, and Hao Wang. "Electrochemical CO₂ reduction in membrane-electrode assemblies". In: *Chem* 8.3 (2022), pp. 663–692.
- [21] Shofu Matsuda, Shota Yamanaka, and Minoru Umeda. "Influence of Water Molecules on CO₂ Reduction at the Pt Electrocatalyst in the Membrane Electrode Assembly System". In: *ACS Applied Materials & Interfaces* 15.36 (2023), pp. 42676–42684.
- [22] Lien-Chun Weng, Alexis T. Bell, and Adam Z. Weber. "Towards membrane-electrode assembly systems for CO₂ reduction: a modeling study". In: *Energy & Environmental Science* 12.6 (2019), pp. 1950–1968.
- [23] Yuefeng Song, Xiaomin Zhang, Kui Xie, Guoxiong Wang, and Xinhe Bao. "High-Temperature CO₂ Electrolysis in Solid Oxide Electrolysis Cells: Developments, Challenges, and Prospects". In: *Advanced Materials* 31.50 (2019), p. 1902033.
- [24] Elif Tezel, Ariel Whitten, Genevieve Yarema, Reinhard Denecke, Jean-Sabin McEwen, and Eranda Nikolla. "Electrochemical Reduction of CO₂ using Solid Oxide Electrolysis Cells: Insights into Catalysis by Nonstoichiometric Mixed Metal Oxides". In: *ACS Catalysis* 12.18 (2022), pp. 11456–11471.

- [25] Lixiao Zhang, Shiqing Hu, Xuefeng Zhu, and Weishen Yang. “Electrochemical reduction of CO₂ in solid oxide electrolysis cells”. In: *Journal of Energy Chemistry* 26.4 (2017), pp. 593–601.
- [26] Lorenz M. Baumgartner, Christel I. Koopman, Antoni Forner-Cuenca, and David A. Vermaas. “Narrow pressure stability window of gas diffusion electrodes limits the scale-up of CO₂ electrolyzers”. In: *ACS Sustainable Chemistry & Engineering* 10.14 (2022), pp. 4683–4693.
- [27] Bert De Mot, Jonas Hereijgers, Miguel Duarte, and Tom Breugelmans. “Influence of flow and pressure distribution inside a gas diffusion electrode on the performance of a flow-by CO₂ electrolyzer”. In: *Chemical Engineering Journal* 378 (2019), p. 122224.
- [28] Bert De Mot, Mahinder Ramdin, Jonas Hereijgers, Thijs J. H. Vlugt, and Tom Breugelmans. “Direct Water Injection in Catholyte-Free Zero-Gap Carbon Dioxide Electrolyzers”. In: *ChemElectroChem* 7.18 (2020), pp. 3839–3843.
- [29] Kostadin V. Petrov, Justin C. Bui, Lorenz Baumgartner, Lien-Chun Weng, Sarah M. Dischinger, David M. Larson, Daniel J. Miller, Adam Z. Weber, and David A. Vermaas. “Anion-exchange membranes with internal microchannels for water control in CO₂ electrolysis”. In: *Sustainable Energy & Fuels* 6.22 (2022), pp. 5077–5088.
- [30] Kailun Yang, Recep Kas, Wilson A. Smith, and Thomas Burdyny. “Role of the Carbon-Based Gas Diffusion Layer on Flooding in a Gas Diffusion Electrode Cell for Electrochemical CO₂ Reduction”. In: *ACS Energy Letters* 6.1 (2021), pp. 33–40.
- [31] Alexandra Rommerskirchen, Anna Kalde, Christian J. Linnartz, Leon Bongers, Georg Linz, and Matthias Wessling. “Unraveling charge transport in carbon flow-electrodes: Performance prediction for desalination applications”. In: *Carbon* 145 (2019), pp. 507–520.
- [32] Volker Presser, Christopher R. Dennison, Jonathan Campos, Kevin W. Knehr, Emin C. Kumbur, and Yury Gogotsi. “The Electrochemical Flow Capacitor: A New Concept for Rapid Energy Storage and Recovery”. In: *Advanced Energy Materials* 2.7 (2012), pp. 895–902.
- [33] Faiza Summer, Vahur Zadin, S. Sunjai Nakshatharan, Alvo Aabloo, and Janno Torop. “Optimization of Electrochemical Flow Capacitor (EFC) design via finite element modeling”. In: *Journal of Energy Storage* 29 (2020), p. 101304.
- [34] Alessandro Brilloni, Federico Poli, Giovanni Emanuele Spina, Damiano Genovese, Giorgia Pagnotta, and Francesca Soavi. “Improving the Electrical Percolating Network of Carbonaceous Slurries by Superconcentrated Electrolytes: An Electrochemical Impedance Spectroscopy Study”. In: *ACS Applied Materials & Interfaces* 13.11 (2021), pp. 13872–13882.
- [35] Hongning Chen, Yao Liu, Xuefeng Zhang, Quan Lan, Yue Chu, Yongliang Li, and Qixing Wu. “Single-component slurry based lithium-ion flow battery with 3D current collectors”. In: *Journal of Power Sources* 485 (2021), p. 229319.

- [36] Francesca Soavi, Alessandro Brilloni, Francesca De Giorgio, and Federico Poli. “Semi-solid lithium/oxygen flow battery: an emerging, high-energy technology”. In: *Current Opinion in Chemical Engineering* 37 (2022), p. 100835.
- [37] Jie Ma, Chunxiao Zhai, and Fei Yu. “Review of flow electrode capacitive deionization technology: Research progress and future challenges”. In: *Desalination* 564 (2023), p. 116701.
- [38] Wannan Zhang, Wenchao Xue, Kang Xiao, Chettiyappan Visvanathan, Jialing Tang, and Lu Li. “Selection and optimization of carbon-based electrode materials for flow-electrode capacitive deionization”. In: *Separation and Purification Technology* 315 (2023), p. 123649.
- [39] C. Borsje, T. Sleutels, C. J. N. Buisman, and A. ter Heijne. “Improving the discharge of capacitive granules in a moving bed reactor”. In: *Journal of Environmental Chemical Engineering* 9.4 (2021), p. 105556.
- [40] Alexandra Deeke, Tom H. J. A. Sleutels, Tim F. W. Donkers, Hubertus V. M. Hamelers, Cees J. N. Buisman, and Annemiek Ter Heijne. “Fluidized Capacitive Bioanode As a Novel Reactor Concept for the Microbial Fuel Cell”. In: *Environmental Science & Technology* 49.3 (2015), pp. 1929–1935.
- [41] Monjur Mourshed, Seyed Mohammad Rezaei Niya, Ruchika Ojha, Gary Rosengarten, John Andrews, and Bahman Shabani. “Carbon-based slurry electrodes for energy storage and power supply systems”. In: *Energy Storage Materials* 40 (2021), pp. 461–489.
- [42] Changyong Zhang, Jinxing Ma, Lei Wu, Jingyi Sun, Li Wang, Tianyu Li, and T. David Waite. “Flow Electrode Capacitive Deionization (FCDI): Recent Developments, Environmental Applications, and Future Perspectives”. In: *Environmental Science & Technology* 55.8 (2021), pp. 4243–4267.
- [43] Ko Yeon Choo, Chung Yul Yoo, Moon Hee Han, and Dong Kook Kim. “Electrochemical analysis of slurry electrodes for flow-electrode capacitive deionization”. In: *Journal of Electroanalytical Chemistry* 806 (2017), pp. 50–60.
- [44] Kelsey B. Hatzell, Muhammad Boota, and Yury Gogotsi. “Materials for suspension (semi-solid) electrodes for energy and water technologies”. In: *Chemical Society Reviews* 44.23 (2015), pp. 8664–8687.
- [45] Bilen Akuzum, Pushpendra Singh, Devon A. Eichfeld, Lutfi Agartan, Simge Uzun, Yury Gogotsi, and E. Caglan Kumbur. “Percolation characteristics of conductive additives for capacitive flowable (semi-solid) electrodes”. In: *ACS Applied Materials & Interfaces* 12.5 (2020), pp. 5866–5875.
- [46] Selvaraj Chinnathambi, Mahinder Ramdin, and Thijs J. H. Vlught. “Mass Transport Limitations in Electrochemical Conversion of CO₂ to Formic Acid at High Pressure”. In: *Electrochem* 3.3 (2022), pp. 549–569.
- [47] Marco J. W. Frank, Johannes A. M. Kuipers, and Wim P. M. van Swaaij. “Diffusion Coefficients and Viscosities of CO₂ + H₂O, CO₂ + CH₃OH, NH₃ + H₂O, and NH₃ + CH₃OH Liquid Mixtures”. In: *Journal of Chemical & Engineering Data* 41.2 (1996), pp. 297–302.

- [48] J. W. Haverkort. "A theoretical analysis of the optimal electrode thickness and porosity". In: *Electrochimica Acta* 295 (2019), pp. 846–860.
- [49] M. Souzy, H. Lhuissier, E. Villermaux, and B. Metzger. "Stretching and mixing in sheared particulate suspensions". In: *Journal of Fluid Mechanics* 812 (2017), pp. 611–635.
- [50] Daniel Alfisi, Amit N. Shocron, Robert Gloukhovski, David A. Vermaas, and Matthew E. Suss. "Resistance breakdown of a membraneless hydrogen–bromine redox flow battery". In: *ACS Sustainable Chemistry & Engineering* 10.39 (2022), pp. 12985–12992.
- [51] Giulia Marcandalli, Akansha Goyal, and Marc T. M. Koper. "Electrolyte Effects on the Faradaic Efficiency of CO₂ Reduction to CO on a Gold Electrode". In: *ACS Catalysis* 11.9 (2021), pp. 4936–4945.
- [52] Julie B. Hipp. *Structure, Rheology, and Electrical Conductivity of High-Structured Carbon Black Suspensions*. University of Delaware, 2020.
- [53] Jun Huang and Jianbo Zhang. "Theory of Impedance Response of Porous Electrodes: Simplifications, Inhomogeneities, Non-Stationarities and Applications". In: *Journal of The Electrochemical Society* 163.9 (2016), A1983–A2000.
- [54] Marco S. Alfonso, Hélène Parant, Jinkai Yuan, Wilfrid Neri, Eric Laurichesse, Katerina Kampioti, Annie Colin, and Philippe Poulin. "Highly conductive colloidal carbon based suspension for flow-assisted electrochemical systems". In: *iScience* 24.5 (2021), p. 102456.
- [55] Jonathan W. Campos, Majid Beidaghi, Kelsey B. Hatzell, Christopher R. Dennison, Benjamin Musci, Volker Presser, Emin C. Kumbur, and Yury Gogotsi. "Investigation of carbon materials for use as a flowable electrode in electrochemical flow capacitors". In: *Electrochimica Acta* 98 (2013), pp. 123–130.
- [56] Johannes Lohaus, Deniz Rall, Maximilian Kruse, Viktoria Steinberger, and Matthias Wessling. "On charge percolation in slurry electrodes used in vanadium redox flow batteries". In: *Electrochemistry Communications* 101 (2019), pp. 104–108.
- [57] Chester Miller. "Predicting Non-Newtonian Flow Behavior in Ducts of Unusual Cross Section". In: *Industrial & Engineering Chemistry Fundamentals* 11.4 (1972), pp. 524–528.
- [58] John S. Newman and Charles W. Tobias. "Theoretical Analysis of Current Distribution in Porous Electrodes". In: *Journal of The Electrochemical Society* 109.12 (1962), p. 1183.
- [59] Qing Chen, Michael R. Gerhardt, and Michael J. Aziz. "Dissection of the Voltage Losses of an Acidic Quinone Redox Flow Battery". In: *Journal of The Electrochemical Society* 164.6 (2017), A1126–A1132.
- [60] José Fernando Pérez, Javier Llanos, Cristina Sáez, Conrado López, Pablo Cañizares, and Manuel Andrés Rodrigo. "Towards the scale up of a pressurized-jet microfluidic flow-through reactor for cost-effective electro-generation of H₂O₂". In: *Journal of Cleaner Production* 211 (2019), pp. 1259–1267.

- [61] Lorenz M. Baumgartner, Andrey Goryachev, Christel I. Koopman, David Franzen, Barbara Ellendorff, Thomas Turek, and David A. Vermaas. “Electrowetting limits electrochemical CO₂ reduction in carbon-free gas diffusion electrodes”. In: *Energy Advances* 2.11 (2023), pp. 1893–1904.
- [62] Changyong Zhang, Lei Wu, Jinxing Ma, Min Wang, Jingyi Sun, and T. David Waite. “Evaluation of long-term performance of a continuously operated flow-electrode CDI system for salt removal from brackish waters”. In: *Water Research* 173 (2020), p. 115580.
- [63] Wann Zhang, Wenchao Xue, Chunpeng Zhang, and Kang Xiao. “Towards long-term operation of flow-electrode capacitive deionization (FCDI): Optimization of operating parameters and regeneration of flow-electrode”. In: *Heliyon* 10.2 (2024), e24940.
- [64] S. Porada, D. Weingarth, H. V. M. Hamelers, M. Bryjak, V. Presser, and P. M. Biesheuvel. “Carbon flow electrodes for continuous operation of capacitive deionization and capacitive mixing energy generation”. In: *Journal of Materials Chemistry A* 2.24 (2014), pp. 9313–9321.
- [65] Kevin G. Gallagher, Stephen E. Trask, Christoph Bauer, Thomas Woehrle, Simon F. Lux, Matthias Tschech, Peter Lamp, Bryant J. Polzin, Seungbum Ha, Brandon Long, Qingliu Wu, Wenquan Lu, Dennis W. Dees, and Andrew N. Jansen. “Optimizing Areal Capacities through Understanding the Limitations of Lithium-Ion Electrodes”. In: *Journal of The Electrochemical Society* 163.2 (2016), A138–A149.
- [66] *pH Calculator*. URL: <https://www.aqion.onl/>.
- [67] P. Serp. “7.13 - Carbon”. In: *Comprehensive Inorganic Chemistry II (Second Edition)*. Ed. by Jan Reedijk and Kenneth Poeppelmeier. Amsterdam: Elsevier, 2013, pp. 323–369. ISBN: 978-0-08-096529-1.

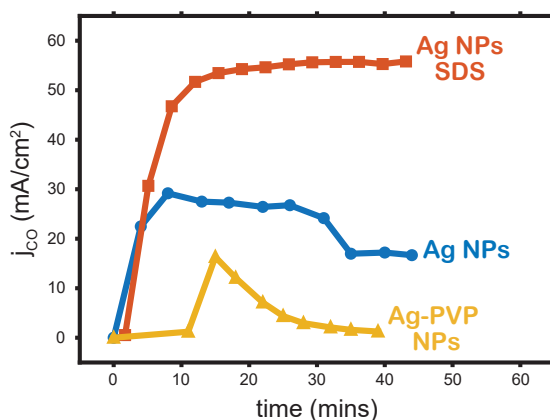
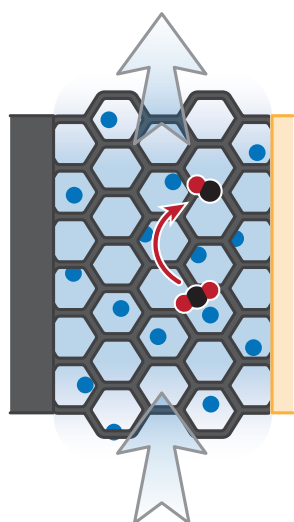
3

FLOW-THROUGH ELECTRODES ENABLE PARTIAL CURRENT DENSITIES BEYOND 50 MA/CM² IN AQUEOUS CO₂ ELECTROLYSIS

Parts of this chapter have been submitted for publication as "*3D current collectors enable partial current densities beyond 50 mA/cm² in aqueous CO₂ electrolysis*" by Nathalie E. G. Ligthart, Mohammed Khan, Johan T. Padding, and David A. Vermaas.

ABSTRACT

Electrochemical conversion of CO_2 to hydrocarbons in aqueous systems is severely limited by the low solubility and slow transport of CO_2 in aqueous systems. We demonstrate that we can reach partial current densities for CO_2 -to- CO over 50 mA/cm^2 in fully aqueous systems. We alleviate the mass transfer limitation by combining a suspension of catalytically active silver nanoparticles (Ag NPs) with a flow-through current collector. This extends the reactive area into the electrolyzer channel and improves the accessibility of dissolved CO_2 in a larger volume of electrolyte. The flow-through electrode system also outperforms a fully suspended electrode (based on carbon black particles), due to enhanced electric conductivity and smaller carbon area to minimize parasitic side-reactions. Additionally, we observe a strong increase in performance upon adding SDS or PVP as surfactant to moderate particle aggregation. The highest CO current density (56 mA/cm^2) was achieved in a flow-through electrode with a suspension of 0.1 wt% Ag NPs and 0.1 wt% SDS, and could be sustained for more than 45 minutes. This shows that the CO current density in aqueous systems can be enhanced considerably by exploiting larger electrolyte volumes via smart electrode designs, such as a flow-through principle.



3.1. INTRODUCTION

The excessive CO₂ levels in our atmosphere are driving a global need to transition to fossil-free renewable energy, fuels, and materials.[1, 2] Electrochemical CO₂ reduction is gaining attention as a clean route to convert CO₂ to basic carbon compounds (*e.g.* CO, ethylene, formic acid), and ultimately to synthetic hydrocarbons such as fuels, plastics, and green chemicals without consuming fossil fuels and releasing new CO₂. [3], [4]

Despite the significant interest in electrochemical CO₂ reduction, the technology is challenging to commercialize. Due to low CO₂ solubility and slow mass transport, the achievable current densities in fully aqueous systems are typically limited to 2 mA/cm², [5] while reaching current densities of at least 200 mA/cm² at high ($\geq 95\%$) Faradaic efficiency (FE) and low cell voltage (≤ 3 V) [6] in scalable systems will be required to achieve economic viability. [7–9] Higher current densities are obtained in gas-fed CO₂ electrolysis configurations that leverage improved mass transfer to achieve these targets at lab scales, but are suffering from complex water management [10–12] and stability issues [13–15] in stacked and larger electrolyzers.

To address these limitations, we studied volume-based aqueous systems, that can alleviate mass transfer limitations through accessing a larger electrolyte volume and making more reactant available, potentially leading to more robust and scalable systems. [16–18] Suspension electrodes, also known as semi-solid or flowable electrodes, enable the electric current to percolate deep into the electrolyzer channel and to reach otherwise inaccessible CO₂ molecules. [19] Although suspension electrodes have proven very effective in various electrochemical applications (*e.g.* semi-solid redox flow batteries [20, 21], flow-electrode capacitive deionization [22, 23], microbial fuel cells [24, 25]), their application in CO₂ electrolysis introduces several challenges. A trade-off between conductivity and flowability results in a poor reaction distribution over the channel depth and creates dead zones where no reaction takes place. Additionally, the relatively large conductive area compared to the catalyst area can lead to increased competition with parasitic reactions, such as HER. [26]

Further expanding the concept of volume-based electrodes, we introduce a flow-through current collector that effectively replaces the flowable conductive network with a static network. Incorporating a solid and continuous structure leads to higher electric conductivity than relying on intermittent particle-particle interactions [27, 28]. Additionally, this strategy decreases the carbon surface area relative to the area active for CO₂ reduction, and thereby minimizes side reactions. [16] Flow-through electrodes have already been applied successfully in other electrochemical applications such as redox flow batteries [29, 30] and water electrolysis [31, 32]. We expect that replacing the carbon particle network in a suspension by a static conductive network can lead to higher geometric current density and selectivity in aqueous CO₂ reduction as well.

Here, we demonstrate volume-based CO₂ reduction with suspensions of silver nanoparticles (Ag NPs) flowing through a 3D (foam) current collector. We compare the flow-through system with a conventional flow-by system and a fully suspension-based system. We reach geometric current densities for CO₂-to-CO conversion that are an order of magnitude higher than for flat electrodes, and show that adding stabilizing agents improves the system further, demonstrating a viable pathway towards intensifying CO₂ reduction in aqueous flow systems.

3.2. METHODS

We performed CO₂ electrolysis in a custom-made flow cell equipped with 6 mm thick flow channels, a Selemion AMV anion exchange membrane, and an Ir-/Ru-oxide coated Ti-sheet (Permascand) as anode (Fig. S3.2). As cathode, we tested a suspension of Ag NPs flowing through a carbon foam (Fig. 3.1b), a suspension of carbon black (CB) and Ag NPs flowing past a glassy carbon plate (Fig. 3.1c), and a silver plate (Fig. 3.1d). A CO₂-saturated 0.5 M KHCO₃ solution was used as catholyte and anolyte and circulated through the setup at 80 mL/min. All suspensions were prepared by mixing and sonicating the electrolyte, particles, and optional surfactants. A constant current was applied (AutoLab and Ivium), and the product gases were analyzed in-line with a CompactGC^{4.0} (Interscience). Details on the experimental methods are supplied in the SI.

3.3. RESULTS AND DISCUSSION

Employing a flow-through current collector with a flowing suspension of catalyst particles yields substantially higher CO current densities compared to the carbon-based suspension and a conventional silver plate electrode (Fig. 3.1). The CO current density of 27 mA/cm² reached in the flow-through system is more than 5 times higher than in the full suspension system (max. 5 mA/cm²), and more than 10 times higher than on the Ag plate (max. 2 mA/cm², equivalent to comparable flow systems in literature).[5] Although both the flow-through and the full-suspension systems benefit from a larger volume with accessible CO₂, shorter distances between the electrode and bulk electrolyte, and interrupted electrode surfaces that disrupt diffusion boundary layers, the flow-through electrode holds additional advantages over the full-suspension system.[16, 26] Firstly, the flow-through electrode provides a permanent conductive network that continuously spans the entire channel depth. This offers higher electrical conductivity than the dynamic networks in a suspension electrode, which leads to improved volume utilization.[16, 27, 28] Secondly, flowing the suspension particles in the full-suspension system lowers the relative velocity between the electrode and electrolyte, which likely diminishes the positive effect of electrolyte flow. As a result, the flow-through configuration makes the best use of the available CO₂ and the electrolyte flow.

Despite the stable performance during catalysis shown in Fig. 3.1, we observe that the Ag NP suspension is not stable. Upon flowing the suspension through the flow-through current collector, the foam acts as a filter and captures most of the suspended Ag NPs within 1 minute of recirculation. This is evident from the fast loss of grey color in the fresh suspension during pumping (Fig. 3.2a-b), and from the large amount of Ag NPs that are visibly stuck to the foam section facing the channel inlet (Fig. 3.3c) and on struts inside the foam (Fig. S3.3 in SI). We hypothesize that severe agglomeration in the first cm of the current collector is preventing the flow-through from performing at its full potential. Based on the color of the electrolyte, the aggregation process happens at a timescale of <1 minute, and therefore occurs before the product gas reaches a stable composition. Hence, the steady state (Ag NPs after 20 minutes in Fig. 2.1a) is reached with a significantly smaller catalytic surface area compared to the initially available area of the suspended Ag NPs. We expect that the performance can be enhanced further by preventing particle aggregation caused by strong Van der Waals forces and weakened

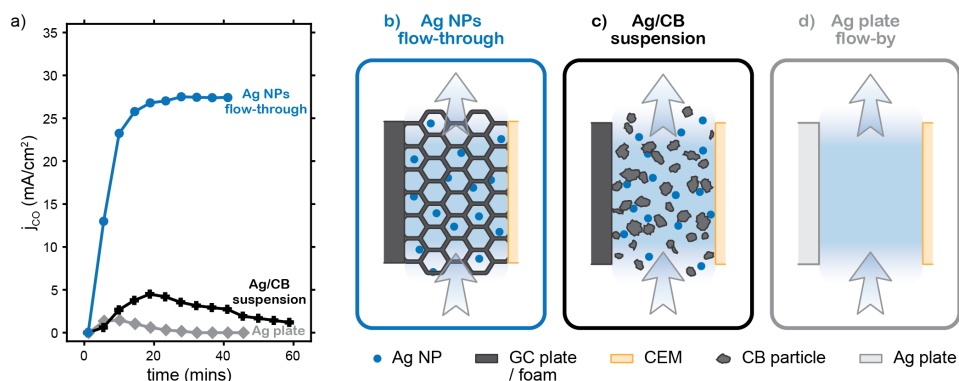


Figure 3.1: The achieved partial CO current density (j_{CO}) over time per flow system. The j_{CO} equilibrates during the first 10 minutes of reaction due to flushing of the headspace in the electrolyte container. The catalytic suspension combined with an inert flow-through electrode (Ag NPs flow-through) reaches higher j_{CO} with greater stability than the flowed suspension of carbon black (CB) microparticles and silver nanoparticles (Ag NP), and the conventional flow-by system with a silver plate (Ag plate) electrode.

electrostatic repulsion in the electrolyte. We can use methods from colloid science, such as adding stabilizing agents, to achieve this.

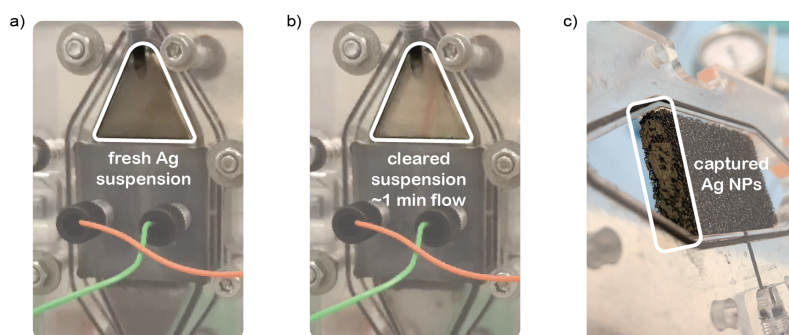


Figure 3.2: Pictures of a) the fresh Ag NP suspension inside the flow channel right after starting the pump, and b) the same suspension that clears within one minute of pumping. c) Picture of a used carbon foam with a large quantity of Ag NPs captured and stuck to the side of the foam facing the channel inlet.

Incorporating surfactants into the reactive suspensions, either by adding sodium dodecyl sulfate (SDS) or using pre-coated polyvinylpyrrolidone (PVP)-capped NPs, indeed raises the CO current density. The SDS- and PVP-stabilized suspensions produce higher CO current densities of 42, and 33 mA/cm², respectively, compared to the bare Ag NP suspension (27 mA/cm²) when applying a total current density of 50 mA/cm² (Fig. 3.3a). Although the initial motive for adding surfactants was to repress particle aggregation, surfactants also aid CO₂ reduction by lowering the surface tension and thereby facilitating bubble removal at smaller bubble sizes.[33] This can enhance bubble-induced mass transfer[34], preventing blocking of pores and active sites by large bubbles.

In addition, surfactants can lend improved CO selectivity by protecting the NP sur-

face from undergoing degradation and morphological changes at highly negative potentials.[35] The bare Ag suspension shows a decline in performance during the run at 100 mA/cm², which occurs even faster and more drastically when PVP-capped Ag NPs are used. The peak observed when applying 100 mA/cm² to the PVP-capped suspension is likely related to the large potential stripping PVP off the NP surfaces, initially increasing the availability of active sites and performance, and subsequently degrading the NP surfaces, decreasing the performance.[35] In contrast, the SDS-stabilized suspensions produce a stable CO current density of 56 mA/cm² when 100 mA/cm² are applied, and even withstand 150 mA/cm² of applied current density (Fig. S3.4 in SI), although the achieved CO current density is decreased compared to Fig. 3.3b. Experiment repetitions revealed some decline for repeated experiments with the same SDS-based solution (Fig. S3.5 in SI).

In more detail, SDS is especially interesting as its addition does not prevent the sticking behavior completely, but rather causes a cloud of Ag NPs to release upon applying a negative potential (Fig. S3.6 in SI). As an anionic surfactant, SDS evidently has a higher repulsion to the negative electrode than the neutral PVP molecules and possibly leads to poor charge transfer between the electrode and Ag NPs at higher negative potentials, causing a decline in CO current density at an applied current density of >100 mA/cm².

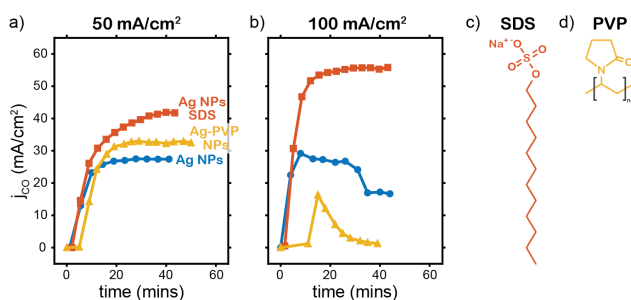


Figure 3.3: The achieved CO current densities (j_{CO}) on Ag NP suspensions without surfactant, PVP-coated Ag NPs, and suspensions of Ag NPs with 0.1 wt.% of SDS added to the electrolyte, when applying a) 50 mA/cm² and b) 100 mA/cm².

Work by Liu et al.[35] indicates that steric hindrance by surfactants can improve particle stability but also hinder CO₂ transfer to the catalytic surface and block active sites. Therefore, we anticipate an optimum in the surfactant-to-particle ratio that lends sufficient stability while preventing the Ag NP surfaces to become too crowded for CO₂ molecules to reach it. Varying the Ag:SDS ratio between 0.1:0 and 0.1:1 (wt%) reveals that the best performance is obtained when both loadings are equal at 0.1 wt% (Fig. 3.4a). This results in a concentration of 3.5 mM SDS, which is well above the critical micelle concentration (CMC) of SDS in 0.5 M KHCO₃. [36] Varying the absolute Ag/SDS concentrations while keeping this ratio fixed at 1 shows that the CO current density is not increased further when raising both concentrations above 0.1 wt% (Fig. 3.4b). The CO current density even decreases when using a higher concentration of 0.5 wt% and applying 50 or 100 mA/cm², while it increases when applying 200 mA/cm². We could speculate that higher potentials provide more repulsion and stability when the particle

suspension is more crowded. However, this effect could also be due to the order in which the current densities were applied; more experiments at varying (and higher) concentrations should be performed to optimize the Ag NP and SDS concentrations further.

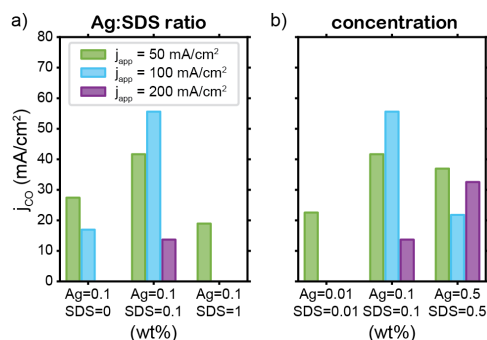


Figure 3.4: Resulting CO current density a) at various Ag:SDS ratio's where the Ag concentration is kept constant at 0.1 wt%, and b) at various Ag and SDS concentrations where the Ag:SDS ratio is fixed at 1. The cases with Ag/SDS equal to 0.1/0, 0.1/1, and 0.01/0.01 were not performed at every current density.

In addition, we tested a silver-coated CB suspension with a flow-through electrode, an Ag NP suspension containing both PVP and SDS, and an Ag NPs +SDS suspension with a flow-through electrode with larger pores (8 pores/cm). None of these performed better than the SDS-stabilized Ag suspensions in combination with the flow-through electrode with standard pore size (24 pores/cm); see Fig. 3.5. The drastically lower CO current density in the flow-through electrode with larger pores emphasizes the need for microporous electrodes to ensure sufficient Ag particle-electrode interactions.

Interestingly, we observed better performance when circulating the suspension for a while before applying the potential, compared to applying a current immediately upon filling the flow cell (Fig. S3.7 in SI). This suggests that having some Ag particles attached to the flow-through electrode promotes CO₂ reduction. In this case, the surfactants can improve the spatial distribution and size of Ag deposits.

3.4. IMPLICATIONS AND CONCLUSIONS

Our results show that a flow-through electrode in combination with surfactants, especially SDS, can significantly improve the CO current density. The highest CO current density of 56 mA/cm² in this study was achieved with an SDS-stabilized Ag NP suspension. We suspect that the surfactants allow 1) a more even coating of Ag NPs to form with fewer aggregates and thus more catalytically active surface area, and 2) improve removal of smaller bubbles which enhances bubble-induced mass transfer and prevents large bubbles from blocking pores and active sites.

With the calculated residence time, this CO current density consumed only 0.6% of the available CO₂ in the channel. Therefore, either the channel can be made longer to raise the portion of utilized CO₂, or the CO current density can be boosted even further (almost 170x, in theory) by bringing the electrode even closer to the dissolved CO₂. This would require a structure with smaller pores, which should ideally be smaller than the

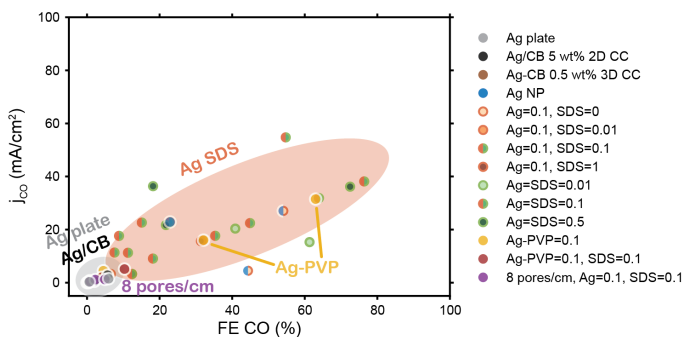


Figure 3.5: Overview of the performance of evaluated systems. The systems containing 2D current collectors (CCs) and/or carbon black (CB) particles perform significantly worse than those employing 3D electrodes and Ag suspensions, *e.g.* Ag SDS, Ag-PVP, and Ag NPs. The Ag-PVP suspension performs similarly as the Ag suspension with SDS, but lacks in stability at higher current densities.

diffusion boundary layer (DBL, estimated to be approximately 10 μm for this foam structure[16]) that forms around the struts where the reaction is taking place. With such intensification, the use of a bipolar membrane could be useful to mitigate OH^- accumulation, which would merge the concept of surfactant-assisted suspensions in flow-through electrodes with the route of bipolar membrane-based bicarbonate conversion.[37–40]

Ultimately, we have shown that a smart electrode design can enhance the CO current density in aqueous electrolyzers considerably, offering an alternative to gas-fed systems as a pathway towards intensifying CO_2 electrolysis.

3.5. SUPPORTING INFORMATION

The relevant data is available in the Zenodo repository at [10.5281/zenodo.12750737](https://zenodo.org/doi/10.5281/zenodo.12750737).

3.5.1 EXPERIMENTAL

All experiments were performed in a custom-made PMMA flow cell with 6 mm thick flow channels. One half of the flow cell consists of a flow channel stacked onto an endplate and is shown in Fig. S3.1. A glassy carbon plate (Goodfellow) is embedded in the cathode endplate in the flow-by configuration (Fig. S3.1a). The flow-through configuration has a glassy carbon foam (RVC foam, 24 pores/cm, approx. 430 μm pore size, Goodfellow) inserted in the flow channel on top of the glassy carbon plate (Fig. S3.1b). A foam that was slightly thicker than the flow channel (6.35 mm versus 6 mm channel thickness) was chosen to ensure a good electrical connection between the glassy carbon foam and the plate. An RVC foam with fewer, larger pores was used in one experiment (8 pores/cm, 1000 μm pore size, 5 mm thick, Nano Chemazone) with three 0.5 mm thick gaskets stacked on top of it (on the side of the membrane) to press the foam tightly against the glassy carbon plate. The glassy carbon plate was cleaned before each experiment by polishing and subsequent sonication in deionized (DI) water. A new piece of RVC foam was used for most experiments and cleaned by sonicating and rinsing in DI water, after which the foam was dried in an oven at 150 $^{\circ}\text{C}$.

The cell was assembled as shown schematically in Fig. S3.2a with a Selemion AMV (100 μm , AGC Engineering) membrane separating the catholyte and anolyte compartments. The membrane was soaked and stored in electrolyte before use. A Ti sheet with Ir-/Ru-oxide coating (Permascand) was used as anode, and a leak-free Ag/AgCl reference electrode (LF-1-45, Alvatek) was inserted into the anode compartment as reference in most experiments, and into a small hole in the RVC in later experiments. The flow cell was connected to the electrolysis setup as shown in Fig. S3.2b.

An electrolyte of 0.5 M KHCO_3 (99%, ThermoFisher Scientific) in deionized water was used for the catholyte and anolyte (both with a volume of 40 mL) in most experiment, one experiment was performed with 0.1 M KHCO_3 . The catholyte suspensions were prepared by adding the desired type and amount of particles to the electrolyte and stirring for 10 minutes, followed by 15 minutes of sonication. When SDS was used, the particles were added to the electrolyte, the suspension was stirred for 5 minutes and sonicated for 10 minutes before adding the required amount of SDS, followed by stirring and sonication for an additional 5 and 15 minutes, respectively. A variety of particle types were used as suspensions, these included silver nanoparticles (Ag NPs, 99.9%, ThermoFisher), carbon black (CB, Vulcan XC-72, Fuel Cell Store), Ag-coated CB (Ag-CB, 20 wt% silver on Vulcan XC-72, Fuel Cell Store), and Ag NPs capped by polyvinylpyrrolidone (Ag-PVP, 99.5%, Merck). The types of particles, current collectors, and electrode configuration used in the different experiment types are listed in Table S3.1.

The anolyte and catholyte were saturated with CO_2 by sparging 50 mL/min of CO_2 , controlled by mass flow controllers (MFCs, Bronkhorst), for at least 30 minutes before each measurement. This was continued during the experiment to keep the electrolytes saturated and to flush the product gases to an inline gas chromatograph (CompactGC4.0, Interscience) for analysis. The electrolytes were circulated at a flow rate of 80 mL/min (L/S Precision Pump System, Masterflex) and a needle valve in the anolyte tubing was used to minimize the pressure difference between the two compartments and prevent membrane rupture. All electrochemical measurements were performed with an IviumStat.h ($\pm 5\text{A}/\pm 10\text{V}$, Ivium), a XP20 ($\pm 20\text{A}/\pm 20\text{V}$, Ivium), or a PGSTAT302N ($\pm 2\text{A}/\pm 30\text{V}$, Autolab) potentiostat. Chronopotentiometry (CP) was performed at various geometrical current densities for 45 minutes each, during which the product gases were analyzed at time intervals of approximately 4 minutes. A CP at 50 mA/cm^2 was always performed first, followed by CPs at 25-200 mA/cm^2 in a randomized order, and a second 50 mA/cm^2 at the end of the day for

comparison. The electrolytes were resaturated with CO₂ for 30 minutes between each CP.

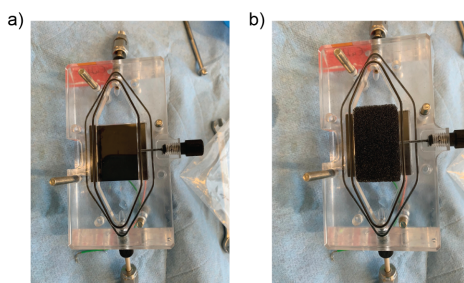


Figure S3.1: Endplates of the flow cell in the a) flow-by and b) flow-through configurations with one flow channel on top. Both configurations have a glassy carbon plate current collector. An RVC foam is inserted into the channel to create the flow-through configuration.

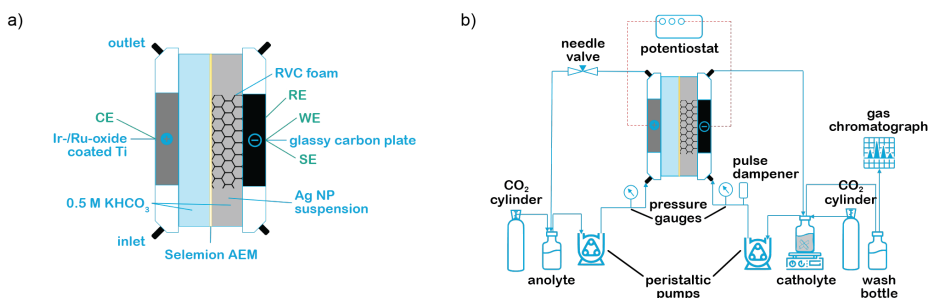


Figure S3.2: a) Schematic of the assembled flow cell (side view) in flow-through configuration with 0.5 M KHCO₃ anolyte flowing on the left side of the anion exchange membrane (AEM), and the silver nanoparticle (Ag NP) suspension in 0.5 M KHCO₃ as catholyte on the right side of the membrane. b) Setup diagram showing all equipment, and liquid and gas flows.

Table S3.1: Used flow configuration, current collectors, particles, surfactant, and electrolyte concentration per experiment type.

Experiment type	Configuration	Plate CC	Foam CC	Particles	Surfactant	KHCO ₃ (M)
Ag plate	flow-by	silver	-	-	-	0.5
Ag CB	flow-by	glassy carbon	-	Ag and CB	-	0.5
Ag-CB	flow-through	glassy carbon	RVC, 24 ppcm	Ag-coated CB	-	0.5
Ag NP	flow-through	glassy carbon	RVC, 24 ppcm	Ag	-	0.5
Ag SDS	flow-through	glassy carbon	RVC, 24 ppcm	Ag	SDS	0.5
Ag-PVP	flow-through	glassy carbon	RVC, 24 ppcm	PVP-capped Ag	PVP	0.5
Ag-PVP SDS	flow-through	glassy carbon	RVC, 24 ppcm	PVP-capped Ag	PVP; SDS	0.5
8 ppcm SDS	flow-through	glassy carbon	RVC, 8 ppcm	Ag	SDS	0.5

3.6. PARTICLE AGGREGATION IN FOAM

Significant aggregation and sticking of particles in the RVC foam was observed in all experiments. The Ag NPs filling and blocking pores can be observed by eye in Fig. S3.3a. An aggregate on a strut inside the foam is shown in the scanning electron microscopy (SEM, JSM-6010LA, JEOL) image in Fig. S3.3b.

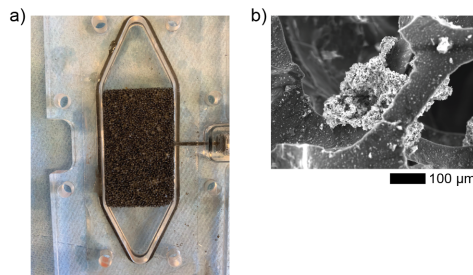


Figure S3.3: a) Photo of a used RVC foam with clearly visible Ag NP aggregates trapped in the pores. b) SEM image of Ag NP aggregates stuck on struts inside the RVC foam.

3.7. SYSTEM COMPARISON

The partial CO current densities achieved over time in various tested systems are shown below (Fig. S3.4). The flow-through systems with silver suspensions reach the highest CO current densities and with the highest stability. This is improved further by including surfactants, PVP or SDS, to the system. The suspensions with SDS as surfactant yield stable performance at higher applied current densities than the PVP-capped suspension particles.

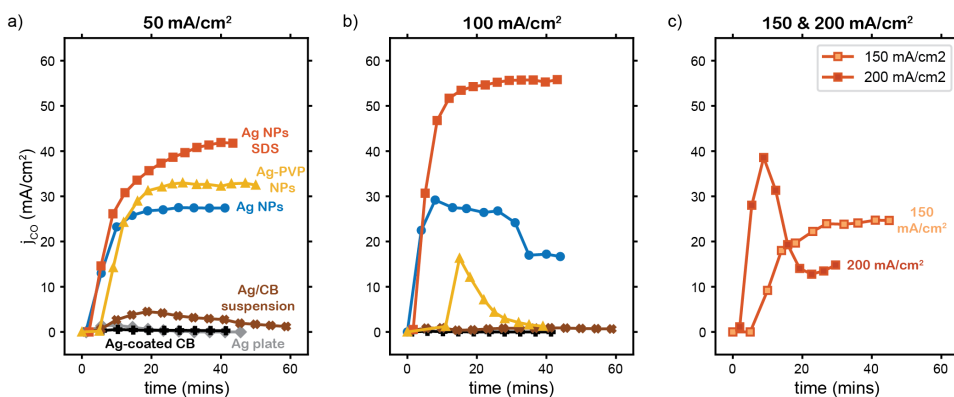


Figure S3.4: CO current density (j_{CO}) over time in the various tested systems at a) 50, b) 100, and c) 150 and 200 mA/cm² applied current density.

3.8. SAMPLE-TO-SAMPLE VARIATION

Although the CO current density was stable during the experiments, it varied between repetitions with identical suspension compositions. Fig. S3.5 shows the j_{CO} over time during the first CP at

50 mA/cm² applied current densities of five experiments performed with 0.1 wt% Ag NPs and 0.1 wt% SDS in 0.5 M KHCO₃, in the order EX013, EX021, EX022, EX027, EX030. This results in a range of achieved j_{CO} values. It is notable that a new AEM was used during EX030 compared to EX027 and is paired with a significant improvement in j_{CO} .

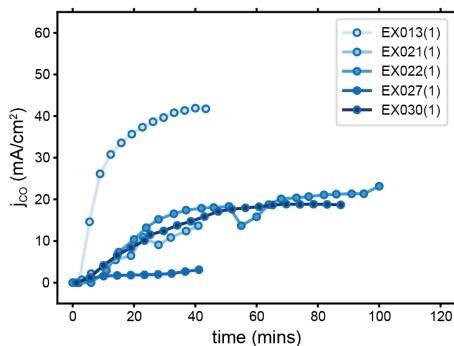


Figure S3.5: CO current density (j_{CO}) over time during multiple experiments with 0.1 wt% Ag NPs and SDS, performed in the order EX013, EX021, EX022, EX027, EX030. The j_{CO} is stable during the individual experiments, but varies per day. A newer membrane was used in EX030 compared to EX027.

3.9. ELECTROSTATIC REPULSION BETWEEN SDS AND CATHODE

SDS was observed not to prevent the suspension particles from sticking inside the flow-through electrode completely, but rather to cause (many of) the captured Ag NPs to be released from the foam electrode upon starting the experiment and applying a negative potential (Fig. S3.6).

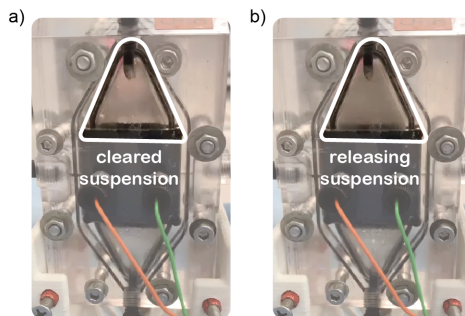


Figure S3.6: Observed Ag NP release in SDS-stabilized suspensions upon applying a negative potential. a) The suspension clears during pumping due to Ag NP capture by the flow-through electrode, and b) a cloud of Ag NPs releases once the CP is started.

3.10. CONTRIBUTIONS OF CAPTURED AND FLOWING AG NPs

Two types of experiments in presence of SDS were performed to assess whether the CO₂ reduction is mostly performed by Ag NPs in suspension or stuck to the foam. During the flow saturation

experiments, the catholyte was sparged with CO_2 for 30 minutes while pumping the catholyte through the setup without applying a potential. This way, the suspension particles were given the opportunity to get stuck inside the flow-through electrode before the repulsion between the cathode and SDS molecules was initiated. During the container saturation experiments, the catholyte was kept in the catholyte container during the 30 minutes of sparging and the catholyte was only pumped into the setup once the potential was applied. Therefore, the suspension was only circulated through the flow cell while the repulsion between the SDS molecules and cathode was active to prevent the Ag NPs from getting stuck in the first place.

Although a visible amount of Ag NPs release and escape from the flow-through electrode upon starting the potential after flow saturation, the achieved CO current density is always higher after flow saturation than after saturating within the container (Fig. S3.7). This shows that particle sticking inside the foam electrode is beneficial for the catalytic performance, and suggests that the captured Ag NPs are more active for CO_2 reduction than the particles that stay in suspension because they are in permanent contact with the current source.

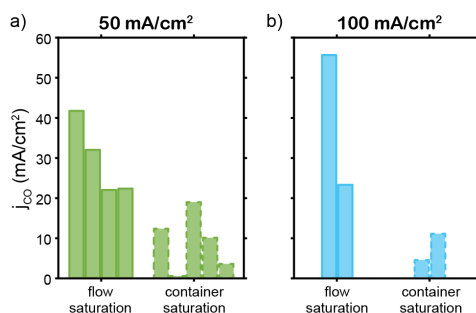


Figure S3.7: Stable j_{CO} during CO_2 reduction at applied current densities of a) 50 mA/cm² and b) 100 mA/cm² after flow- and container saturation.

REFERENCES

- [1] Phil De Luna, Christopher Hahn, Drew Higgins, Shaffiq A. Jaffer, Thomas F Jaramillo, and Edward H. Sargent. “What would it take for renewably powered electrosynthesis to displace petrochemical processes?” In: *Science* 364.6438 (2019), eaav3506.
- [2] Geoffrey Hammond and Marcus Newborough. “Glasgow climate pact: a step on the way towards a lower carbon dioxide world”. In: *Proceedings of the Institution of Civil Engineers - Civil Engineering* 175.1 (2022), pp. 8–8.
- [3] Paolo Gabrielli, Matteo Gazzani, and Marco Mazzotti. “The Role of Carbon Capture and Utilization, Carbon Capture and Storage, and Biomass to Enable a Net-Zero-CO₂ Emissions Chemical Industry”. In: *Industrial & Engineering Chemistry Research* 59.15 (2020), pp. 7033–7045.
- [4] Matthew Jouny, Wesley Luc, and Feng Jiao. “General Techno-Economic Analysis of CO₂ Electrolysis Systems”. In: *Industrial & Engineering Chemistry Research* 57.6 (2018), pp. 2165–2177.
- [5] Lorenz M. Baumgartner, Aron Kahn, Maxime Hoogland, Jorrit Bleeker, Wolter F. Jager, and David A. Vermaas. “Direct imaging of local pH reveals bubble-induced mixing in a CO₂ electrolyzer”. In: *ACS Sustainable Chemistry & Engineering* 11.28 (2023), pp. 10430–10440.
- [6] Danielle Salvatore and Curtis P. Berlinguette. “Voltage Matters When Reducing CO₂ in an Electrochemical Flow Cell”. In: *ACS Energy Letters* 5.1 (2020), pp. 215–220.
- [7] Md Golam Kibria, Jonathan P. Edwards, Christine M. Gabardo, Cao-Thang Dinh, Ali Seifitokaldani, David Sinton, and Edward H. Sargent. “Electrochemical CO₂ Reduction into Chemical Feedstocks: From Mechanistic Electrocatalysis Models to System Design”. In: *Advanced Materials* 31.31 (2019), p. 1807166.
- [8] Richard I. Masel, Zengcai Liu, Hongzhou Yang, Jerry J. Kaczur, Daniel Carrillo, Shaoxuan Ren, Danielle Salvatore, and Curtis P. Berlinguette. “An industrial perspective on catalysts for low-temperature CO₂ electrolysis”. In: *Nature Nanotechnology* 16.2 (2021), pp. 118–128.
- [9] Sumit Verma, Byoungsu Kim, Huei-Ru “Molly” Jhong, Sichao Ma, and Paul J. A. Kenis. “A Gross-Margin Model for Defining Technoeconomic Benchmarks in the Electroreduction of CO₂”. In: *ChemSusChem* 9.15 (2016), pp. 1972–1979.
- [10] Lorenz M. Baumgartner, Christel I. Koopman, Antoni Forner-Cuenca, and David A. Vermaas. “Narrow pressure stability window of gas diffusion electrodes limits the scale-up of CO₂ electrolyzers”. In: *ACS Sustainable Chemistry & Engineering* 10.14 (2022), pp. 4683–4693.
- [11] Bert De Mot, Mahinder Ramdin, Jonas Hereijgers, Thijs J. H. Vlugt, and Tom Breugelmans. “Direct Water Injection in Catholyte-Free Zero-Gap Carbon Dioxide Electrolyzers”. In: *ChemElectroChem* 7.18 (2020), pp. 3839–3843.

- [12] Kostadin V. Petrov, Justin C. Bui, Lorenz Baumgartner, Lien-Chun Weng, Sarah M. Dischinger, David M. Larson, Daniel J. Miller, Adam Z. Weber, and David A. Vermaas. “Anion-exchange membranes with internal microchannels for water control in CO₂ electrolysis”. In: *Sustainable Energy & Fuels* 6.22 (2022), pp. 5077–5088.
- [13] Emiliana R. Cofell, Uzoma O. Nwabara, Saket S. Bhargava, Danielle E. Henckel, and Paul J. A. Kenis. “Investigation of Electrolyte-Dependent Carbonate Formation on Gas Diffusion Electrodes for CO₂ Electrolysis”. In: *ACS Applied Materials & Interfaces* 13.13 (2021), pp. 15132–15142.
- [14] Hesamoddin Rabiee, Lei Ge, Xueqin Zhang, Shihu Hu, Mengran Li, and Zhiguo Yuan. “Gas diffusion electrodes (GDEs) for electrochemical reduction of carbon dioxide, carbon monoxide, and dinitrogen to value-added products: a review”. In: *Energy & Environmental Science* 14.4 (2021), pp. 1959–2008.
- [15] Kailun Yang, Recep Kas, Wilson A. Smith, and Thomas Burdyny. “Role of the Carbon-Based Gas Diffusion Layer on Flooding in a Gas Diffusion Electrode Cell for Electrochemical CO₂ Reduction”. In: *ACS Energy Letters* 6.1 (2021), pp. 33–40.
- [16] Nathalie E. G. Ligthart, Phebe H. van Langevelde, Johan T. Padding, Dennis G. H. Hetterscheid, and David A. Vermaas. “20-Fold Increased Limiting Currents in Oxygen Reduction with Cu-tmpa by Replacing Flow-By with Flow-Through Electrodes”. In: *ACS Sustainable Chemistry & Engineering* 12.34 (2024), pp. 12909–12918.
- [17] Veda Sri Vedharathinam, Zhen Qi, Corie Horwood, Bill Bourcier, Michael Stadermann, Juergen Biener, and Monika Biener. “Using a 3D Porous Flow-Through Electrode Geometry for High-Rate Electrochemical Reduction of CO₂ to CO in Ionic Liquid”. In: *ACS Catalysis* 9.12 (2019), pp. 10605–10611.
- [18] F. C. Walsh, L. F. Arenas, C. Ponce de León, G. W. Reade, I. Whyte, and B. G. Mellor. “The continued development of reticulated vitreous carbon as a versatile electrode material: Structure, properties and applications”. In: *Electrochimica Acta* 215 (2016), pp. 566–591.
- [19] Alexandra Rommerskirchen, Anna Kalde, Christian J. Linnartz, Leon Bongers, Georg Linz, and Matthias Wessling. “Unraveling charge transport in carbon flow-electrodes: Performance prediction for desalination applications”. In: *Carbon* 145 (2019), pp. 507–520.
- [20] Nicholas J. Matteucci, Christopher T. Mallia, Bertrand J. Neyhouse, Madhu V. Majji, and Fikile R. Brushett. “Toward electrochemical design principles of redox-mediated flow batteries”. In: *Current Opinion in Electrochemistry* 42 (2023), p. 101380.
- [21] Francesca Soavi, Alessandro Brilloni, Francesca De Giorgio, and Federico Poli. “Semi-solid lithium/oxygen flow battery: an emerging, high-energy technology”. In: *Current Opinion in Chemical Engineering* 37 (2022), p. 100835.
- [22] Jie Ma, Chunxiao Zhai, and Fei Yu. “Review of flow electrode capacitive deionization technology: Research progress and future challenges”. In: *Desalination* 564 (2023), p. 116701.

- [23] Wannu Zhang, Wenchao Xue, Kang Xiao, Chettiyappan Visvanathan, Jialing Tang, and Lu Li. "Selection and optimization of carbon-based electrode materials for flow-electrode capacitive deionization". In: *Separation and Purification Technology* 315 (2023), p. 123649.
- [24] C. Borsje, T. Sleutels, W. Zhang, W. Feng, C. J. N. Buisman, and A. ter Heijne. "Making the best use of capacitive current: Comparison between fixed and moving granular bioanodes". In: *Journal of Power Sources* 489 (2021), p. 229453.
- [25] Alexandra Deeke, Tom H. J. A. Sleutels, Tim F. W. Donkers, Hubertus V. M. Hamelers, Cees J. N. Buisman, and Annemiek Ter Heijne. "Fluidized Capacitive Bioanode As a Novel Reactor Concept for the Microbial Fuel Cell". In: *Environmental Science & Technology* 49.3 (2015), pp. 1929–1935.
- [26] Nathalie E. G. Lighthart, Gerard Prats Vergel, Johan T. Padding, and David A. Vermaas. "Practical potential of suspension electrodes for enhanced limiting currents in electrochemical CO₂ reduction". In: *Energy Advances* 3.4 (2024), pp. 841–853.
- [27] Hongning Chen, Yao Liu, Xuefeng Zhang, Quan Lan, Yue Chu, Yongliang Li, and Qixing Wu. "Single-component slurry based lithium-ion flow battery with 3D current collectors". In: *Journal of Power Sources* 485 (2021), p. 229319.
- [28] Xinyuan Zhang, Hongjian Zhou, Zhen He, Haimin Zhang, and Huijun Zhao. "Flow-electrode capacitive deionization utilizing three-dimensional foam current collector for real seawater desalination". In: *Water Research* 220 (2022), p. 118642.
- [29] Nuno M. Delgado, Carlos M. Almeida, Ricardo Monteiro, and Adélio Mendes. "Flow-Through Design for Enhanced Redox Flow Battery Performance". In: *Journal of The Electrochemical Society* 169.2 (2022), p. 020532.
- [30] M. E. Suss, K. Conforti, L. Gilson, C. R. Buie, and M. Z. Bazant. "Membraneless flow battery leveraging flow-through heterogeneous porous media for improved power density and reduced crossover". In: *RSC Advances* 6.102 (2016), pp. 100209–100213.
- [31] H. Rajaei, A. Rajora, and J. W. Haverkort. "Design of membraneless gas-evolving flow-through porous electrodes". In: *Journal of Power Sources* 491 (2021), p. 229364.
- [32] Feichen Yang, Myung Jun Kim, Micah Brown, and Benjamin J. Wiley. "Alkaline Water Electrolysis at 25 A cm⁻² with a Microfibrous Flow-through Electrode". In: *Advanced Energy Materials* 10.25 (2020), p. 2001174.
- [33] Nirbhay Kumar, Md Qaisar Raza, and Rishi Raj. "Surfactant aided bubble departure during pool boiling". In: *International Journal of Thermal Sciences* 131 (2018), pp. 105–113.
- [34] Thomas Burdyny, Percival J. Graham, Yuanjie Pang, Cao-Thang Dinh, Min Liu, Edward H. Sargent, and David Sinton. "Nanomorphology-Enhanced Gas-Evolution Intensifies CO₂ Reduction Electrochemistry". In: *ACS Sustainable Chemistry & Engineering* 5.5 (2017), pp. 4031–4040.

- [35] Menglong Liu, Ying Kong, Huifang Hu, Noémi Kovács, Changzhe Sun, Iván Zecualtecatl Montiel, María de Jesús Gálvez Vázquez, Yuhui Hou, Marta Mirolo, Isaac Martens, Jakub Drnec, Soma Vesztergom, and Peter Broekmann. “The capping agent is the key: Structural alterations of Ag NPs during CO₂ electrolysis probed in a zero-gap gas-flow configuration”. In: *Journal of Catalysis* 404 (2021), pp. 371–382.
- [36] E. Dutkiewicz and A. Jakubowska. “Effect of electrolytes on the physicochemical behaviour of sodium dodecyl sulphate micelles”. In: *Colloid and Polymer Science* 280.11 (2002), pp. 1009–1014.
- [37] Tengfei Li, Eric W. Lees, Zishuai Zhang, and Curtis P. Berlinguette. “Conversion of Bicarbonate to Formate in an Electrochemical Flow Reactor”. In: *ACS Energy Letters* 5.8 (2020), pp. 2624–2630.
- [38] Hakhyeon Song, Carlos A. Fernández, Hyeonuk Choi, Po-Wei Huang, Jihun Oh, and Marta C. Hatzell. “Integrated carbon capture and CO production from bicarbonates through bipolar membrane electrolysis”. In: *Energy & Environmental Science* 17.10 (2024), pp. 3570–3579.
- [39] Hakhyeon Song, Carlos A. Fernández, Anush Venkataraman, Victor D. Brandão, Sandeep S. Dhingra, Sukaran S. Arora, Saket S. Bhargava, Carlos M. Villa, Carsten Sievers, Sankar Nair, and Marta C. Hatzell. “Ethylene Production from Carbonate Using a Bipolar Membrane Electrolysis System”. In: *ACS Applied Energy Materials* 7.3 (2024), pp. 1224–1233.
- [40] Alex J. Welch, Emily Dunn, Joseph S. DuChene, and Harry A. Atwater. “Bicarbonate or Carbonate Processes for Coupling Carbon Dioxide Capture and Electrochemical Conversion”. In: *ACS Energy Letters* 5.3 (2020), pp. 940–945.

4

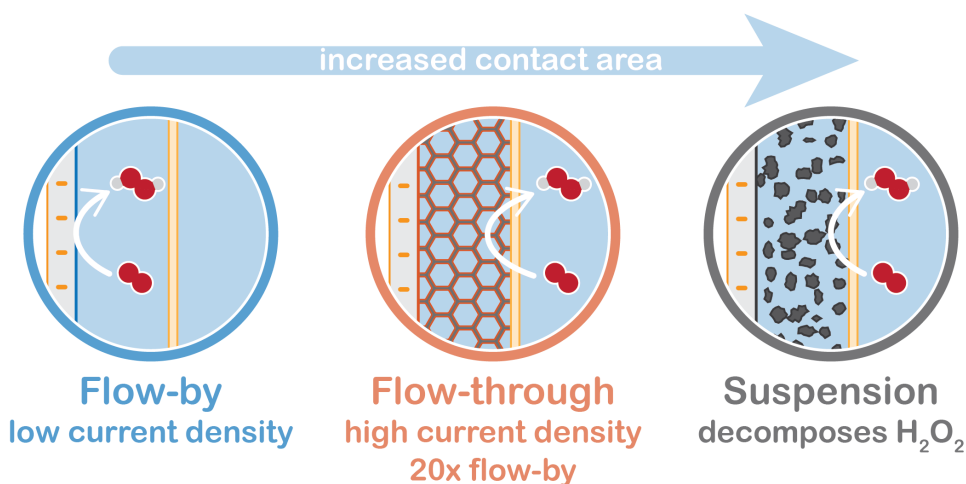
TWENTYFOLD INCREASED LIMITING CURRENTS IN OXYGEN REDUCTION WITH CU-TMPA BY REPLACING FLOW-BY WITH FLOW-THROUGH ELECTRODES

Parts of this chapter have been published as "20-Fold increased limiting currents in oxygen reduction with Cu-tmpa by replacing flow-by with flow-through electrodes" by Nathalie E. G. Ligthart, Phebe H. van Langevelde, Johan T. Padding, Dennis G. H. Hetterscheid, and David A. Vermaas in *ACS Sustainable Chemistry & Engineering*, 2024, **12**, 12909-12918.

ABSTRACT

Electrochemical oxygen reduction is a promising, sustainable alternative to the current industrial production method for hydrogen peroxide (H_2O_2), which is a green oxidant in many (emerging) applications in the chemical industry, water treatment, and fuel cells. Low solubility of O_2 in water causes severe mass transfer limitations and loss of H_2O_2 selectivity at industrially-relevant current densities, complicating the development of practical scale electrochemical H_2O_2 synthesis systems. We tested a flow-by and flow-through configuration, and suspension electrodes in an electrochemical flow cell to investigate the influence of electrode configuration and flow conditions on mass transfer and H_2O_2 production. We monitored the H_2O_2 production using Cu-tmpa (tmpa = tris(2-pyridylmethyl)amine) as a homogeneous copper-based catalyst in a pH-neutral phosphate buffer during 1 hour of catalysis and estimated the limiting current density from CV scans. We achieve the highest H_2O_2 production and a 15-20 times higher geometrical limiting current density in the flow-through compared to the flow-by configuration, due to the increased surface area and foam structure that improved mass transfer. The activated carbon (AC) material in suspension electrodes, that have an even larger surface area, decompose all produced H_2O_2 and prove unsuitable for H_2O_2 synthesis. Although the mass transfer limitations seem to be alleviated on the microscale in the flow-through system, the high O_2 consumption and H_2O_2 production cause challenges in maintaining the initially reached current density and Faradaic efficiency (FE). The decreasing ratio between the O_2 and H_2O_2 concentrations in the bulk electrolyte will likely pose a challenge when proceeding to larger systems with longer electrodes. Tuning the reactor design and operating conditions will be essential in maximizing the FE and current density.

4



4.1. INTRODUCTION

Hydrogen peroxide (H_2O_2) is an important chemical that is widely used in established methods for chemical synthesis[1], disinfection[2], and bleaching[3], as well as applications such as advanced oxidation processes in water treatment[4], and fuel cells[5]. Contrary to the use of H_2O_2 as a green oxidant, its anthraquinone production process is energy-intensive and environmentally unfriendly.[6] The continued and increasing demand[7] for H_2O_2 as a green oxidant has provoked the development of alternative production methods, such as electrochemical 2e^- oxygen (O_2) reduction.

The oxygen reduction reaction (ORR) can run on renewable energy, water, and oxygen as inputs and provides a sustainable route for H_2O_2 synthesis[8], but suffers from challenges imposed by the low solubility of O_2 in water (1.1 mM when in contact with pure O_2 gas at standard conditions). The small amount of O_2 available near the electrode depletes rapidly when working at higher current densities. This causes severe mass transfer limitations and lowers catalyst selectivity considerably at economically viable current densities.[9, 10] Electrochemical H_2O_2 synthesis has been commercialized in the Dow-Huron process[11] that produces highly alkaline H_2O_2 solutions, of which the pH is lowered after production to prevent H_2O_2 decomposition and to fit the requirement for acidic or neutral H_2O_2 solutions of many applications. Commercially applicable processes for producing neutral and acidic H_2O_2 solutions directly are still lacking.[12] Improved reactor designs are necessary to alleviate mass transfer limitations and advance towards widely applicable practical-scale electrochemical H_2O_2 synthesis devices.[5]

Here, we perform ORR in an electrochemical flow cell with three different electrode configurations and Cu-tmpa (tmpa = tris(2-pyridylmethyl)amine) as catalyst. This catalyst was selected because it is the fastest copper-based molecular ORR catalyst reported to date, catalyzing the reduction of oxygen with more than 2 million turnovers per second.[13] Furthermore, electrochemical experiments have shown that this Cu-based molecular catalyst converts O_2 in neutral pH in two consecutive steps, starting with fast 2-electron reduction of O_2 to H_2O_2 , followed by a slower second 2-electron reduction of H_2O_2 to H_2O , therefore generating H_2O_2 as a stable intermediate.[13, 14] It has been shown that in a rotating disk electrode (RDE) setup, the ORR selectivity is determined by the local O_2 and H_2O_2 concentrations at the electrode surface, and thus highly dependent on transport of O_2 towards- and H_2O_2 away from the electrode.[15] Cu-tmpa was shown to generate H_2O_2 solutions with high Faradaic efficiency for up to 8 hours. However, an RDE setup is a highly controlled and idealized system. Therefore, in this work we extend Cu-tmpa studies that have been limited to fundamental studies on RDEs to more applicable flow systems with a larger electrode area, to obtain insight into the effect of cell configuration on the activity and selectivity of H_2O_2 -generating molecular catalysts. Additionally, we study the influence of the different electrode configurations and electrolyte flow velocities on mass transfer limited electro-conversion, and we relate our findings to the implications for larger electrodes to provide insights helpful for scaling up electrochemical H_2O_2 -generating systems.

Replacing 2D electrodes by 3D structures can alleviate mass transfer limitations by providing a larger contact area with the electrolyte and shorter mass transport distances.[10, 16] We perform the ORR in a conventional flow-by configuration (2D), as well as in a flow-through configuration and on a flowing suspension electrode (both 3D). The flow-

by configuration consists of a flat electrode with the electrolyte flowing along its surface (Figure 4.1a), and is likely to develop a thick diffusion boundary layer and severe mass transfer limitations. The flow-through configuration has an electrically conductive foam inserted into the electrolyte flow path (Figure 4.2b), enlarging the contact area, allowing the electric current to percolate through the entire channel, and hindering the development of a thick boundary layer. The suspension electrode is composed of conductive porous microparticles suspended in an electrolyte and is flowed along a 2D current collector (Figure 4.1c). The porous particles provide an even larger surface area than the foam, while conductive networks and particle collisions also allow for electron percolation into the channel.[17–19]

Evaluating the influence of reactor design on mass transfer is essential for achieving the high product selectivity and current densities needed for advancing electrochemical H_2O_2 synthesis to an industrially relevant technology.

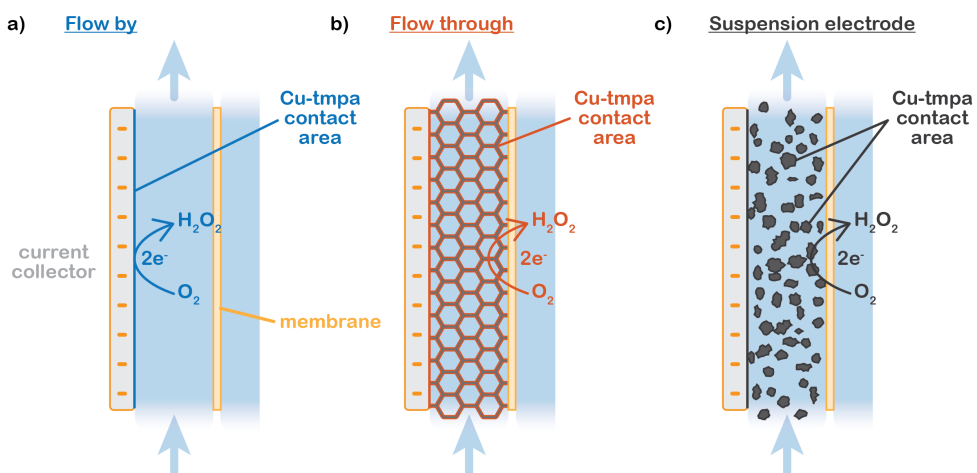


Figure 4.1: Studied current collector configurations a) flow-by, b) flow-through and c) suspension electrodes, for homogeneous catalysis of oxygen reduction by Cu-tmpa.

4.2. METHODS

Cu-tmpa was synthesized as described by Langerman et al.[14] All experiments were performed in the electrochemical flow cell and setup shown in Figure S4.1. The cathodic and anodic compartments (3 mm thick) were separated by a Nafion 117 cation exchange membrane (CEM) that was soaked and stored in electrolyte. We used a three-electrode setup, with a glassy carbon plate (Goodfellow) used as cathodic current collector in all experiments, of which an area of 2.4 by 3.4 cm was exposed to the electrolyte. This was combined with a vitreous carbon foam (3.2 mm thickness, 24 pores/cm³, 96.5% porosity, surface area 3937 m²/m³, Goodfellow) cut into the same dimension and inserted into the flow channel to create the flow-through configuration. An Ir-/Ru-oxide coated Ti-sheet (Permascand) was used as anode. A leak-free Ag/AgCl electrode (LF-1-45, Alvatek) was used as reference electrode (RE). It was inserted through the side of the flow channel

with its tip in front of the glassy carbon plate as illustrated in Figure S4.1. A small hole (\varnothing 3 mm) was made in the carbon foam at this spot to accommodate for the RE insertion.

A phosphate buffer of 0.5 M $\text{Na}_2\text{HPO}_4/\text{NaH}_2\text{PO}_4$ ($\geq 99.999\%$, Honeywell Fluka Trace-SELECT) at pH 7 was used as catholyte and anolyte to allow for comparison with previous studies[13–15], and to provide good Cu-tmpa and H_2O_2 stability and sufficient conductivity to achieve acceptable cell potentials. The catholyte was saturated with oxygen by sparging O_2 gas at 50 mL/min (controlled with mass flow controllers by Bronckhorst) during and for at least 30 minutes before the experiment. 80 mL of catholyte and anolyte were used in case of the flow-by and flow-through configurations, and 40 g of carbon suspension in 0.5 M phosphate buffer replaced the catholyte, and 40 mL of phosphate buffer was used as anolyte in the suspension electrode experiments. The suspension was prepared by adding 10 or 20 wt% of activated carbon (AC, 20 μm median particle size, 1000 m^2/g , Norit SX Plus CAT, Sigma Aldrich) to the phosphate buffer under thorough stirring, followed by 30 minutes of sonication.

Cyclic voltammetry scans (CVs) were performed at a scan rate of 100 mV/s using an IviumStat ($\pm 5\text{A}/\pm 10\text{V}$, Ivium) potentiostat (see the SI for more details). The scans were performed at various flow speeds (peristaltic pump, L/S Precision Pump System, Masterflex) before and in between two additions of 5 μM of Cu-tmpa to investigate the effect of flow and catalyst concentration on the limiting current.

The ORR performance was evaluated during chronoamperometry at a cathode potential close to the half-wave potential ($E_{\text{cat}/2}$) of 0.3 vs RHE found in previous studies[13, 14] that results in roughly 75% of the peak current. This allowed us to push the current densities towards their maximum without entering the mass transfer limited regime in the CVs. As the catalytic peaks were not visible in the CV scans of the suspension electrodes, the suspension CAs were run at the potentials selected for the flow-by and flow-through configurations. Each CA was run for 1 hour at a flow velocity inside the catholyte channel of 19 mm/s when using the flow-by and flow-through configurations, and at a lower flow velocity of 9 mm/s when using a suspension electrode to prevent operational complications such as clogging over the course of the experiment. The H_2O_2 concentration was measured periodically with a reflectometer (RQflex[®] 20, Merck) and corresponding peroxide test strips (0.2-20.0 mg/L H_2O_2). The accuracy of the test strips for measuring peroxide in phosphate buffer has been verified in ref. [15]. The samples were diluted with buffer to fit the detection window of the test strips whenever necessary. The precise reaction conditions of each experiment are listed in Table S4.1.

The stability of H_2O_2 in the different experimental conditions was tested by adding a known amount of H_2O_2 and measuring the concentration in the liquid at time intervals. In case of the flow-by and flow-through configurations, the flow cell was assembled as described above. The anolyte compartment was filled with electrolyte and closed off while 72 g of buffer was cycled through the catholyte compartment at 40 mL/min (9 mm/s inside the channel). In case of the suspension electrode, the H_2O_2 concentration was monitored after addition to 80 g of the 10 wt% AC suspension under continuous stirring inside a glass bottle. The first sample was taken 30 s after each addition and passed through a filter (Whatman Puradisc H-PTFE syringe filters, 0.2 μm , hydrophilic) to remove the AC before measuring the H_2O_2 concentration with the reflectometer. Taking the sample and filtering took about 10 minutes.

A similar experiment was performed to investigate whether the H_2O_2 was decomposed or adsorbed by the AC particles. Known amounts of H_2O_2 were injected into the 10 wt% AC suspension inside a gas-tight bottle and gas samples were taken and analyzed with a gas chromatograph (GC, CompactGC^{4.0}, Interscience) to track O_2 evolution.

4.3. RESULTS AND DISCUSSION

4.3.1. FLOW-THROUGH CONFIGURATION IMPROVES THE H_2O_2 PRODUCTION

We measured the current density of the ORR and concentration of produced H_2O_2 in the electrolyte during 1 hour of chronoamperometry for comparison of the electrochemical performance in each configuration. Figure 4.2a shows a significant difference in the achieved current densities among the different configurations, with the 20 wt% AC suspension reaching the highest current density of $-7.7 \pm 0.9 \text{ mA/cm}^2$, about twice the current density reached in the 10 wt% AC suspension ($-3.0 \pm 0.3 \text{ mA/cm}^2$) and the flow-through electrode ($-3.8 \pm 0.4 \text{ mA/cm}^2$), and almost 26 times higher than the flow-by configuration, which reaches only $-0.3 \pm 0.0 \text{ mA/cm}^2$.

In addition, we observe a steady decrease in current density in all systems during chronoamperometry, especially those operating at higher current densities. The Faradaic efficiency (FE) decreases over time as well, in the flow-by and flow-through configurations (Figure 4.2b). Both effects decrease the H_2O_2 formation rate over time. We suspect that this is due to two complications. First, the decrease in selectivity over time can be caused by the increasing concentration of H_2O_2 , both in the reservoir and through the height of the cell, leading to increased Faradaic over-reduction of the produced H_2O_2 to form H_2O and resulting in a lower measured FE towards H_2O_2 . This is especially an issue in the flow-through configuration, in which the H_2O_2 concentration increases most severely and even exceeds the O_2 concentration after about 36 minutes of operation, as shown in Figure 4.2d. While such concentrations generally do not lead to a loss in FE when using an RDE[15], H_2O_2 accumulation has been shown to decrease selectivity in flow cells.[20] The produced H_2O_2 spends a significantly longer time near the electrode before getting diluted inside the reservoir, compared to a setup using an RDE. This essentially increases the risk of H_2O_2 reduction. Secondly, the overall decrease in current density over time can be caused by slow dissolution of O_2 in the reservoir. To illustrate, all dissolved O_2 will be consumed within 9 minutes at the ORR rate reached in the flow-through configuration if no fresh O_2 is supplied (see SI for calculation). Reaching a sufficiently high dissolution rate to keep up with the O_2 consumption and maintain the maximum O_2 concentration is challenging and unlikely when using a simple sparger for saturation.[10] Both the O_2 depletion and H_2O_2 accumulation contribute to altering the $\text{O}_2/\text{H}_2\text{O}_2$ ratio near the electrode and affect the ORR and the hydrogen peroxide reduction reaction (HPRR) rates according to $\text{ORR rate} = k_{\text{ORR}}[\text{Cu-tmpa}][\text{O}_2]$ and $\text{HPRR rate} = k_{\text{HPRR}}[\text{Cu-tmpa}][\text{H}_2\text{O}_2]$, increasing the HPRR rate during the chronoamperometry. In turn, this also lowers the overall current density because k_{HPRR} is an order of magnitude lower than k_{ORR} . [13] The combination of these two effects ultimately leads to a more severe loss in partial H_2O_2 current density in the flow-through than in the flow-by case (Figure 4.2c).

Despite the lower selectivity, the flow-through configuration displays the highest partial H_2O_2 current density at all times (Figure 4.2c). The higher H_2O_2 production rate results in almost 10 times more H_2O_2 being produced in the flow-through than in the flow-by configuration within one hour of operation (Figure 4.2d). The flow-through setup produces concentrations in the mM range, which is already sufficiently high for applications like H_2O_2 /UV disinfection.[21]

Although the total current densities achieved in the suspension electrodes almost match (for 10 wt% AC) or even surpass (for 20 wt% AC) the total current density reached in the flow-through configuration, no H_2O_2 was detected in the suspensions. We suspect that the suspensions are interfering negatively with the reaction because the glassy carbon plate used in the flow-by system is also present here and was expected to allow for at least some H_2O_2 production. We address this issue later.

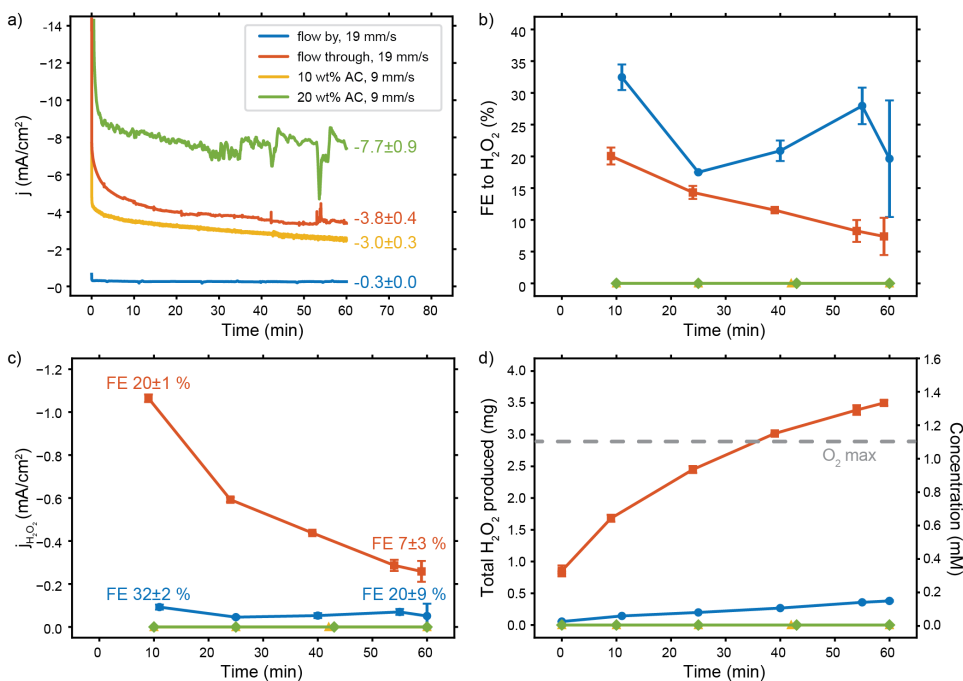


Figure 4.2: Overall performance of O_2 reduction by $10 \mu\text{M}$ Cu-tmpa in 0.5 M phosphate buffer (pH 7) on flow-through, flow-by and suspension (10 and 20 wt% AC) electrodes. a) Chronoamperometry showing the differences in achieved current densities through time, performed at 0.31 V vs RHE for the flow-by and 10 wt% suspension, and 0.21 V vs RHE for the flow-through and 20 wt% suspension. The 20 wt% AC graph has been smoothed through a running average over 30 s to remove excessive noise. b) Measured FE towards H_2O_2 production, and c) achieved partial current density to H_2O_2 ($j_{\text{H}_2\text{O}_2}$) through time. d) Resulting cumulative H_2O_2 production over time in mg and mM. The H_2O_2 concentration exceeds the maximum O_2 concentration after 36 minutes of operation in the flow-through configuration.

4.3.2. ELECTRODE CONFIGURATION AND FLOW CONDITIONS ENHANCE MASS TRANSFER

We performed CV scans to further study what current densities can be reached in our H₂O₂ synthesis systems and how this relates to the applied potential and electrolyte flow velocity. The CV scans for the different electrodes and different flow velocities are shown in Figure 4.3. The current increases most sharply between roughly 0.4 and 0.2 V vs RHE, depending on the configuration. This is in line with previous studies, wherein the half-wave potential ($E_{\text{cat}/2}$) was found at 0.3 V vs RHE. [13, 14]

First we consider the CVs of the flow-by (Figure 4.3a) and the flow-through (Figure 4.3b) cases. The flow-by configuration leads to a typical peak-shaped CV with a peak current in the forward scan caused by the transition from saturated O₂ conditions at the electrode surface to the formation of a depleted diffusion boundary layer. The peak is followed by a plateau towards the cathodic vertex, where the O₂ at the surface has already been depleted and the current is limited by O₂ transport from the freshly delivered bulk electrolyte. Increasing the flow velocity increases the peak current and the plateau current to a certain extent by lowering the residence time and reducing the boundary layer thickness, respectively.

The flow-through configuration (Figure 4.3b) reaches a significantly higher geometrical current density of 5-15 times, depending on the flow rate, compared to the highest peak current in the flow-by configuration (Figure 4.3a). The active surface area per flow cell area is increased 13.5 times by the porosity of the flow-through electrode compared to the flow-by plate electrode (see SI for calculation). This suggests that most of the increase in geometric current density is due to the larger active surface area. However, the difference in CV shape reveals that also the mass transfer conditions depend on the electrode systems. The lowest flow velocity (5 mm/s) for flow-through results in a similar shape as we have seen in the flow-by configuration, but with a less pronounced peak at 0.25 V. The peak shape transforms to resemble an S-shape voltammogram with increasing flow velocity and is completely invisible when applying higher flow velocities (28 and 37 mm/s). The plateau shape in the CV indicates that a constant O₂ supply is available, which corresponds with O₂ transport from the bulk instead of O₂ from a transient boundary layer build-up. The transition towards a steady-state diffusion (S-shape) at relatively low flow velocities suggests that the boundary layer in the flow-through is much thinner than in the flow-by case. This makes sense as the 3D character of the foam forces a frequent restart of the boundary layer development along the length of the channel. Therefore, the foam reduces the boundary layer thickness compared to the flow-by system, in which the diffusion boundary layer continues to develop along the entire channel length, resulting in an ever-increasing boundary layer thickness along the current collector surface. We estimate the average boundary layer thickness (δ) in the flow-by configuration at 180 μm , versus 11 μm in the flow-through configuration, using $\delta = D/k$, with D the diffusion coefficient of O₂ in water, and k the mass transfer coefficient. [22, 23] We obtain the mass transfer coefficients of a plate and foam, k_{plate} and k_{foam} , respectively, later with equations 4.3-4.5.

Although suspension electrodes give even higher current densities compared to the flow-by and flow-through configurations (Figures 4.3c and d), the ORR performance cannot be compared from these scans. The steep slope of the ORR that is expected be-

low 0.6 V vs. RHE is clearly present in the other flow configurations, but is not visible when using the suspension electrodes and we do not see a difference between the experiments in presence or absence of catalyst. The high currents seem to be due to the high capacitance of the suspensions, caused by the large surface area of the porous carbon particles. This agrees with the increase in hysteresis when comparing the 10 wt% (Figure 4.3c) with the 20 wt% (Figure 4.3d) AC suspension, as the increase in carbon loading raises the capacitance for two reasons: 1) a higher carbon loading results in a larger surface area, and 2) a higher carbon loading also gives higher conductivity and more percolation into the bulk of the electrode, making more surface area accessible for capacitive charging.[24] The large capacitance of the suspensions makes it impossible to observe an onset potential for the ORR in CVs and shows that at least part of the current during chronoamperometry can be attributed to electric double layer (EDL) charging.

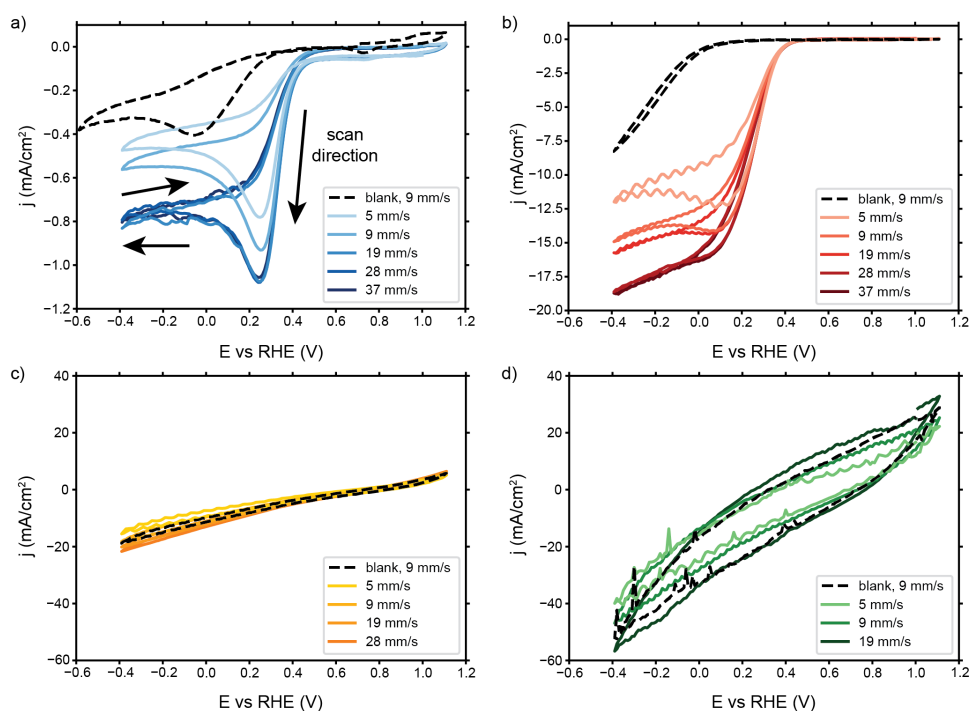


Figure 4.3: CV scans of 5 μ M Cu-tmpa in O₂-saturated 0.5 M phosphate buffer of pH 7 under various flow velocities with a) glassy carbon plate (flow-by), b) glassy carbon foam (flow-through), c) 10 wt% AC suspension, and d) 20 wt% AC suspension electrodes, at a scan rate of 100 mV/s. The black dashed lines correspond to blank measurements without any Cu-tmpa present. The blank measurement in the flow-by shows an extra reduction peak at an earlier onset potential or ORR on glassy carbon than in the flow-through configuration due to a contaminant. Nevertheless, addition of Cu-tmpa clearly increases the current and decreases the onset potential in the flow-by and flow-through systems, but not in the suspensions. Current fluctuations are visible in some scans, we suspect these are caused by the pulsed flow from the peristaltic pump.

4.3.3. CATALYST CONCENTRATION AND STABILITY

We performed CVs with Cu-tmpa concentrations of 5 and 10 μM to check whether the current is limited by catalyst availability in addition to O_2 availability. Doubling the Cu-tmpa concentration had no significant effect on the reached currents in any of the configurations, shown in Figures 4.4a and 4.4b for the flow-by and the flow-through configurations, respectively (see SI for the suspensions). This is in line with observations inside this concentration range in RDE systems.[15] The altered shape of the scans performed on the flow-through with 5 versus 10 μM Cu-tmpa was caused by a short contact loss of the RE while scanning the positive potentials, etching the foam surface and causing a larger EDL to become visible in the CVs. The potential range of interest remained unaffected and we conclude that neither system is limited by the low Cu-tmpa concentration.

In addition, we performed CVs after 1 hour of catalysis ("after CA" curves in Figure 4.4) at the indicated chronoamperometry (CA) potentials to check the catalyst stability. The shape and reached currents are very similar to those before the CA, suggesting that loss of catalytic activity or Cu-tmpa degradation are no likely causes for the FE loss through time observed in Figure 4.2. Cu-tmpa reached a turnover number (TON) of 130 during the experiments, which is likely considerably lower than the maximum TON Cu-tmpa can reach in catalysis of the ORR. Previous studies have shown that a TON of at least 250 is achievable.[15] However, very subtle differences can be observed in the CVs. The slight increase in slope in the flow-by configuration is caused by an increase in available reactant in the form of H_2O_2 , and the slight broadening of the flow-through CV can indicate further etching of the foam surface during additional CVs before catalysis. The suspension CVs (Figure S4.2) show a decrease in current after catalysis, which is in line with the capacitive nature of the suspensions and our observations from Figures 4.3c and 4.3d.

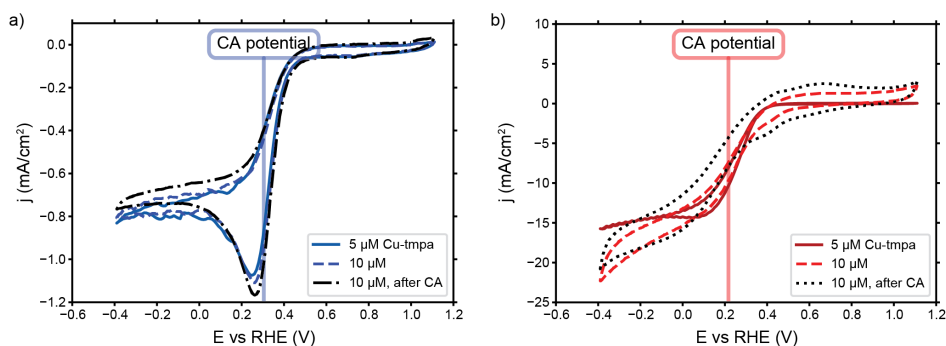


Figure 4.4: Influence of Cu-tmpa concentration and 1 hour of chronoamperometry (CA) on CV scans at a scan rate of 100 mV/s and an electrolyte flow velocity of 19 mm/s with a) a glassy carbon plate (flow-by), and b) glassy carbon foam (flow-through) as current collectors. The vertical line indicates the potential applied during CA.

4.3.4. AC SUSPENSIONS BREAK DOWN H_2O_2

Even though the activated carbon suspensions show a non-Faradaic response due to their large capacitance, the applied potential was equal to the flow-by and flow-through

cases, and sufficient for catalysis of the ORR. However, we did not detect any H_2O_2 production when applying a potential for a long period of time (Figure 4.2). To investigate this further, we studied the stability of H_2O_2 in a stirred suspension of 10 wt% AC without a potential applied. We added known concentrations of H_2O_2 to the suspension and measured the concentration in the electrolyte within 10 minutes after each addition (Figure 4.5a). No H_2O_2 was detectable in any of these measurements, showing that it vanishes rapidly after addition to an AC suspension via a non-Faradaic process. In contrast, no H_2O_2 loss was observed while pumping electrolyte with known H_2O_2 concentrations through the flow-by and flow-through configurations.

We performed the same experiment in a gas-tight bottle and analyzed the evolving gases to determine whether the suspension decomposes or adsorbs the added H_2O_2 on its large surface area. Gas-phase analysis showed formation of significant amounts of O_2 upon addition of H_2O_2 to the suspensions (Figure 4.5b). This shows that the H_2O_2 disproportionates on the AC particles via $2\text{H}_2\text{O}_2 \longrightarrow 2\text{H}_2\text{O} + \text{O}_2$. Figure 4.5c shows how much of the added H_2O_2 has decomposed over time and that the AC particles can break down all added H_2O_2 within 2 hours. Note that the concentration added in this experiment is 6 times higher than the eventual concentration formed in 1 hour of catalysis in the flow-through configuration, according to Figure 4.2. In addition, we also detected smaller amounts of CO_2 forming, which can indicate the oxidation of the carbon particles by H_2O_2 .

Hence, we have shown that the AC suspensions would decompose any H_2O_2 produced by the ORR through non-Faradaic disproportionation, in addition to the already competing Faradaic HPRR. The fast H_2O_2 decay prevents us from monitoring how much is produced in the suspension electrodes during chronoamperometry (Figure 4.2a). Although the suspension electrodes rival (10 wt% AC) and even surpass (20 wt% AC) the flow-through configuration in terms of achieved current density, we conclude that either no H_2O_2 was produced on the suspension electrodes, or any produced H_2O_2 was rapidly decomposed on the suspension particles' large surface area. Therefore, the AC particles used in this study are not suitable for use in H_2O_2 production systems. As a result, the envisaged advantages of using the suspension electrode configuration depicted in Figure 4.1c could not be realized in this work.

Nevertheless, carbon-based ORR catalysts have been studied extensively in literature and are considered to have great prospect.[8, 25] Suspensions of carefully selected carbon materials may not exhibit the issues we encounter here. Materials such as carbon black (CB), carbon nanotubes (CNTs), and graphene-based materials are commonly used in suspension electrodes[18, 26, 27], and can be modified to act as ORR catalyst[8, 9] as well. Such modified CB, CNT, and graphene-based materials would be promising to test as a suspension electrode for H_2O_2 production. Alternatively, a small amount of flowing carbon-based catalyst can be used in combination with a conductive foam to replicate the flow-through configuration with a heterogeneous catalyst instead of Cu-tpmpa.

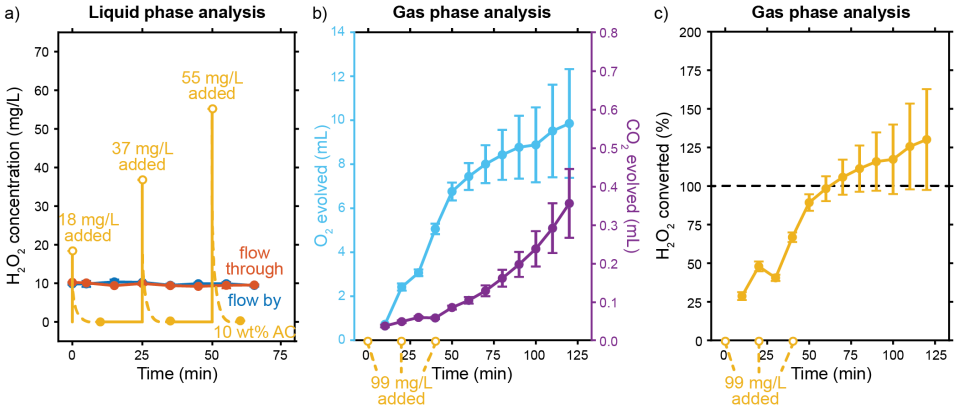


Figure 4.5: Results showing the 10 wt% activated carbon (AC) suspension breaking down H₂O₂ in solution. a) Measured H₂O₂ concentrations through time after one addition of 10 mg/L H₂O₂ in case of the flow-by, flow-through case, and after additions of 18, 37 and 55 mg/L H₂O₂ to the 10 wt% AC suspension case, spaced 25 mins apart. H₂O₂ disappears before the concentration in the liquid phase of the suspension can be measured. b) O₂ evolution through time after adding H₂O₂ to the 10 wt% AC suspension. Smaller amounts of CO₂ evolve as well. c) Percentage of the H₂O₂ added that has been decomposed by the 10 wt% AC suspension, as calculated from the O₂ evolution through time.

4.3.5. COMPARING LIMITING CURRENT DENSITIES TO SHERWOOD CORRELATIONS

Having established that a flow-through electrode offers a major advantage in mass transport compared to flow-by electrodes, we can further study the physical cause of the higher limiting current densities. The electrolyte flow velocity and the channel properties influence the limiting current density (j_{lim}) of a mass transfer limited reaction through the Sherwood number (Sh). A higher Sherwood number represents an increased mass transfer coefficient (k) and a decreased diffusion boundary layer thickness (δ), leading to a higher limiting current density through equations 4.1-4.3, [22, 23]

$$j_{lim} = \frac{DnFc_{bulk}}{\delta} \quad (4.1)$$

$$\delta = \frac{D}{k} \quad (4.2)$$

$$k = \frac{ShD}{d_c} \quad (4.3)$$

in which D is the diffusion coefficient, n the number of electrons involved in the reaction, F the Faraday constant, c_{bulk} the reactant concentration outside the diffusion boundary layer, and d_c the characteristic length.

The Sherwood number along a planar electrode in laminar flow with a fully developed hydrodynamic boundary layer is given by [23]

$$Sh = 1.467 \left(\frac{2}{1+\gamma} \right)^{0.33} \left(Re Sc \frac{d_h}{L} \right)^{0.33} ; \quad \gamma = \frac{B}{L} ; \quad d_h = 2BW(B+W) \quad (4.4)$$

in which γ is the aspect ratio of the electrode, and d_h is the hydrodynamic diameter of the channel. These are determined by the electrode length (L), electrode and channel breadth (B), and channel depth (W). The Sherwood number of flow through a porous electrode can be estimated with[28]

$$Sh = (7 - 10\epsilon + 5\epsilon^2) (1 + 0.7Re^{0.2} Sc^{0.33}) + (1.33 - 2.4\epsilon + 1.2\epsilon^2) Re^{0.7} Sc^{0.33} \quad (4.5)$$

where ϵ is the porosity. Both expressions make use of the Reynolds (Re) and Schmidt (Sc) numbers, given by equations 4.6 and 4.7, respectively.

$$Re = \frac{u d_c}{\nu} \quad (4.6)$$

$$Sc = \frac{\nu}{D} \quad (4.7)$$

which include the superficial flow velocity (u), the kinematic viscosity (ν) of the electrolyte, and a characteristic length scale d_c . The value of d_c is defined as d_h (hydrodynamic diameter) for the flow-by configuration and as d_s (typical strut size) for the flow-through electrode. We use equations 4.4 and 4.5 to obtain the Sherwood numbers at relevant flow velocities in the flow-by and flow-through configurations, respectively. The only flow velocity-dependent term in both equations is the Reynolds number, so we expect that $Sh \propto Re^{0.33}$ in the flow-by and approximately $Sh \propto \alpha Re^{0.2} + \beta Re^{0.7}$ in the flow-through electrode. Figure 4.6 shows the limiting current density at various flow velocities as estimated from CV scans (see SI for method). We compare the experimental results with the limiting current densities expected from the obtained Sherwood numbers via

$$Sh = \frac{d_c}{D} k = \frac{d_c}{D} \frac{j_{lim}}{n F c_{bulk}} = a \cdot j_{lim} \quad (4.8)$$

by fitting them to the limiting current density in the 5 μ M Cu-tmpa solution at the lowest flow velocity (5 mm/s) via the factor a . The shaded areas in Figure 4.6 indicate the expected limiting current densities. Both configurations follow the predicted trends with $Sh \propto Re^{0.33}$ and $Sh \propto \alpha Re^{0.2} + \beta Re^{0.7}$ quite well. For the flow-through case, the dominance of the first term ($\alpha \approx 15.3\beta$) gives a weaker flow velocity-dependence of approximately $Sh \propto \alpha Re^{0.2}$ in the low Re laminar flow regime compared to the flow-by electrode. The flow-by electrode benefits more from increased flow because of the severe diffusion boundary layer development over the electrode length, while the flow-through electrode keeps a thinner boundary layer already at low flow velocities because of the shorter developing lengths along the individual struts.

The second term of equation 4.5, for the flow-through electrode, will get larger than the first term when the Reynolds number exceeds 234, which mitigates the flattening of the curve. This situation is unlikely to occur in channels with dimension that are

typically used in electrolyzers. To illustrate, flow velocities of 5-40 mm/s give Reynolds numbers of only 1-8 in our flow cell. The threshold for Re can be lowered by using a flow-through electrode with lower porosity, but that will add to the pressure drop and pumping costs, as will increasing the flow rate.

Overall, we have shown that the type of current collector configuration (flow-by versus flow-through) can be used to boost the limiting current 15-25 times (see Figure S4.5). The current density can be raised further by increasing the flow velocity and the achieved improvement fits well with our expectations from Sherwood correlations. However, flowing faster boosts the limiting current to a much smaller extent than the electrode shape. Therefore, changing the electrode design is more effective than changing the flow rate.

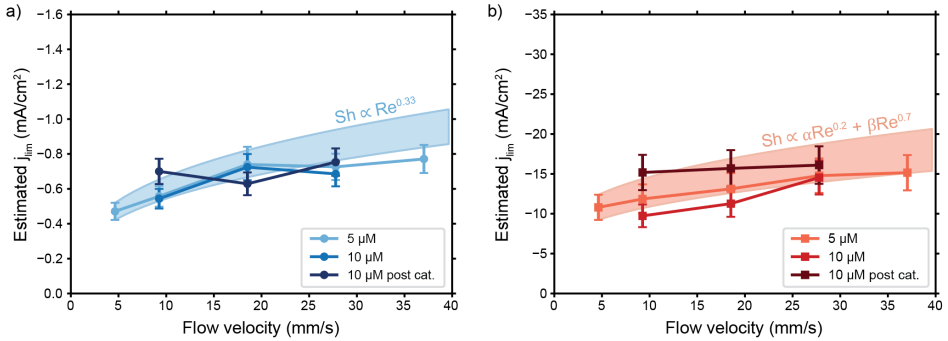


Figure 4.6: Estimated current densities in the a) flow-by and b) flow-through configurations at various flow velocities and catalyst concentrations obtained from CV measurements recorded before and after 1 hour of chronoamperometry. Our method for estimating the limiting current densities and the errors is included in the SI. The shaded areas indicate the expected increase in j_{lim} of the 5 μM line with flow velocity based on $Sh \propto Re^{0.33}$ and $Sh \propto \alpha Re^{0.2} + \beta Re^{0.7}$ as indicated.

4.3.6. IMPLICATIONS FOR SCALE UP

Although the flow-through configuration alleviates mass transfer limitations on the microscale, the low amount of O_2 available in the bulk of the electrolyte can pose an issue through O_2 depletion along the height of the cell, especially when extrapolating to larger electrolyzers. The local current density is dependent on the local O_2 concentration and will thus decrease along the height of the channel as O_2 is consumed and the bulk concentration decreases. We derive the O_2 concentration profile from the microscopic mass balance (derivation available in the SI, section 4.5), which results in

$$c(x) = c_0 e^{-\frac{kA_V}{u}x} \quad (4.9)$$

in which c_0 is the inlet concentration, and A_V is the specific surface area of the foam. The local geometric current density is given by

$$j_{loc}(x) = nFkA_V c(x)W = nFkA_V W c_0 e^{-\frac{kA_V}{u}x} \quad (4.10)$$

and can be integrated along the electrode length to yield the average geometric current density (j_{avg})

$$j_{avg} = \frac{nFWc_0u}{L} \left(1 - e^{-\frac{k_{AV}L}{u}} \right). \quad (4.11)$$

We use equation 4.11 to extract an experimental mass transfer coefficient ($-k_{u=0.019}^{exp}$) at a flow velocity of 19 mm/s by inserting the average achieved current density over the first 5 minutes of chronoamperometry. We estimate the mass transfer coefficient for various flow velocities by multiplying the theoretical mass transfer coefficient (k^{th}), obtained from equations 4.3 and 4.5, with a factor $k_{u=0.019}^{exp} / -k_{u=0.019}^{th}$ to correct for the discrepancy between theory and our experimental setup.

We evaluate a system with an FE for ORR of 100%, and we study the influence of flow velocity on the local O₂ concentration and the resulting average geometric current density. We calculate the concentration profile with equation 4.9 (Figure 4.7a) along the 3.4 cm long flow-through electrode (solid orange line) used in our experiments and use this to extrapolate the O₂ concentration expected for much longer electrodes (dashed orange line). The O₂ concentration decreases significantly along a 50 cm long electrode and results in an outlet concentration of only 0.1 mM, versus an inlet concentration of 1.1 mM. The ORR current density is highly dependent on the local O₂ concentration and will thus decrease accordingly higher up in the channel. In turn, O₂ depletion along the electrolyzer channel lowers the average geometric current density (Figure 4.7b). Therefore, even a system with perfect selectivity will be limited by the amount of O₂ as it is scaled up.

Increasing the flow velocity improves the situation considerably in terms of preventing O₂ depletion along the channel (Figure 4.7a) and results in a higher average geometric current density (Figure 4.7b). The higher flow velocity increases the limiting current density in two ways; first, the higher flow rate supplies more fresh electrolyte, which keeps the O₂ concentration high. Second, the higher flow velocity increases the mass transfer coefficient. Despite this double effect, the gain in local O₂ concentration and in average current density is the largest at relatively low flow velocities. This follows from the exponential term in equation 4.11, representing the limit of fresh electrolyte (*i.e.* the limited inflow concentration). As an example, increasing the flow velocity from 19 to 100 mm/s raises the minimum O₂ concentration 5 times and doubles the average current density, while increasing the flow velocity to 600 mm/s (a factor 30 higher than 19 mm/s) increases the current density only 4 times and induces a significant pressure drop.

The balance between increased performance and increased pumping costs with increased flow velocity should be optimized in any electrochemical flow system. As a result, typical flow velocities in comparable applications with single phase flow, such as electrodialysis, are in the order of 10-150 mm/s.[29] The j_{avg} -curve in Figure 4.7b is also steepest in this region and we expect similar flow velocities to be relevant in our flow-through system, with the most favorable trade-off between increased geometric current density and pumping costs in this regime. We estimated that the theoretical pumping power is already 34% of the electrochemical power at a flow velocity of 600 mm/s in a single-pass (calculation in SI), which makes it unpractical to flow at such high velocities.

In addition, the electrolyte flow velocity and current density control the H₂O₂ concentration in the product stream and will influence the choice between designing an electrolyte recycling- or a single-pass system. High flow velocities would require a recy-

cling system in order to achieve a sufficiently high H_2O_2 concentration, but will allow for O_2 -resaturation and maintain higher O_2 concentrations along with the increasing H_2O_2 concentration. Lower flow velocities will be necessary in a single-pass system, but such a system will have to cope with decreasing O_2 concentration during the same H_2O_2 concentration increase needed to satisfy application requirements. Therefore, the electrode height and flow velocity should be optimized to fit the current density and system requirements as well.[20, 30] Alternatively, the inlet O_2 concentration can be increased by pressurizing the system, or options for in-channel saturation, such as bubbling O_2 directly into the reaction channel, could be investigated.

Although the low O_2 solubility remains a challenge in any aqueous system, the flow-through configuration allows for higher current densities and thicker channels with larger total amounts of available O_2 compared to a flow-by configuration, while avoiding stability issues in GDEs due to salt formation[31], flooding[32], and water management in general.[33, 34] Even so, flow-through and GDE configurations are promising concepts to solve the O_2 mass transfer limitation, each with their own advantages and drawbacks. Although the stability issues in GDEs need to be considered, GDEs provide better O_2 availability in the entire channel compared to a flow-through system, whereas the flow-through system might offer easier scalability and higher stability due to the more simple and robust system design.

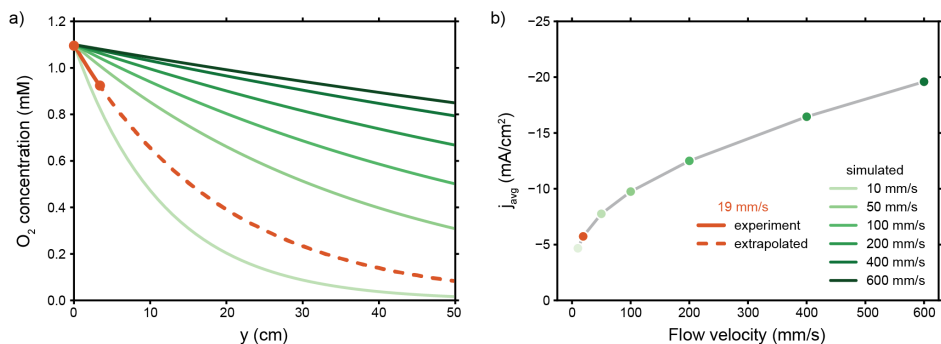


Figure 4.7: a) Estimated O_2 concentration along the height of the flow cell at various flow velocities (see legend in b). b) Average current density over a 50 cm long electrode at various flow velocities. Both estimates are based on Sherwood numbers and the average geometric current density of 5.7 mA/cm^2 during the first 5 minutes of catalysis on a 3.4 cm long electrode.

4.4. CONCLUSIONS

We electrochemically produced H_2O_2 via the two-electron ORR with Cu-tmpa as homogeneous catalyst at neutral pH in an electrochemical flow cell with different electrode configurations. We achieved similar Faradaic efficiencies for H_2O_2 to previously studied RDE systems with Cu-tmpa catalyst, while the electrode area can be extended in flow cells. This indicates that this is a promising way of scaling up this reaction. We achieved the highest current density and H_2O_2 concentrations in a flow-through configuration. The limiting current density was improved 10-25 times in the flow-through compared to

the flow-by configuration due to the larger electrode area and due to higher mass transfer coefficients in flow-through electrodes. The electrode configuration had a significantly larger effect on the limiting current than the electrolyte flow rate; the flow velocity has only a minor effect when using a small (3.4 cm long) flow-through electrode.

The high current density in flow-through electrodes was paired with increased difficulties in maintaining the initial current density and FE during chronoamperometry. The higher O_2 consumption- and H_2O_2 production rates shifted the $[O_2]/[H_2O_2]$ ratio in favor of H_2O_2 reduction and increased the competition between O_2 and H_2O_2 reduction over time. Although this resulted in the most severe performance drop in the flow-through configuration, the H_2O_2 production rate remains the highest in this configuration and the H_2O_2 concentration entered the mM range. In contrast, the suspension electrodes, that have an even higher contact area with the liquid phase, did not yield any detectable H_2O_2 . We showed that any H_2O_2 that may be produced will be immediately decomposed by the AC material, rendering this particular carbon material unsuitable for ORR to H_2O_2 .

We have demonstrated that implementing a flow-through principle in an ORR flow system can greatly reduce mass transfer limitations already at low electrolyte flow and boost H_2O_2 production rates, enabling us to produce meaningful H_2O_2 concentrations in a neutral solution with Cu-tmpa as ORR catalyst. Although the availability of O_2 is greatly improved on the microscale, it will decrease through the height of the channel and cause difficulties when scaling to larger flow cells. Here, increasing the flow rate will have a larger positive effect than in the small flow cell used in the experiments. Future studies should apply a fast O_2 saturation method to ensure the maximum O_2 concentration at the channel inlet and carefully design the electrode height, flow velocity, and recirculation ratio to suit the current density in the electrochemical H_2O_2 synthesis systems.

4.5. SUPPORTING INFORMATION

The relevant data is available in the Zenodo repository at [10.5281/zenodo.12622234](https://zenodo.org/record/12622234).

4.5.1 EXPERIMENTAL

4.5.1.1 ORR FLOW CELL AND SETUP

We used the custom-made PMMA electrochemical flow cell shown in Figure S4.1a to perform all ORR experiments. The flow cell consists of two backplates and two 3 mm thick flow channels, separated by a membrane. Both backplates have an inlay for the current collector or anode with leak-tight connections for two electrical connections from the back. The flow channels have an inlet designed to fit a micro reference electrode. We make use of two electrolyte reservoirs, which are connected to the electrochemical cell and peristaltic pumps as shown in Figure S4.1b. The catholyte reservoir is sparged with pure O₂ before and during the experiment, and is open to the air to allow for easy liquid sampling.

The glassy carbon foam is slightly thicker than the flow channel (3.2 versus 3.0 mm) to ensure good electrical contact with the current collector plate by pressing the membrane on top of the foam in between the channels. The glassy carbon plate was cleaned by polishing with 1 and 0.5 μm alumina slurries, rinsed and finally sonicated in deionized (DI) water for 16 minutes. A new piece of foam (24 by 34 mm) was cut before each experiment. A small hole (Ø3 mm) was punched in the foam at the RE inlet to accommodate RE insertion. The foam was cleaned by rinsing with DI water, sonicating in DI water for 16 minutes, and blow-drying with a nitrogen stream until no more water emerged.

The used foam had dimensions of 24 by 34 by 3.2 mm and a specific surface area of 3937 m²/m³ (specification provided by Goodfellow), resulting in surface area of 102 cm², and a total surface area (plate + foam) of 110 cm² in contact with the electrolyte. This is a factor of 13.5 times larger than the contact area of only the plate (8.16 cm²) used in the flow-by configuration.

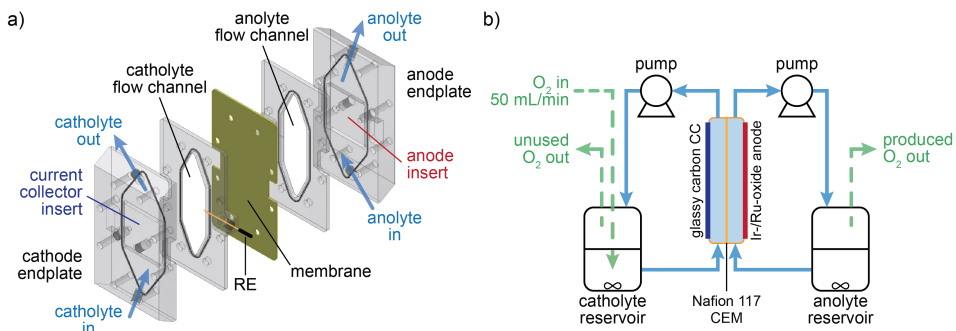


Figure S4.1: Illustration of the a) flow cell and b) setup used for the ORR experiments. Figure S1a is reproduced from the Supplementary Information of Ref. [17] with permission from the Royal Society of Chemistry.

4.5.1.2 ELECTROCHEMICAL ANALYSIS

Cyclic voltammetry scans (CVs) were performed before each chronoamperometry (CA) scan to investigate the activity of the current collectors, the influence of Cu-tmpa concentration, and flow speed. In addition, CVs were measured after each CA to check the stability of the system. We scanned between -0.4 and 1.1 V vs. RHE, at a step size of 10 mV and scan rate of 100 mV/s, for at least 3 cycles. We used a slightly larger voltage window in some cases, mostly in the suspension electrodes, to make sure that the reaction was not occurring at a higher potential.

We performed 1 hour of CA to evaluate the oxygen to H_2O_2 reaction performance in each electrode configuration. We ran each CA at the working electrode potential resulting in roughly 75% of the peak current, as determined from the CVs. No catalytic current was visible in the CV measurements with the suspension electrodes because they were dominated by the capacitive current. We therefore ran the suspension CAs at similar potentials as we did for the flow-by and flow-through configurations. The precise conditions of each experiment are listed in Table S4.1.

Table S4.1: Reaction conditions of the ORR experiments.

Cell configuration	Applied E vs. RHE (V)	Flow velocity (mm/s)
Flow-by	0.31	19
Flow-through	0.21	19
Suspension – 10 wt% AC	0.31	9
Suspension – 20 wt% AC	0.21	9

4.5.2 CATALYST CONCENTRATION AND STABILITY

CV scans of 10 (Figure S4.2a) and 20 wt% (Figure S4.2b) AC suspension electrodes with various concentrations of Cu-tmpa and O_2 -saturated electrolyte have been recorded. Scans were again performed before and after CA to check the influence of Cu-tmpa concentration and the stability during catalysis. No influence of Cu-tmpa concentration is visible in either of these scans. The post catalysis scans are notably less steep than the scans taken before catalysis. This can indicate a loss of capacitive current due to partial charging of the Electric Double Layer Capacitance (EDLC) during the CA, or a loss in conductivity due to suspension sedimentation.

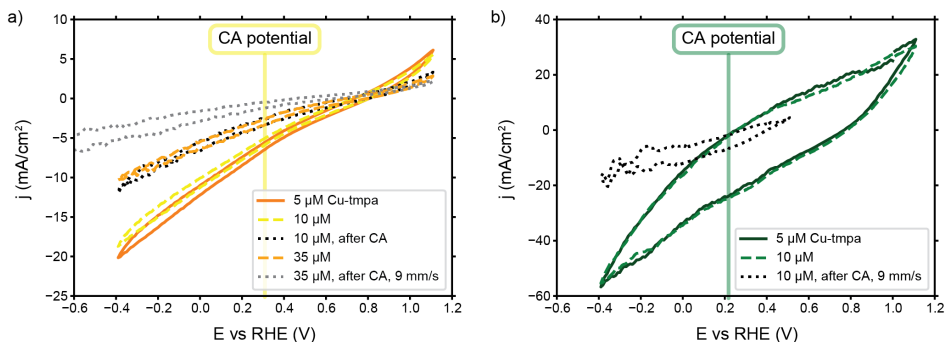


Figure S4.2: Influence of Cu-tmpa concentration and 1 hour of reaction conditions on CV scans of Cu-tmpa with a) 10 wt% AC suspension, and b) 20 wt% AC suspension as current collectors. The potential at which chronoamperometry (CA) was performed is indicated in the panels, and all scans were performed under a flow velocity of 19 mm/s, unless indicated otherwise.

4.5.3 CALCULATION OF OVERALL O_2 DEPLETION

Taking a catholyte volume of 80 mL and assuming maximum O_2 saturation of 1.1 mM at the start of the experiment, we have 0.09 mmol of O_2 available when starting the reaction. Taking the average currents during the flow-by ($-0.3 \text{ mA}/\text{cm}^2$, -2 mA) and flow-through ($-3.8 \text{ mA}/\text{cm}^2$, -31 mA)

operations, and assuming that all current consumes O_2 , we can estimate the O_2 consumption. The O_2 concentration through time, when no fresh O_2 is supplied, is shown in Figure S4.3 for both configurations. It is clear that the flow-through configuration will consume all O_2 within about 9 mins and needs a fast resaturation technology to keep up with the O_2 consumption, while this is significantly less critical in the flow-by configuration. The latter can run for 60 mins without consuming even half of the O_2 starting concentration.

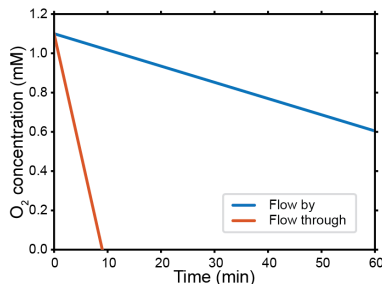


Figure S4.3: Estimated decreasing O_2 concentration in the bulk electrolyte in case of the flow-by and flow-through configurations.

4.5.4 COMPARING LIMITING CURRENTS TO SHERWOOD CORRELATIONS

4.5.4.1 ESTIMATING LIMITING CURRENTS

We estimated the limiting current in each CV scan by performing two linear fits and calculating the current at the intercept. The first line was fitted in the mass-transfer limited region (between -0.39 and -0.09 V vs RHE), the second line was fitted in the steep region close to the reaction potential of 0.3 V vs RHE (between 0.26 - 0.36 V vs RHE in case of the flow-through, and between 0.11 and 0.31 V vs RHE in case of the flow-by case). An example is shown for both a peak-shaped CV and for an S-like CV in Figure S4.4. The current density is then calculated from the measured current and the geometrical area of the current collector.

The error bars in Figure 4.3 are an indication of the maximum error caused by our choice of potential window. We estimated the errors at 10 and 14% of the calculated current density for the flow-by and the flow-through cases, respectively. We obtained these values for the errors by performing the fits over large and small potential windows and calculating the standard deviation of in current density from the intersects of all combinations of fits for one CV scan per experiment.

4.5.4.2 PREDICTING LIMITING CURRENTS FROM SHERWOOD CORRELATIONS

Here, we give the complete derivation of the local O_2 concentration inside the flow-through (foam) electrode, all input parameters are given in Table S4.2. We start with the microscopic mass balance

$$\frac{d}{dt}(c(x)BWdx) = BWuc|_x - BWuc|_{x+dx} - kA_Vc(x)BWdx \quad (S4.1)$$

and assume steady state to arrive at

$$0 = uc(x) - uc(x+dx) - kA_Vc(x)dx \quad (S4.2)$$

$$u(c(x+dx) - c(x)) = -kA_Vc(x)dx \quad (S4.3)$$

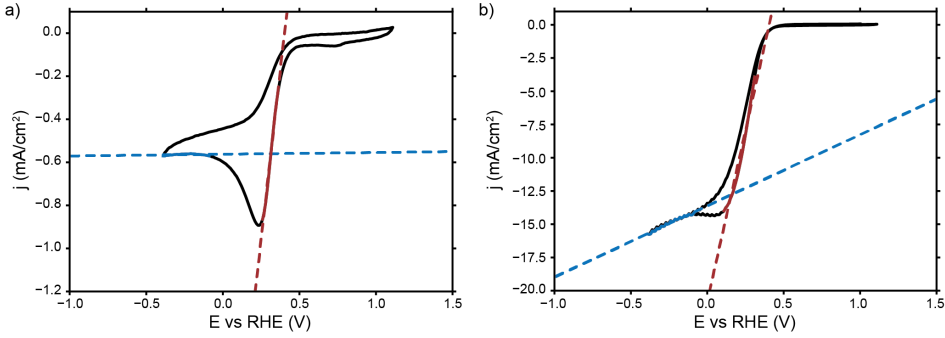


Figure S4.4: Typical CV scans in the a) flow-by and b) flow-through configurations. We estimated the limiting current densities by calculating the intercept between linear fits in the mass transfer-limited region and the region around 0.3 V vs RHE.

$$udc = -kA_V c(x) \quad (\text{S4.4})$$

$$u \frac{dc}{dx} = -kA_V c(x) \quad (\text{S4.5})$$

$$\frac{dc}{dx} = -\frac{kA_V}{u} c(x) \quad (\text{S4.6})$$

We impose the boundary condition $c(0) = c_0 (= c_{bulk})$ to get the concentration profile, which is dependent on the inlet concentration (c_0), the mass transfer coefficient (k), the specific area of the foam (A_V), the flow velocity (u), and the location (x).

$$c(x) = c_0 e^{-\frac{kA_V}{u} x} \quad (\text{S4.7})$$

The local geometric current density is then given by

$$j_{loc}(x)A = nFkA_V c(x)V \quad (\text{S4.8})$$

$$j_{loc}Bdx = nFkA_V c(x)BWdx \quad (\text{S4.9})$$

$$j_{loc} = nFkA_V c(x)W = nFkA_V W c_0 e^{-\frac{kA_V}{u} x} \quad (\text{S4.10})$$

Which can be integrated to find the average geometric current density

$$j_{avg}^{foam} = \frac{1}{L} \int_0^L j_{loc}(x) dx = \frac{nFkA_V W c_0}{L} \int_0^L e^{-\frac{kA_V}{u} x} dx = \frac{nFWc_0 u}{L} \left(1 - e^{-\frac{kA_V L}{u}}\right) \quad (\text{S4.11})$$

We used equations S4.7 and S4.11 to create Figure 4.7 in the manuscript.

The situation in the flow-by configuration is simpler because the O_2 consumption is significantly lower and we can assume that the bulk concentration is constant along the complete height of the channel ($c(x) = c_0$). This gives us an average geometric current density over the plate electrode of

$$j_{avg}^{plate} = nFk^{plate}c_0 \quad (S4.12)$$

This is equal to the limiting current on the flow-by electrode (j_{lim}^{plate}).

The expected limiting current on the flow-through electrode can be calculated in a similar manner, *i.e.* by assuming that the bulk stays O₂-saturated ($c_0 = 1.1$ mM) everywhere in the foam, and results in

$$j_{lim}^{foam} = nFk^{foam}c_0 \quad (S4.13)$$

Comparing the limiting current on the flow-by and flow-through electrodes gives an improvement factor of $j_{lim}^{foam} / j_{lim}^{plate}$. The predicted improvement factor and the experimental results are shown together in Figure S4.5. They are in good agreement at a factor of 19.5-16 for the theoretical values, and 25-15 for the experimental values. The decrease in improvement with increasing flow velocity follows from the weaker flow velocity-dependence of the Sherwood number in the flow-through versus the flow-by configuration.

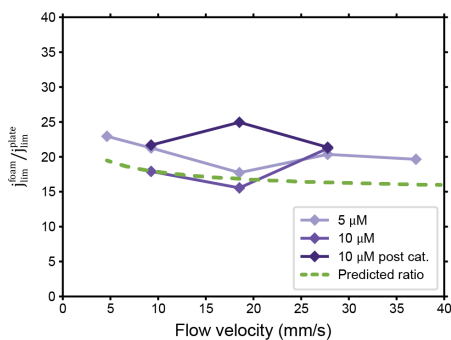


Figure S4.5: The factor ($j_{lim}^{foam} / j_{lim}^{plate}$) by which the limiting current density is increased in the flow-through compared to the flow-by configuration per flow velocity during our experiments (solid purple lines) and what we predict from Sherwood correlations (green dashed line).

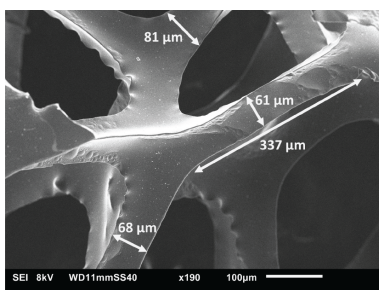


Figure S4.6: SEM image of the 60 ppi glassy carbon foam and length measurements used to estimate a typical strut size.

Table S4.2: Input parameters for Sherwood correlations and mass transfer coefficient extraction.

Shared - independent of configuration		
L	$34 \cdot 10^{-3}$ m	electrode length
B	$24 \cdot 10^{-3}$ m	electrode width
W	$3 \cdot 10^{-3}$ m	electrode-membrane spacing, channel depth
u	Experiment: $18.6 \cdot 10^{-3}$ m/s	(superficial) flow velocity
ν	10^{-6} m ² /s	kinematic viscosity
D	$2 \cdot 10^{-9}$ m ² /s	diffusion coefficient O ₂ in water
n	2	electrons transferred in reaction
F	96485 C/mol	Faraday constant
c_{bulk}	1.1 mol/m ³	maximum O ₂ concentration
Configuration-specific		
Flow-by		Flow-through
$\gamma = \frac{B}{L}$	0.71	ϵ 0.965, porosity
$d_c = d_h = 2BW(B+W)$	$5.33 \cdot 10^{-3}$ m, hydrodynamic diameter	$d_c = d_s$ $200 \cdot 10^{-6}$ m, typical strut size
A	$8.16 \cdot 10^{-4}$ m ² , electrode area	A_V 4219 m ² /m ³ , specific electrode area

4.5.5 PRESSURE DROP IN THE FLOW-THROUGH SYSTEM

The pressure drop in an ideal case of an infinitely wide channel with fully developed laminar flow can be estimated from the Darcy-Weisbach equation[35] (eqs. S4.14)

$$\Delta p = \frac{12\mu Lu}{h^2} = \frac{12\mu L^2}{t_{res} \frac{1}{4} d_h^2} \quad (S4.14)$$

in which μ is the viscosity of water (Pa·s), L is the cell length (m), u is the flow velocity (m/s), h is the channel thickness (m), t_{res} is the residence time (s), and the hydraulic diameter (d_h) can be calculated from[36, 37]

$$d_h = \frac{4\epsilon}{\frac{2}{h} + \frac{(1-\epsilon)S_{CC}}{V_{CC}}} \quad (S4.15)$$

to account for the presence of spacers or, as in our case, the presence of a foam. Here, ϵ is the foam porosity, S_{CC} is the surface (m²) of the porous current collector, and V_{CC} is the solid volume (m³) of the foam. Figure S4.7 shows the theoretical pressure drop over a 50 cm long foam at various flow rates.

Assuming a current density of 20 mA/cm² and a cell voltage of 1.5 V, an electrolyzer of 50 cm long, with a 0.3 cm thick channel, and 1 cm wide electrode, would use 1.5 W of power to perform the electrochemical reaction, the required pumping power (P_{pump}) can be calculated with

$$P_{pump} = \frac{\Delta Q}{\eta} \quad (S4.16)$$

where a flow velocity of 600 mm/s gives a theoretical pressure drop of 0.2 bar and a flow rate (Q) of 18 mL/s. Assuming a pump efficiency (η) of 70% gives a pumping power of 0.51 W, which is already 34% of the utilized electrochemical power.

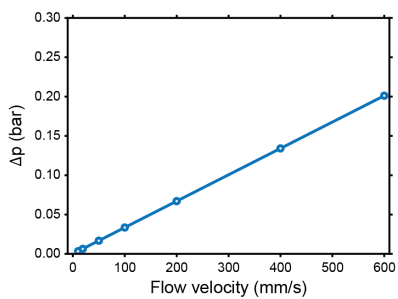


Figure S4.7: Calculated pressure drop in a flow-through cell for the ideal case of an infinitely wide channel with fully developed laminar flow.

REFERENCES

- [1] Ryoji Noyori, Masao Aoki, and Kazuhiko Sato. “Green oxidation with aqueous hydrogen peroxide”. In: *Chemical Communications* 16 (2003), pp. 1977–1986.
- [2] Gerald McDonnell. “The Use of Hydrogen Peroxide for Disinfection and Sterilization Applications”. In: *Patai's Chemistry of Functional Groups*. John Wiley & Sons, Ltd, 2014. Chap. The Use of Hydrogen Peroxide for Disinfection and Sterilization Applications, pp. 1–34. ISBN: 9780470682531.
- [3] Ronald Hage and Achim Lienke. “Applications of Transition-Metal Catalysts to Textile and Wood-Pulp Bleaching”. In: *Angewandte Chemie International Edition* 45.2 (2006), pp. 206–222.
- [4] Sara Ann Fast, Veera Gnanaswar Gude, Dennis D. Truax, James Martin, and Benjamin S. Magbanua. “A Critical Evaluation of Advanced Oxidation Processes for Emerging Contaminants Removal”. In: *Environmental Processes* 4.1 (2017), pp. 283–302.
- [5] Xiao Zhang, Yang Xia, Chuan Xia, and Haotian Wang. “Insights into Practical-Scale Electrochemical H₂O₂ Synthesis”. In: *Trends in Chemistry* 2.10 (2020), pp. 942–953.
- [6] Jose M. Campos-Martin, Gema Blanco-Brieva, and Jose L. G. Fierro. “Hydrogen Peroxide Synthesis: An Outlook beyond the Anthraquinone Process”. In: *Angewandte Chemie International Edition* 45.42 (2006), pp. 6962–6984.
- [7] Rosaria Ciriminna, Lorenzo Albanese, Francesco Meneguzzo, and Mario Pagliaro. “Hydrogen Peroxide: A Key Chemical for Today's Sustainable Development”. In: *ChemSusChem* 9.24 (2016), pp. 3374–3381.
- [8] Meng Dan, Ruyi Zhong, Shangyu Hu, Huixiang Wu, Ying Zhou, and Zhao-Qing Liu. “Strategies and challenges on selective electrochemical hydrogen peroxide production: Catalyst and reaction medium design”. In: *Chem Catalysis* 2.8 (2022), pp. 1919–1960.
- [9] Jingkun An, Yujie Feng, Qian Zhao, Xin Wang, Jia Liu, and Nan Li. “Electrosynthesis of H₂O₂ through a two-electron oxygen reduction reaction by carbon based catalysts: From mechanism, catalyst design to electrode fabrication”. In: *Environmental Science and Ecotechnology* 11 (2022), p. 100170.
- [10] José Fernando Pérez, Javier Llanos, Cristina Sáez, Conrado López, Pablo Cañizares, and Manuel Andrés Rodrigo. “Towards the scale up of a pressurized-jet microfluidic flow-through reactor for cost-effective electro-generation of H₂O₂”. In: *Journal of Cleaner Production* 211 (2019), pp. 1259–1267.
- [11] E. Berl. “A new cathodic process for the production of H₂O₂”. In: *Transactions of The Electrochemical Society* 76.1 (1939), p. 359.
- [12] Nan Wang, Shaobo Ma, Pengjian Zuo, Jizhou Duan, and Baorong Hou. “Recent Progress of Electrochemical Production of Hydrogen Peroxide by Two-Electron Oxygen Reduction Reaction”. In: *Advanced Science* 8.15 (2021), p. 2100076.

- [13] Michiel Langerman and Dennis G. H. Hetterscheid. “Mechanistic Study of the Activation and the Electrocatalytic Reduction of Hydrogen Peroxide by Cu-tmpa in Neutral Aqueous Solution”. In: *ChemElectroChem* 8.15 (2021), pp. 2783–2791.
- [14] Michiel Langerman and Dennis G. H. Hetterscheid. “Fast Oxygen Reduction Catalyzed by a Copper(II) Tris(2-pyridylmethyl)amine Complex through a Stepwise Mechanism”. In: *Angewandte Chemie International Edition* 58.37 (2019), pp. 12974–12978.
- [15] Phebe H. van Langevelde and Dennis G. H. Hetterscheid. “Selective electrochemical H₂O₂ production by a molecular copper catalyst: A crucial relation between reaction rate and mass transport”. In: *Chem Catalysis* ().
- [16] Chao Zhang, Yonghai Jiang, Yunlin Li, Zhongxin Hu, Lei Zhou, and Minghua Zhou. “Three-dimensional electrochemical process for wastewater treatment: A general review”. In: *Chemical Engineering Journal* 228 (2013), pp. 455–467.
- [17] Nathalie E. G. Ligthart, Gerard Prats Vergel, Johan T. Padding, and David A. Vermaas. “Practical potential of suspension electrodes for enhanced limiting currents in electrochemical CO₂ reduction”. In: *Energy Advances* 3.4 (2024), pp. 841–853.
- [18] Monjur Mourshed, Seyed Mohammad Rezaei Niya, Ruchika Ojha, Gary Rosengarten, John Andrews, and Bahman Shabani. “Carbon-based slurry electrodes for energy storage and power supply systems”. In: *Energy Storage Materials* 40 (2021), pp. 461–489.
- [19] Alexandra Rommerskirchen, Anna Kalde, Christian J. Linnartz, Leon Bongers, Georg Linz, and Matthias Wessling. “Unraveling charge transport in carbon flow-electrodes: Performance prediction for desalination applications”. In: *Carbon* 145 (2019), pp. 507–520.
- [20] Winton Li, Arman Bonakdarpour, Előd Gyenge, and David P. Wilkinson. “Production of Hydrogen Peroxide for Drinking Water Treatment in a Proton Exchange Membrane Electrolyzer at Near-Neutral pH”. In: *Journal of The Electrochemical Society* 167.4 (2020), p. 044502.
- [21] Michelle N. Young, Mikaela J. Links, Sudeep C. Papat, Bruce E. Rittmann, and César I. Torres. “Tailoring Microbial Electrochemical Cells for Production of Hydrogen Peroxide at High Concentrations and Efficiencies”. In: *ChemSusChem* 9.23 (2016), pp. 3345–3352.
- [22] R. Parsons. “Electrochemical nomenclature”. In: 37.4 (1974), pp. 499–516.
- [23] Stéphane J. C. Weusten, Luc C. E. M. Murrer, Matheus T. de Groot, and John van der Schaaf. “Mass transfer in 3D-printed electrolyzers: The importance of inlet effects”. In: *AIChE Journal* 67.6 (2021), e17263.
- [24] Ko Yeon Choo, Chung Yul Yoo, Moon Hee Han, and Dong Kook Kim. “Electrochemical analysis of slurry electrodes for flow-electrode capacitive deionization”. In: *Journal of Electroanalytical Chemistry* 806 (2017), pp. 50–60.

- [25] Yichan Wen, Ting Zhang, Jianying Wang, Zhelun Pan, Tianfu Wang, Hiromi Yamashita, Xufang Qian, and Yixin Zhao. "Electrochemical Reactors for Continuous Decentralized H₂O₂ Production". In: *Angewandte Chemie International Edition* 61.35 (2022), e202205972.
- [26] Bilen Akuzum, Pushpendra Singh, Devon A. Eichfeld, Lutfi Agartan, Simge Uzun, Yury Gogotsi, and E. Caglan Kumbur. "Percolation characteristics of conductive additives for capacitive flowable (semi-solid) electrodes". In: *ACS Applied Materials & Interfaces* 12.5 (2020), pp. 5866–5875.
- [27] M. Boota, K. B. Hatzell, M. Alhabeab, E. C. Kumbur, and Y. Gogotsi. "Graphene-containing flowable electrodes for capacitive energy storage". In: *Carbon* 92 (2015), pp. 142–149.
- [28] D. J. Gunn. "Transfer of heat or mass to particles in fixed and fluidised beds". In: *International Journal of Heat and Mass Transfer* 21.4 (1978), pp. 467–476.
- [29] Dipak Ankoliya, Anurag Mudgal, Manish Kumar Sinha, Philip Davies, Edxon Licon, Rubén Rodríguez Alegre, Vivek Patel, and Jatin Patel. "Design and optimization of electro dialysis process parameters for brackish water treatment". In: *Journal of Cleaner Production* 319 (2021), p. 128686.
- [30] Dhananjai Pangotra, Lénárd-István Csepei, Arne Roth, Volker Sieber, and Luciana Vieira. "Anodic generation of hydrogen peroxide in continuous flow". In: *Green Chemistry* 24.20 (2022), pp. 7931–7940.
- [31] Eric W. Lees, Benjamin A. W. Mowbray, Fraser G. L. Parlane, and Curtis P. Berlinguette. "Gas diffusion electrodes and membranes for CO₂ reduction electrolyzers". In: *Nature Reviews Materials* 7.1 (2022), pp. 55–64.
- [32] Kailun Yang, Recep Kas, Wilson A. Smith, and Thomas Burdyny. "Role of the Carbon-Based Gas Diffusion Layer on Flooding in a Gas Diffusion Electrode Cell for Electrochemical CO₂ Reduction". In: *ACS Energy Letters* 6.1 (2021), pp. 33–40.
- [33] Lorenz M. Baumgartner, Christel I. Koopman, Antoni Forner-Cuenca, and David A. Vermaas. "Narrow pressure stability window of gas diffusion electrodes limits the scale-up of CO₂ electrolyzers". In: *ACS Sustainable Chemistry & Engineering* 10.14 (2022), pp. 4683–4693.
- [34] Bert De Mot, Jonas Hereijgers, Miguel Duarte, and Tom Breugelmans. "Influence of flow and pressure distribution inside a gas diffusion electrode on the performance of a flow-by CO₂ electrolyzer". In: *Chemical Engineering Journal* 378 (2019), p. 122224.
- [35] David A. Vermaas, Enver Guler, Michel Saakes, and Kitty Nijmeijer. "Theoretical power density from salinity gradients using reverse electro dialysis". In: *Energy Procedia* 20 (2012), pp. 170–184.
- [36] A. R. Da Costa, A. G. Fane, and D. E. Wiley. "Spacer characterization and pressure drop modelling in spacer-filled channels for ultrafiltration". In: *Journal of Membrane Science* 87.1 (1994), pp. 79–98.
- [37] G. Schock and A. Miquel. "Mass transfer and pressure loss in spiral wound modules". In: *Desalination* 64 (1987), pp. 339–352.

5

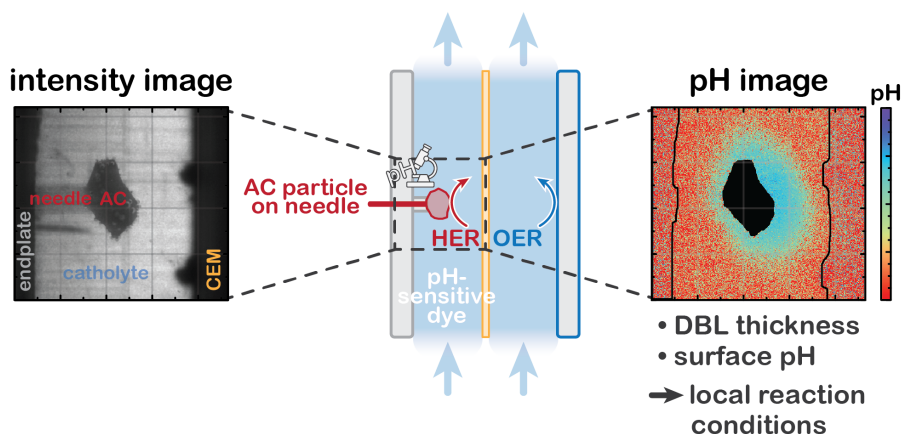
IMAGING LOCAL pH IN BOUNDARY LAYERS AT 3D ELECTRODES IN ELECTROCHEMICAL FLOW SYSTEMS

Parts of this chapter have been submitted for publication as "*Imaging local pH in boundary layers at 3D electrodes in electrochemical flow systems*" by Nathalie E. G. Ligthart*, Julius Sommer*, Jorrit Bleeker, Lorenz M. Baumgartner, Johan T. Padding, and David A. Vermaas. (* Shared co-first authorship)

ABSTRACT

Electrochemical conversion reactors, such as water electrolyzers, CO₂ electrolyzers, fuel cells, and flow batteries, will be essential in electrifying industry in the ongoing energy transition. These technologies require intensification to become economically viable. Hydrodynamics and mass transfer at electrode-electrolyte interfaces significantly affect electrochemical conversion reactions by influencing the reactant availability and pH in the local reaction environment. 3D electrodes, such as flow-through foams and suspension electrodes, hold a great advantage over 2D electrodes as they moderate pH changes and reactant depletion by spreading the current over a larger electrode area and electrolyte volume. We study the diffusion boundary layer in operando around a single mm-sized particle, representing an element of a 3D electrode. We visualize the local pH with Fluorescence Lifetime Imaging Microscopy (FLIM) during H₂O reduction at various current densities and electrolyte flow velocities. FLIM enables us to map the transient pH at a resolution down to 9 μm and 2 Hz. In addition, we apply an intermittent current to investigate how long the capacitive electric double layer of a suspension electrode particle can maintain an ongoing electrochemical reaction during their time of non-contact with a current collector in applications that require Faradaic charge transfer (i.e. flow batteries, microbial fuel cells, CO₂ electrolyzers). We demonstrate that the diffusion boundary layer and pH gradients are not symmetrical, but depend on the direction of the electric field and that of the flow, and are strongly influenced by the current density and flow conditions. The substantial pH gradients and boundary layer formation at the scale of hundreds of micrometers underline the importance of controlling flow in or around electrodes, making 3D electrodes an important asset for creating suitable reaction conditions in mass transport-limited electrochemical conversions.

5



5.1. INTRODUCTION

Developing technologies for sustainable production methods in the chemical industry is essential in the energy transition and decarbonization of industry.[1, 2] Electrochemical processes are gaining interest as alternatives to thermochemical routes, for example to synthesize high-value chemicals and fuels from renewable energy sources and captured CO₂. [3] Base materials such as syngas, formic acid, and ethylene are produced in CO₂ electrolyzers as intermediates and are processed further to obtain the essential hydrocarbons without using fossil fuels as carbon source. [4, 5] Additional electrochemical reactor applications include technologies for hydrogen [6, 7], salinity gradient energy [8], energy storage [9, 10], carbon capture [11, 12], and wastewater treatment [13–16]. Although these electrochemical technologies are promising, high costs, low efficiency, and poor stability pose considerable challenges for large-scale application of electrochemical reactors. [4, 17]

Working at high current density while maintaining high product selectivity and long-term stability is challenging but essential for realizing economic viability of many of these new technologies. High current densities can cause severe local concentration gradients (or depletion) of redox active species with low solubility and can negatively affect product selectivity and catalyst stability. [18, 19] In case of proton-coupled electron transfer reactions, this causes local pH gradients, which can hamper the reaction efficiency. Therefore, fast mass transport is extremely important to counter depletion and loss of selectivity. In particular, regarding the example of electrochemical CO₂ reduction, the selectivity towards carbonaceous products critically depends on maintaining a narrow pH window of 7–8 near the electrode [20], to suppress the Hydrogen Evolution Reaction (HER). [19, 21] Just like other proton-coupled electron transfer reactions, CO₂ reduction suffers from considerable energy and selectivity losses when the pH at the surface is higher, because the high pH raises the Nernst potential and shifts the equilibrium of dissolved CO₂ towards (bi)carbonate. [21–23] Hence, understanding mass transport and pH profiles is essential to limit performance loss during operation at high current densities.

The electrode geometry is pivotal for the development of diffusion boundary layer and the pH profile near the electrode. 3D electrodes, which can be flow-through electrodes such as foams or suspension electrodes, hold a clear advantage over flat electrodes in this regard, because 1) they spread the current over a larger electrode area and electrode volume, moderating the local current density and surface pH, [24, 25] and 2) they disrupt the flow to prevent diffusion boundary layers from developing over the length of the electrode. A continuously undeveloped diffusion boundary layer improves mass transport, which is reflected in higher Sherwood numbers. [26] Flow-through electrodes are a popular choice for a variety of applications [24, 27], and flowable suspension electrodes have been found especially effective in Flow electrode Capacitive Deionization (FCDI) [28, 29], Electrochemical Flow Capacitors (EFCs) [30, 31], Redox Flow Batteries (RFBs) [10, 32], and microbial fuel cells (MFCs) [33, 34]. However, these previous works on 3D electrodes have focused on studying the performance parameters (such as power density and removal efficiency), without detailed insight in the local reaction conditions. At the same time, 3D electrodes feature strongly heterogeneous flow and concentration fields, where the diffusion boundary layer develops under flow around an electrode seg-

ment (filaments in case of flow through, particles in case of a suspension). Hence, we need to further understand the local reaction conditions in 3D electrodes and the extent to which the capacitance contributes to electrochemical conversion in suspension electrodes.

Therefore, we investigate the local pH at the electrode-electrolyte interface of a reactive particle representing an element in a 3D electrode, and we evaluate the Faradaic contribution during the discharge of a capacitive particle. We inserted a single Activated Carbon (AC) particle electrode in an electrolytic flow cell and imaged the local pH with Fluorescent Lifetime Imaging Microscopy (FLIM) [21, 35] under various current densities and flow conditions relevant for a particle in a flowing suspension. We determine the pH around the particle electrode and use the resulting OH^- concentration to extract the diffusion boundary layer thickness in all directions around the single-particle electrode during H_2O reduction as a model reaction.

In contrast to elements in a flow-through electrode, particles in a flowing suspension are not continuously in contact with a current source, but rather pick up electrons during collisions with dynamic networks and experience an intermittent current supply. We investigate whether the particle's electric double layer capacitance can maintain the ongoing Faradaic reaction long enough to mitigate the non-contact time by combining the FLIM and potentiostat data and fitting the discharge curve to a self-discharge model of Electric Double Layer Capacitors (EDLCs). [36] This allows to elucidate how often suspension particles should reestablish electrical contact to overcome the challenges of their low conductivity. [28, 30, 37]

Our findings can be extended towards other pH-sensitive reactions and different 3D electrode geometries, and are equally applicable to other mass transfer-limited reactions. We consider the OH^- produced during H_2O reduction as a proxy for local generation of electrolysis products and depletion of reactants. Furthermore, our findings on particle capacitance as electron supply during Faradaic reactions are applicable to suspension electrode applications and aid in the design of current collectors and non-contact time of the particles.

5.2. METHODS

A large AC particle ($455 \pm 23 \mu\text{m}$ radius, Norit 18x40 AG 1, Cabot) was attached to the tip of a metal needle with an electrically conductive epoxy adhesive (Eccobond 56 C). The needle and epoxy were coated with an insulating acrylic layer (nail polish) to prevent contact with the electrolyte. The AC particle electrode was placed as cathode in a two-compartment electrochemical flow cell as shown in Figure 5.1. The cell was equipped with an Ag/AgCl reference electrode (LF-1-45, Alvatek) and nickel plate (Ni-plate) anode. The channels were separated by a Cation Exchange Membrane (CEM, Selemion CMV). The anolyte consisted of 0.1 M KOH in deionized water. The catholyte consisted of 0.1 M K_2SO_4 and 0.1 mM of fluorescent quinolinium-based dye (see Figure S5.3a). [21, 35] The pH-sensitive fluorescence lifetime of this dye allows for pH measurements between pH 7 to 13 (see Figure S5.3b). The electrolytes were pumped through the cell at flow velocities ranging from 0.1 to 2.1 mm/s by two syringe pumps and collected in waste containers to create a single-pass system. All experiments were performed at constant currents between 0 and -143 mA/g carbon (corresponding to 0 to -106 mA/cm², based

on the geometric surface area of the particle) applied by a Vertex.100mA potentiostat ($\pm 100\text{mA}/\pm 10\text{V}$, Ivium). See section 5.5 of the SI for more information on the setup and dye.

FLIM was performed with a light microscope equipped with a 2.5x objective, 405 nm diode laser (20 MHz, 300 mW), a spinning disc confocal imager (X-Light V2, Crest Optics) and a FLIM Toggel camera (512x470 pixels, Lambert Instruments) resulting in a pixel size of 9 μm . The images were recorded in LIFA 1.4 software (Lambert Instruments) and processed further with an in-house developed Python script, as described in section 5.5 of the SI.

The formation and growth of the boundary layer in no-flow conditions were recorded at -43 mA/g (-32 mA/cm^2) for 150 s, with one FLIM image recorded every 0.5 s (2 Hz). To reduce noise, a running average over 3 images was used during data processing. We characterize each experiment using the Fourier number (Fo), given by[38]

$$Fo = \frac{t}{t_D} = \frac{tD_{OH^-}}{L^2} \quad (5.1)$$

in which t is the measurement time, t_D and D_{OH^-} are the diffusion timescale and the diffusion coefficient of OH^- , respectively, and we consider half the channel depth (approx. 1.8 mm) as the characteristic length scale (L). Fo gives the relative significance of the diffusion length of OH^- (numerator) versus the distance to a wall (denominator) during the transient measurement.

The influence of current and flow velocity were both studied in steady state conditions. The conditions of interest were applied for 60 s and the local pH was recorded with FLIM at a lower frequency of 1 Hz. The first 40 s were used to reach steady state, and the last 20 s were averaged to yield the results. The current density was varied between 0 and -143 mA/g (-106 mA/cm^2) at a constant flow velocity of 0.3 mm/s. Influence of flow velocity was investigated between 0.1 and 2.1 mm/s, at a constant current density of -15 mA/g (-11 mA/cm^2). We define the Reynolds (Re) number as

$$Re = \frac{uL}{\nu} \quad (5.2)$$

with u being the channel-averaged flow velocity, ν the kinematic viscosity of the liquid phase, and L the characteristic length, for which the particle diameter (d_p) is inserted to arrive at the particle Reynolds number (Re_p).

OH^- concentration gradients were modelled around a spherical particle inside a 2D flow channel in COMSOL Multiphysics 6.1 for comparison with our experimental results. The geometry was designed to resemble the experimental setup, with a ratio between the particle diameter and channel width similar to the experiments, and an imposed electrical field perpendicular to the electrolyte flow direction. See section 5.5 of the SI for further details.

5.3. RESULTS AND DISCUSSION

We used FLIM to record how the concentration boundary layer develops over time, and how it depends on current density and electrolyte flow velocity. Our results confirm established theories, but also show unexpected behavior. Please note that, unlike previous

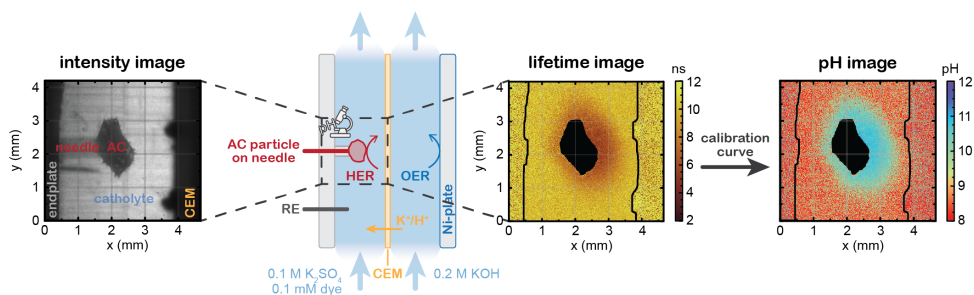


Figure 5.1: Schematic of the single AC particle electrode inside the electrochemical flow cell and the microscope imaging window. The local fluorescence intensity and lifetime of the added pH-sensitive dye are recorded. The fluorescence lifetime image is converted to a pH map, using the calibration curve shown in the SI (section 5.5).

pH mapping with FLIM[21], the current setup with a reactive particle in the middle of the flow channel has no interference from gaskets or walls, which allows us to measure the local pH very close to the reaction site.

5.3.1. BOUNDARY LAYER AND PLUME FORMATION

In the simplest case, we apply a low constant current (-43 mA/g , -32 mA/cm^2) without convection by applied flow or detaching hydrogen bubbles. As expected, a region with increased pH, that corresponds to the diffusion boundary layer, forms after starting the current and grows significantly over time (see Figures 5.2a-e) as OH^- is produced and transported away from the electrode surface by migration and diffusion. The placement of the anode on the right side of the particle causes a stronger electric field and increased local ionic current density (j_L), with a higher ion flux, on the right side of the particle (see Figure 5.2f for a modeled spherical particle electrode). The asymmetrical system, in combination with migration in the direction of the membrane and the irregular shape of the electrode, causes the boundary layer to grow asymmetrically, with a thicker layer on the side of the particle that is facing the anode (see Figures 5.2c-e). The buildup of OH^- ions is analogous to consumption of reactants, and should be considered when performing pH-sensitive reactions or when working with poorly soluble reagents.

We processed the measured pH maps to obtain a more quantitative analysis of the boundary layer thickness (δ) by casting rays from the exterior of the particle into the electrolyte and extracting the boundary layer thickness along each ray. The rays were cast at a slightly modified angle from the exterior normal, as described in section 5.5 of the SI, to prevent excessive crossing of the rays. Figure 5.3a shows the particle electrode with several rays (A, B, C, and D) and their mirror images (A', B', C', and D'). We fit a linear graph to the difference between the bulk- and local OH^- concentration (ΔC_{OH^-}) in the region close to the particle and define the x-intercept as the diffusion boundary layer thickness. This is shown for ray C at three different times (t_1 , t_2 , and t_3) in Figure 5.3b. For the rays A, B, C, D (and their mirror images), the estimated boundary layer thickness is indicated by a colored dot in Figure 5.3a. The white dots indicate the end of the boundary layer on all rays in between those shown in this figure. The analysis is

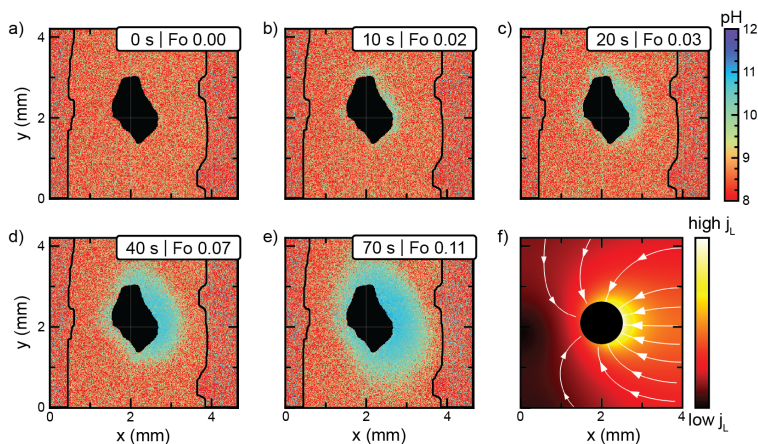


Figure 5.2: Development of the pH around an AC particle electrode through time at a current of -43 mA/g (-32 mA/cm^2) in the absence of flow and rising bubbles, as recorded with our FLIM setup. The region with increased pH marks the diffusion boundary layer. f) Modeled electric field lines and resulting local current density in the electrolyte (j_L) around a spherical particle electrode in a similar flow channel. The asymmetry of the system results in a stronger electric field at the right side of the particle electrode, with a higher ion flux in that region. Fo is the dimensionless Fourier number defined by eq. 5.1.

performed over 360 rays in total. A more thorough explanation on the ray casting and data processing is provided in section 5.5 of the SI.

As a result, we can monitor the diffusion boundary layer thickness along any ray over time. The results are shown in Figure 5.3c for rays B, C, and D (solid lines), and the mirrored counterparts B', and D' (dashed lines). C' is not included because of interference by the needle placement. The larger diffusion boundary layer thickness along rays B, C, and D compared to the mirrored counterparts B' and D' confirms that the development of the diffusion boundary layer around the particle is asymmetrical and depends on the location relative to the anode. During this experiment without electrolyte flow, the diffusion boundary layer thickness is eventually limited by the size of the channel. It reaches as far as the membrane along rays C and D after approximately 90 s, as can be seen in Figure S5.8 in the SI, and cannot grow further as a result.

The boundary layer grows roughly sublinear for the first 50 seconds, when the channel walls are not limiting yet and $Fo < 0.08$. Although the boundary layer growth in this case is subject to mixed migration and diffusion transport in the asymmetric system, this duration is close to the timescale that would be expected from penetration theory ($Fo = 0.1$ at $t = 60 \text{ s}$).

The situation changes drastically when introducing flow. Introducing a mild upward flow (0.3 mm/s , $Re_p = 0.27$) significantly diminishes the diffusion boundary layer along the sides of the particle (Figure 5.4b) versus the previous case without convection (Figures 5.2 and 5.3). Instead of forming a thick pH gradient in the x-direction, most produced OH^- gets flushed upward to form a plume above the particle electrode (indicated with arrow 3 in Figure 5.4c). In addition, FLIM reveals OH^- accumulation near the membrane due to concentration polarization (arrow 1, Figure 5.4a), and H_2 bubble formation

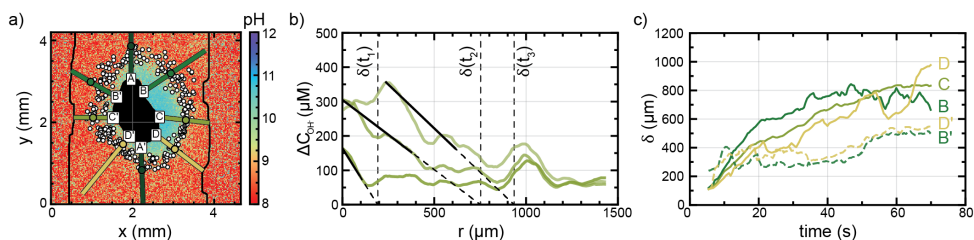


Figure 5.3: a) Colour map of the measured pH after 40 s of applying -43 mA/g (-32 mA/cm^2) without flowing the electrolyte. Rays are casted from the particle surface and the boundary layer thickness is estimated along each ray. Several rays (A, B, C, D) and their respective mirror images (A', B', C', and D') are shown with the edge of the diffusion boundary layer indicated with a coloured dot. The white dots indicate the estimated boundary layer thickness along all rays in between. b) Visualization of the boundary layer thickness (δ) along ray C (at $t_1 = 9 \text{ s}$, $t_2 = 50 \text{ s}$, and $t_3 = 68 \text{ s}$), by finding the x-intercept of the linearized $\Delta C_{\text{OH}^-}(r) = C_{\text{bulk}} - C(r)$ gradient near the particle. c) Development of the boundary layer thickness through time on rays B, C, and D, and the mirrored counterparts B' and D'.

5

is visible as well (arrow 2, Figure 5.4c).

In our system (HER), the plume signifies a region with increased pH, but more generally it indicates a region with altered reaction conditions. This can constitute anything from altered pH for proton-coupled electron transfer reactions, to reactant depletion for other reaction types. Ideally, the plume should be dissipated before the next active electrode section is reached, such as a strut in a porous (foam) electrode or a particle in a suspension electrode, to maintain a suitable reaction environment on the microscale. This is also important to prevent accumulation of changing conditions through the height of the electrode channel. For a porous electrode, this can result in a larger optimal pore size in the y-direction, and for suspension electrodes this can result in larger optimal spacing between the suspended particles.

To allow a 3D electrode with a large surface area (thus relatively small distance between the struts or particles) while minimizing plume effects, both the applied current density and flow velocity can be varied to reduce the size of the resulting plume. While higher current densities promote the plume formation and cause a steep pH gradient in the diffusion boundary layer (Figures 5.4a-c), higher flowrates help repress these effects (Figures 5.4d-f). Increasing the flow velocity diminishes the boundary layer and dissipates the plume at a shorter length scale, which in turn allows for smaller pores or loading more active particles in the same geometrical area and using them effectively. Because electrochemical conversions demand high current densities to improve their economic viability, enhancing mass transfer by raising the flow velocity is a more attractive strategy.

We analyze the effects of current density and flow velocity on the diffusion boundary layer thickness along several rays in Figures 5.5a and b, respectively. Although the diffusion boundary layer in Figures 5.4a-c becomes more visible with increasing current density, the diffusion boundary layer thickness is independent of the current density for relatively horizontal rays (ray C, Figure 5.5a). The higher visibility in Figure 5.4c is merely caused by a steeper pH gradient within the boundary layer, while the thickness is actually the same as in Figures 5.4a and b. This is in accordance with theory, which indicates

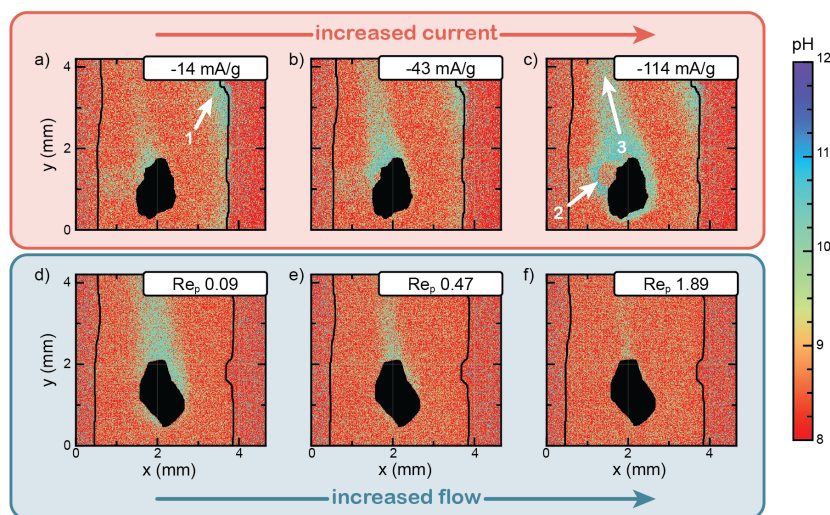


Figure 5.4: pH maps averaged over 20 images (20 s, 1 Hz) taken at steady state after 40 s of applying the relevant current density and flow velocity. The images show the influence of a-c) current density between -14 and -114 mA/g (-11 to -85 mA/cm²) at a constant flow velocity (0.3 mm/s) with $Re_p = 0.27$, and the influence of d-f) flow velocity (Re_p) at a constant applied current density of -15 mA/g on the boundary layer thickness and plume formation. The arrows indicate 1. OH⁻ accumulation near the membrane, 2. bubble formation, and 3. plume formation away from the membrane.

5

that the boundary layer thickness is determined by the Sherwood number (Sh), which is related to Re_p and independent of the current density.

The situation is different for ray A (Figure 5.5a), which points in the same direction as the flow. Here, the boundary layer thickness does show an increase with increasing current density. This is due to the larger amount of produced OH⁻ with increasing current density, which requires more mixing with bulk electrolyte to neutralize. This causes plume formation and a larger observed boundary layer.

As mentioned, we expect a decrease in boundary layer thickness with increasing Re_p in Figure 5.5b. This effect is slightly visible in two out of three analyzed regions (regions A and B), while the most horizontal region (region C) shows the opposite trend. This discrepancy is likely caused by the thin boundary layer with a relatively small OH⁻ concentration gradient inside it, or by the shape of the particle inducing a sideways electrolyte flow that carries OH⁻ ions in this direction. This combination makes our analysis less accurate, while the analysis in regions A and B is aided by the larger change in OH⁻ concentration. This effect should be more clearly present when operating at a higher current density.

We plot the pH close to the particle surface (average of the 5 first pixels on a ray) against the diffusion layer thickness in Figure 5.5c to illustrate the different local reaction conditions that can be obtained for the conversion reaction by adjusting the applied current density and electrolyte flow velocity. Increasing the current clearly raises the surface pH, while increasing the flow decreases the diffusion boundary layer thickness and accelerates mass transfer from the bulk. We can use these observations to steer the

local reaction conditions with current density and flow velocity.

Most electrochemical reactions benefit from fast mass transfer and an unaltered surface pH compared to the bulk, which corresponds to the region at the left bottom of Figure 5.5c. However, other reactions may benefit from a slightly elevated pH or concentration of product close to the catalyst surface (left upper region in Figure 5.5c), such as CO₂ reduction to higher carbon products (*i.e.*, in which the produced CO is converted to form C₂₊ products in a second step).[39, 40] In contrast, other reactions require a stable pH throughout the electrolyte to favor the desired reaction or to prevent detrimental effects on the catalyst (lower region of Figure 5.5c).[41] The current density and flow velocity, in combination with buffering electrolytes, can be used to steer the local environment towards the lower/upper region, or to the left/right side of the plot to achieve the optimum local reaction conditions.

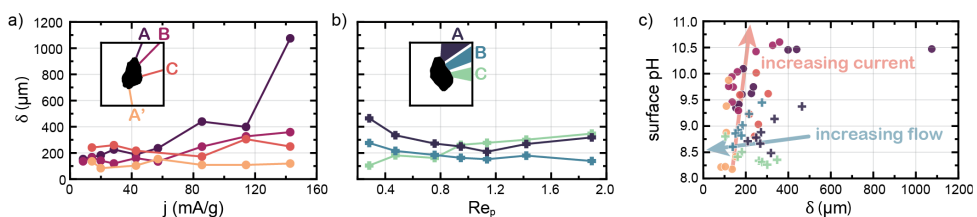


Figure 5.5: Influence of a) current density (j) at a constant flow velocity of 0.3 mm/s ($Re_p = 0.27$), and b) the influence of flow velocity (Re_p) at a constant current density of -15 mA/g (-11 mA/cm²) on the diffusion boundary layer thickness (δ) along various radial directions around a particle electrode. c) Shifts in δ and surface pH as a result of changing j and Re_p . For horizontal rays, raising the current density increases the surface pH with only a small effect on δ , while increasing the flow velocity decreases the δ at a mainly constant surface pH. For vertical rays, the δ and surface pH are also affected when increasing the current density and flow velocity, respectively.

5.3.2. CONCENTRATION PROFILE NEAR THE PARTICLE

In more detail, we observe that the highest OH⁻ concentration is often not located at the electrode surface, but is located 100-200 μm away from the electrode surface instead (Figure 5.3b). We constructed a simple model with a spherical particle electrode in COMSOL (Figures 5.6d-f, see section 5.5 in the SI for model details) to verify that our observations are not caused by artefacts of the experimental method.

The 3D character of the cathode and the asymmetry imposed by the system geometry (*i.e.* anode on only one side) alter the concentration profile inside the diffusion boundary layer in two ways. First, the OH⁻ concentration on the left is considerably higher than on the side of the particle that is facing the anode, because of the electric field pulling the OH⁻ ions to the anode side of the channel. This compresses and concentrates the boundary layer on the left side, while it stretches and dilutes the diffusion layer on the anode side of the particle. This matches our previous observations of asymmetry. Secondly, the observed OH⁻ concentration profile on the anode-facing side of the particle deviates from the linear profile that would be expected at a planar electrode from Fick's law. Instead, the OH⁻ concentration peaks further inside the diffusion boundary layer, as shown in Figure 5.6b. This peak was observed in every experiment, as well as in the

model (bottom row, Figure 5.6) and is thus not caused by FLIM artefacts or the particle shape.

Increasing the current density raises the peak height in both the experiments and the model, and shifts its location slightly away from the particle in the experimental results (Figure 5.6b), which is also subtly observed in the simulations (Figure 5.6e). We suspect that this is caused by the increase in electric field strength, which accelerates migration. Furthermore, the peak shifts towards the particle and decreases slightly in height when increasing the flow velocity (Figures 5.6c and f). In summary, the peak height is determined mainly by the current density through the OH^- production rate, while the peak location depends on the electric field strength through the migration velocity and on the flow velocity.

From these observations, we conclude that the peak is caused by OH^- that is produced at the bottom of the particle and flushed upwards along the curve of the particle electrode. More generally, the flow along a particle or an element of a 3D electrode will cause a convolution of concentration profiles produced upstream. The concentration profile observed at any location in the channel higher than the bottom of the particle will be an overlay of a series of gradients between the gradient caused by production at the observation height (which will have a high surface concentration and linear decrease to the bulk concentration) and the concentration gradient of all OH^- that is produced lower on the particle and flushed upwards. The current density controls how much OH^- is produced, but also determines the field strength, *i.e.* how fast the produced OH^- migrates to the right, and the flow velocity regulates how fast the OH^- is flushed upward and how much time it gets to migrate sideways before reaching the horizontal plane along which the profiles are recorded.

Hence, we conclude that this type of concentration profile is intrinsic for any non-planar electrode in flow, such as a flow-through (foam) and even in suspension electrodes, as the suspension particles also have a non-zero velocity relative to the electrolyte because of their difference in density with the electrolyte.

5.3.3. CAPACITANCE-DRIVEN FARADAIC REACTIONS

In this section, we investigate how long the capacitance of the particle's large microscopic surface area can maintain an ongoing Faradaic reaction after contact with the current source is broken, which is of interest for suspension electrodes. We apply a constant potential to drive the HER and charge the electric double layer (EDL) during an "on" phase, and switch to the Open Circuit Potential (OCP) during an "off" phase after 3 minutes. We continue measuring the particle potential (Figure 5.7a) and the surface pH (Figure 5.7b) while the particle electrode discharges. Because the HER can be sustained as long as the particle potential is more negative than E_{HER}^{eq} , we derived the HER equilibrium potential (E_{HER}^{eq}) in real-time from the surface pH obtained with FLIM. Although the surface pH differs significantly during the "on" - and "off" phases, the E_{HER}^{eq} increases by less than 0.1 V (comparing the highest surface pH of 9 to the starting pH of 7.3). The complete range of calculated E_{HER}^{eq} values are indicated as a grey band in Figure 5.7a. The HER can continue as long as the particle potential is more negative than this limit. In addition, the particle can perform the ORR as long as dissolved oxygen is present in the electrolyte because the E_{ORR}^{eq} lies 1.23 V above the E_{HER}^{eq} . [33, 42] We performed the

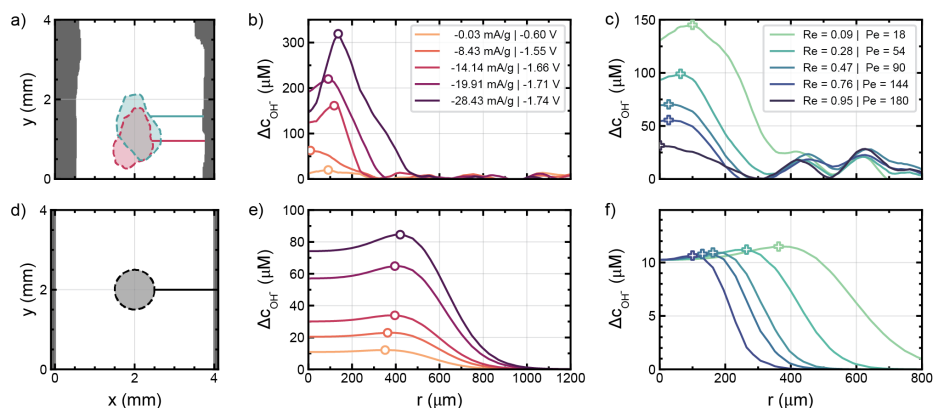


Figure 5.6: Visualization of the OH^- concentration profiles in the experiments (top row) and model (bottom row) with markers indication the locations of the peak OH^- concentrations. Panels a) and d) show the shape of the particle used in each experiment (pink for the current density series, green for the flow velocity series, spherical in all simulations), and the horizontal plane next to the particle electrode along which the OH^- concentration profiles are plotted. Panels b) and e) show the influence of current density, and panels c) and f) show the influence of flow velocity.

5

experiment at various charging potentials between -0.7 and -2.0 V vs SHE and we assess the influence of the charging potential on the surface pH and potential change over time in Figure 5.7.

The surface pH (Figure 5.7b) during charging increases with the charging potential because of the higher production rate of OH^- , and decays to the initial pH during the “off” phase as the produced OH^- ions are flushed away. However, the pH decay does not start immediately after switching to OCP and is always delayed by 5-10 s. It is hard to say whether this is caused by continued HER and ORR driven by the EDL capacitance, or by slow OH^- -removal along the particle exterior. The cases that were charged at -1.7 and -2.0 V vs SHE show a significant peak in pH 10 s after switching to OCP. This peak is caused by the removal of bubbles, which interfere with the FLIM signal.

The negative potential on the particle decays in two stages during the “off” stage in all cases (Figure 5.7a). The first jump occurs almost instantly after switching to OCP, while the 2nd stage is significantly slower. The initial and fast potential change is caused by the sudden removal of Ohmic resistances when switching to OCP, whereas the subsequent gradual potential change is related to discharging the capacitive EDL. Changing the preceding charging potential alters the shape of the discharge curve in two ways: 1) The capacitive discharge after switching to OCP (between 0-120 s) is faster for small negative charging potentials than for large negative potentials. This may be because the EDL is not an ideal capacitor and the $Q(V)$ relation is not linear, resulting in a lower capacitance and steeper potential change with the dissipation of charges.[43] And 2) the graphs show discharge towards different values in two clusters, with those charged at -1.7 and -2.0 V vs SHE approaching a more negative potential than those charged at -0.7 , -1.0 , and -1.4 V vs SHE, which quickly cross the equilibrium potential for HER. We suspect that this is determined by which reaction is performed on the particle. The potential in the three

upper graphs (charged at -0.7, -1.0, and -1.4 V vs SHE) is likely too small for the HER. In that case, ORR is the only Faradaic reaction that can occur. The potential on the two lower graphs (charged at -1.7 and -2.0 V vs SHE) is considerably larger and allows for both ORR and HER to occur simultaneously. Because the maximum O_2 concentration in water is only 1.1 mM, all available oxygen is instantly depleted at the electrode surface and hence, the discharge potential cannot surpass the HER limit for at least 120 s.

Regardless of which Faradaic reaction is occurring, we observe a continued discharge of the capacitive EDL after switching to OCP, during which sufficiently negative potentials to drive either the HER or the ORR are maintained for at least 2 minutes. This suggests that the particle capacitance can indeed sustain a Faradaic reaction for a while after contact with a current source is broken, albeit at a lower current density than when a potential is applied (deduced from the decreasing surface pH in Figure 5.7b). We will now assess the contributions of the different mechanisms and the timescales at which they occur in more detail.

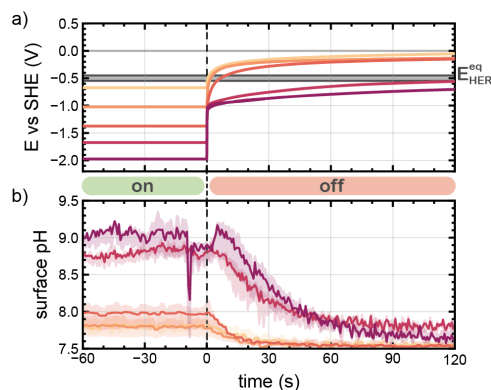


Figure 5.7: a) Particle potential during the charging (“on” phase) at various potentials and after switching to Open Circuit Potential (OCP) (“off” phase), and the range of HER equilibrium potentials (E_{HER}^{eq}) calculated from the particle surface pH. b) Particle surface pH during the experiment, as obtained with FLIM.

We study the potential curves further because the pH profiles (Figure 5.7b) do not distinguish between slow OH^- removal by flushing or continued OH^- production through HER driven by the EDL capacitance as the possible causes for the delayed pH decay in the FLIM results after ending the “on” phase.

Self-discharge of EDL capacitors (EDLCs) is known to occur through Faradaic reactions, charge redistribution, and current leakage. First of all, Faradaic reactions can take place whenever the potential on the electrode is sufficient to cause electron transfer for a redox reaction. The electron transfer from the electrode is accompanied by the release of ions from the EDL and a loss of cell voltage.[44] Secondly, charge redistribution is caused by a difference in charging speed between different parts of the electrode due to differences in resistance. For example, the outer surface area is easier to access for ions in solution than internal structures such as pores, which leads to faster charging of the EDL on the outer surface area. Ultimately, this results in an uneven distribution of charges throughout the material and a larger potential at the outer surface, where the

potential is measured.[44, 45] Upon switching to the “off” phase, the measured potential becomes smaller as the charges slowly redistribute to achieve an even charge distribution throughout the material. Finally, current leakage is a common problem when the capacitor electrodes are separated by a membrane or porous separator. Such separators allow for ion transfer between the compartments, effectively creating yet another discharge pathway.[31, 44]

Combining these three mechanisms, the self-discharge of an EDLC through these processes can be described by[36]

$$\Delta E = a\left(1 - e^{-\frac{t}{\tau}}\right) + b \ln(t) + c\sqrt{t} \quad (5.3)$$

in which ΔE is the change in potential compared to the “on” phase, t is the time after switching off the potential control, τ is a characteristic time constant, and a , b , and c are constants. The first term describes the potential loss due to electrolytic current leakage and ohmic resistances, the second term corresponds to the Faradaic contribution, and the third term is related to diffusion-controlled processes, which includes diffusion-limited Faradaic reactions and charge redistribution.[36] We obtained the total discharge contributions of these three terms over time by fitting the discharge curves to the equation.

The first term, related to current leakage and ohmic resistances, causes the potential jump upon switching off the potential control (at $t = 0$), due to nullifying the current (i) in Ohm’s law ($E = iR$). The data fitting shows that the current leakage is significantly smaller than the ohmic drop, causing the grey area in Figure 5.8 a-c to remain constant over time. The contributions of other self-discharge mechanisms are highly dependent on the charging potential. The purely Faradaic contribution decreases visibly with increasingly negative charging potentials of -1.4, -1.7, and -2.0 V vs SHE (Figure 5.8 a-c). Charge redistribution and mass transfer limitations in the Faradaic charge transfer gain importance at these larger applied potentials and currents, causing the discharging behavior to become more diffusion-controlled. For less negative charging potentials (-0.7 and -1.0 V vs SHE), the Faradaic contribution is smaller than that for -1.4 V vs SHE.

To understand why the Faradaic contribution peaks at -1.4 V vs SHE, and is smaller for both larger and smaller charging potentials, we translate the contributions to ΔE into a current density. Assuming ideal capacity behavior (*i.e.* constant capacitance), the slope $\frac{d\Delta E}{dt}$ is proportional to the current density for each mechanism. Hence, the slopes of the Faradaic charge transfer and diffusion-controlled discharge curves (Figure 5.8 d-e) give an indication of the intensity and timescale at which each mechanism occurs. The purely Faradaic potential change is the fastest and it is maintained longest (>20 s) after charging at -1.4 V vs SHE. The estimated discharge current that is entirely Faradaic is smaller and ceases within a few seconds when charging at a larger (-1.7 and -2.0 V vs SHE) or smaller (-0.7 and -1.0 V vs SHE) potentials (Figure 5.8d). This difference may be caused by either 1) a smaller overpotential (in the case of charging at -0.7 and -1.0 V vs SHE), or 2) depletion of oxygen (at -1.7 and -2.0 V vs SHE). For the large charging potentials (at -1.7 and -2.0 V vs SHE), oxygen may be depleted before and after switching off the potential control, which results in a high contribution for diffusion-controlled discharge instead. Alternatively, charge redistribution may play a substantial role at larger charging potentials. We cannot discriminate between these two effects, as both invoke a

shift towards diffusion-controlled discharge at the increasingly large charging potentials in Figure 5.8e.

Therefore, the charging potential should be optimized when using a suspension electrode for a Faradaic reaction. In this case, it is important for the capacitance of the porous particles to drive the reaction long enough to bridge their non-contact time with a current source. The applied potential should be large enough to provide sufficient overpotential and make the reaction last longer, but small enough to avoid significant diffusion limitations and charge redistribution. Ideally, charge redistribution can be suppressed by charging for a long time, and the current collector and suspension can be designed to shorten the non-contact time.

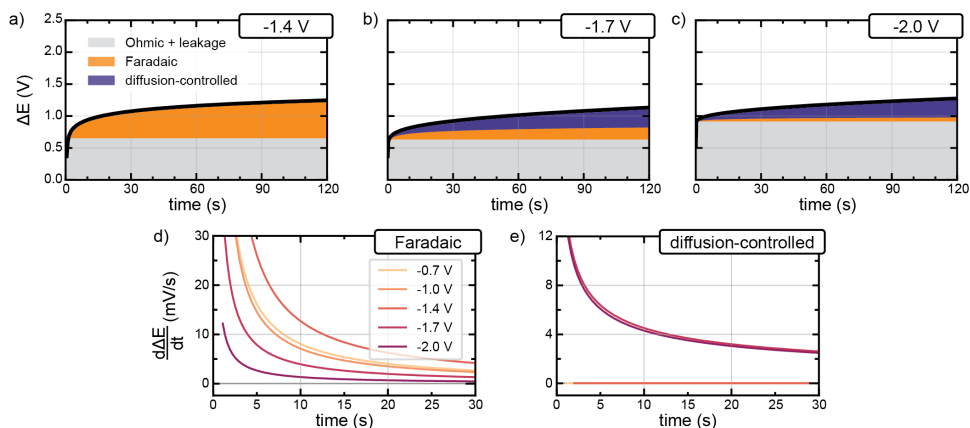


Figure 5.8: Panels a-c) show the contributions of the different discharge mechanisms on the potential change (ΔE) over time after charging at a) -1.4, b) -1.7, and c) -2.0 V vs SHE. The charging potential influences which discharge behavior is more dominant. Faradaic charge transfer dominates at small charging potential (-1.4 V vs SHE), and diffusion limitations that can also increase charge redistribution gain importance at larger charging potential (-2.0 V vs SHE). Panels d) and e) show the discharging rates $\frac{d\Delta E}{dt}$ attributed to purely Faradaic charge transfer (d) and diffusion-controlled processes (e).

5.4. CONCLUSIONS

Poor mass transfer at high operating current densities can cause an unfavorable local reaction environment near electrodes and affect selectivity and stability negatively in many electrochemical technologies. We studied the pH profiles around an activated carbon (AC) particle electrode, representing an element of a 3D electrode, during water electrolysis with FLIM. The obtained pH gradients give an estimate of the diffusion boundary layer thickness and the severity of plume formation, and indicate the extent of reactant depletion or product accumulation near the electrode.

The 3D character of the electrode and the asymmetry of the system lead to the formation of an asymmetrical diffusion boundary layer with an OH^- concentration profile that deviates from the linear profile known from planar electrodes. The OH^- gradient spanned over a thickness of 100–600 μm to the side, and a larger distance in the direction of applied electrolyte flow to create an OH^- -rich plume. We show that the bound-

ary layer thickness and plume size are most effectively decreased by an increase in flow velocity, while the surface pH is increased at higher current density. This implies that the 3D electrode design (*e.g.* pore size and shape) and flow velocity can be adapted to improve the reaction environment on the microscale, as well as on the macroscale by ensuring sufficient plume dissipation and preventing increased reagent depletion and product accumulation at the electrode surface or higher up in the electrode at required current densities.

Additionally, we investigated how long the capacitance of an AC particle can drive a Faradaic reaction after interrupting the potential control, by fitting the discharge curve to a self-discharge model for EDLCs. We conclude that our capacitive particle, representing a suspension electrode particle, can drive Faradaic reactions after interrupting the potential control, but probably drives ORR instead of HER in our case. We demonstrate that an optimum charging potential exists (in our case -1.4 V vs SHE) to provide sufficient overpotential, while avoiding the diffusion-limited regime and charge redistribution.

Overall, we conclude that FLIM is an excellent tool for studying hydrodynamics and local concentrations around 3D electrodes at high spatial and time resolution. Observations from FLIM can be used to design more effective electrodes adapting the morphology (pore size and shape, coverage by active particles) and flow conditions to mitigate negative effects caused by high current densities and plume formation to improve local reaction environments in a wide variety of applications.

5.5. SUPPORTING INFORMATION

The relevant data is available in the Zenodo repository at 10.5281/zenodo.12683345.

5.5.1 METHODS

5.5.1.1 EXPERIMENTAL

All experiments were performed in a transparent two-compartment PMMA electrochemical flow cell of which the design is shown in Figure S5.1a. An AC particle electrode (500-1000 μm , Norit 18x40 AG 1, average 200 μm diameter, Cabot) and Ni-foil are used as cathode and anode, respectively, with an Ag/AgCl reference electrode (LF-1-45, Alvatek). The AC particle electrode was made of an AC particle and sewing needle. The particle was attached to the tip of the needle with electrically conductive glue (Eccobond 56 C). The needle was coated with an acrylic layer to prevent contact with the electrolyte. A fluorescent dye (0.1 mM) is added to the catholyte (0.1 M K_2SO_4) as FLIM probe. The catholyte is separated from the anolyte (0.2 M KOH) by an Cation Exchange Membrane (CEM, Selemion CMV). The electrolytes are pumped through the cell at 0.1-2.1 mm/s in a single-pass mode by two syringe pumps as shown in Figure S5.1b. All electrochemical measurements are performed with a Vertex.100mA (± 100 mA/ ± 10 V, Ivium) potentiostat.

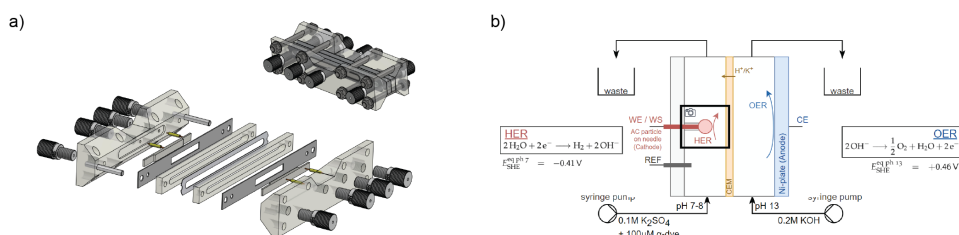


Figure S5.1: Illustrations of the a) FLIM flow cell and b) the setup used in the experiments. The needle with the AC particle attached is inserted through the WE/WS inlet in the backplate on the cathode side and replaces the cathode plate.

The flow cell was positioned in front of a light microscope (2.5x objective) equipped with a FLIM system (Figure S5.2). The FLIM system used a diode laser (405 nm, 20 MHz, 300 mW) as excitation source. The laser light is passed through an initial clean-up filter and spinning disc confocal imager (X-Light V2, Crest Optics) before illuminating the sample. The emitted light is directed by a dichroic mirror through an additional emission filter (cutoff at 420 nm) and onto a FLIM Toggel camera (512x470 pixels, Lambert Instruments).

The images are acquired with LIFA 1.4 software (Lambert Instruments) and are recorded at an exposure time of 34 ms and fitted to 6 phases. This results in a maximum FLIM image frequency of 2 Hz. The initial phase shift is set to 1500 and the multiplication gain to 8, resulting in 1000-6000 counts s^{-1} . All data is processed and analyzed further with a Python script that was developed in-house.

In FLIM, the fluorescence lifetime of a probe is used to study the local environment. The fluorescence lifetime of a probe can be dependent on various properties, such as pH or temperature. We use a quinolium-based dye with a fluorescence lifetime that is governed by the local pH through the protonation degree of the dye (double protonated H_2Q^{2+} , single protonated HQ^+ , and deprotonated Q).^[21, 35] The molecular structures and the used calibration curve, based on data from ref. [35], measured in cuvettes, are shown in Figure S5.3. An additional calibration measurement inside the flow channel is performed at the start of each experiment by filling the cell with a solution of pH 7-8 and setting the fluorescence lifetime to 12.6 ns. The fluorescence lifetime in

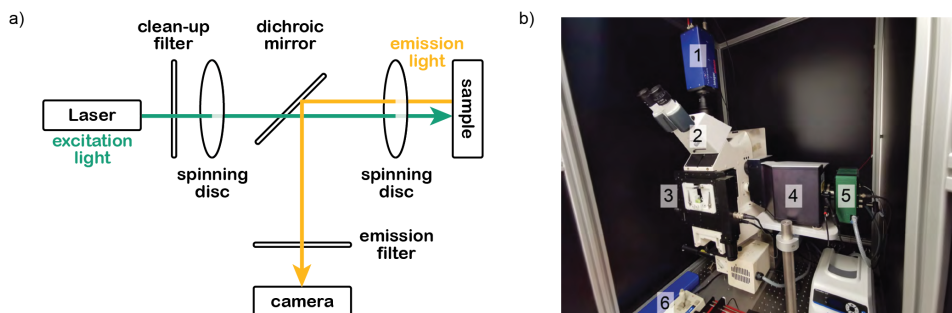


Figure S5.2: a) Diagram of the internal components, and excitation and emission light paths in the FLIM setup. b) Picture of the FLIM setup consisting of a (2) microscope, (3) sample holder, (4) confocal imager with spinning disc, (5) FLIM toggle camera, objects (1) and (6) are not used in FLIM mode.

each pixel is directly exported from LIFA and can be combined with the calibration curve in Figure S5.3 to calculate the local pH.

5

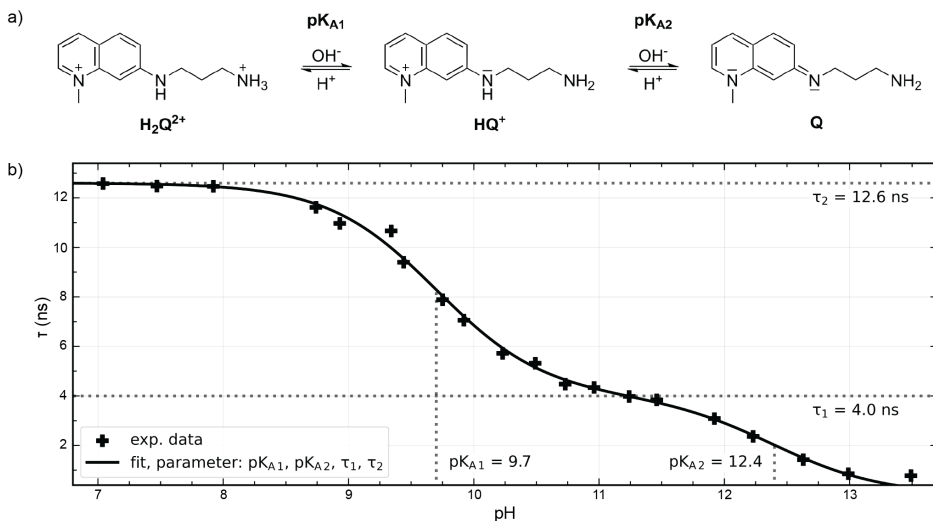


Figure S5.3: a) Molecular structure of the quinolium-based fluorescent dye in the double protonated (H_2Q^{2+}), single protonated (HQ^+), and deprotonated (Q) forms. b) Calibration curve showing the pK_{A1} and pK_{A2} , where the H_2Q^{2+}/HQ^+ and HQ^+/Q equilibria shift, determined from the sudden decrease in fluorescence lifetime (τ) with changing pH. Panel b is plotted with data from ref. [35].

5.5.1.2 IMAGE ANALYSIS

To perform radial analysis, the shape of the particle is extracted from the images with *scikit-image*, *opencv*, and *shapely* (all Python packages), and 360 rays are cast from the particle exterior, starting from these evenly spaced points on the shape edge. To prevent the rays of crossing and crowding in certain areas, the rays are not placed perfectly along the normal vector of the starting point, but the angle is modified with

$$\Theta_{ray} = \frac{\Theta_{normal} + f_p \cdot \Theta_{target}}{1 + f_p} \quad (S5.1)$$

in which Θ_{normal} is the normal angle, Θ_{target} is the target angle that is the ideal angle to achieve even spacing of the rays, f_p is a pulling factor, and Θ_{ray} is the resulting ray angle. A pulling factor of $f_p = 5$ was found to give a reasonably evenly spaced collection of rays. The placement of the starting points and effect of ray pulling are demonstrated in Figure S5.4.

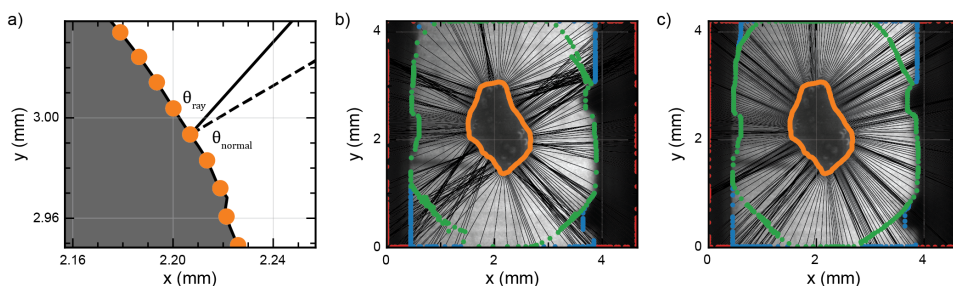


Figure S5.4: Demonstration of ray casting and pulling to achieve a decently even distribution of radial lines. a) Starting points placed on the particle edge and the projected normal vector (Θ_{normal} , dashed line) and the final ray (Θ_{ray} , solid line) obtained from pulling towards the target ray. Panels b) and c) show the collection of casted rays before and after pulling, respectively.

This allows us to study the pH along all rays. The recorded pH along a single ray in a single image is shown in Figure S5.5a. The data is averaged spatially with a moving average along 11 pixels and temporally over 20 images (20 s) to remove excessive noise in the experiments where the system is studied in steady state (i.e. the current and flow series). The temporal averaging is reduced to only 3 images (1.5 s) in the experiments where we are studying transient changes (i.e. the time series). Figure S5.5b shows the result of smoothing the data in panel a, the shaded areas indicate the standard deviations. The recorded local pH is used to calculate the difference between the local and the bulk hydroxide (OH^-) concentration (Figure S5.5c). Next, the boundary layer thickness can be estimated by converting the OH^- concentration and radius to dimensionless concentration (C^*) and dimensionless radius (r^*) by scaling with the maximum concentration and the particle radius, respectively (Figure S5.5d), and finally fitting a straight line from the peak to where ΔC^* drops below 40% of the peak concentration, and extrapolating it to the x-intercept (Figure S5.5e). This is in line with the common consensus that the diffusion boundary layer ends where the concentration approaches that of the bulk.

5.5.1.3 MODELLING

A simple model of OH^- concentration gradients around a spherical particle inside a 2D flow channel was created in COMSOL Multiphysics 6.1 for comparison with our experimental results. A schematic explaining the model and boundary conditions is shown in Figure S5.6. The modelled channel has a height H_{model} , and a width W . The spherical particle has a radius R_p and is placed with its center at a height of $5R_p$ in the middle of the channel. The following simplifications are applied:

- The Faradaic reaction is derived from the electric current
- Electrolyte electroneutrality is conserved by a mock counter-ion
- The electric current is decoupled from the electric potential

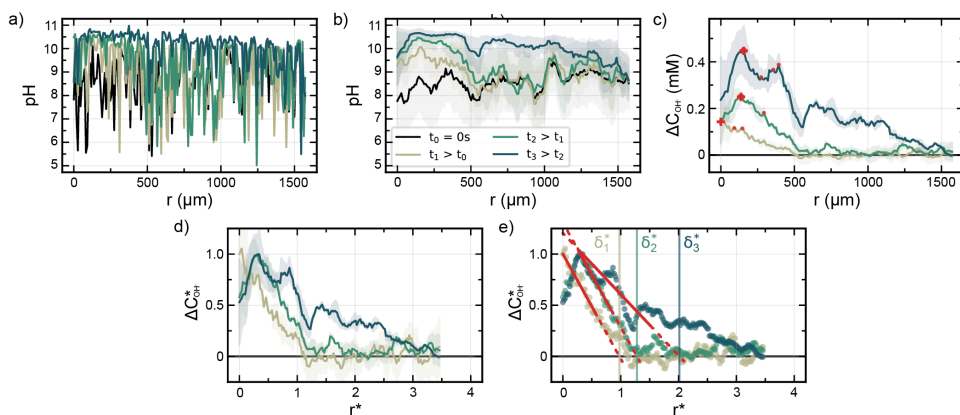


Figure S5.5: Steps in data processing for radial analysis. Starting from a) the pH along one ray in a single image, and b) smoothing data by spatial and temporal averaging. The shaded regions represent the standard deviation. c) Same result converted from local pH to OH^- concentration. The diffusion boundary layer thickness is then estimated by d) scaling the local OH^- concentration and radial distance to obtain the dimensionless concentration (C^*) and radius (r^*), e) fitting and extrapolating the linear region to find the diffusion boundary layer thickness (δ) at the x-intercept.

5

- No bubble formation

The fluid flow field is obtained by solving the Navier-Stokes equation for an incompressible fluid, with the following momentum boundary conditions:

- No slip condition on channel walls and particle
- Entering fluid has a fully developed laminar flow
- $P = 0$ at the outlet

The electric field is modelled with the 2D secondary current distribution interface. The Nernst-Planck equation is solved under electroneutrality and conservation of current conditions.

The mass balance of the dissolved ions is solved by inserting the Nernst-Planck equation with the previously obtained flow field and electrical field. A no-flux condition is imposed on the sides of the channel, the outlet is defined as region with only convection (no diffusion), the OH^- concentration at the inlet is defined by a pH of 7, and the OH^- production at the particle surface is obtained from the Faradaic reaction.

5.5.2 RESULTS

5.5.2.1 INFLUENCES ON DIFFUSION BOUNDARY LAYER

We monitored the pH gradient around the particle electrode under influence of three variables: time, current density, and electrolyte flow. The timeseries (Figure S5.7) was recorded without flowing the electrolyte, and at a low current density (-43 mA/g, corresponding to -32 mA/cm²) to prevent bubble-induced convection. We investigated the influence of current density at constant flow velocity of 0.3 mm/s with $Re_p = 0.27$, at current densities between 0 and -143 mA/g (-106 mA/cm²) (Figure S5.8). The influence of flow velocity is shown in Figure S5.9, and was studied at a constant current density of -15 mA/g (-11 mA/cm²). The particle's Péclet number is indicated for each flow velocity in Figures S5.11 and S5.12, and is defined here as $Pe_p = vd_p/D_{\text{OH}^-}$. [38] The

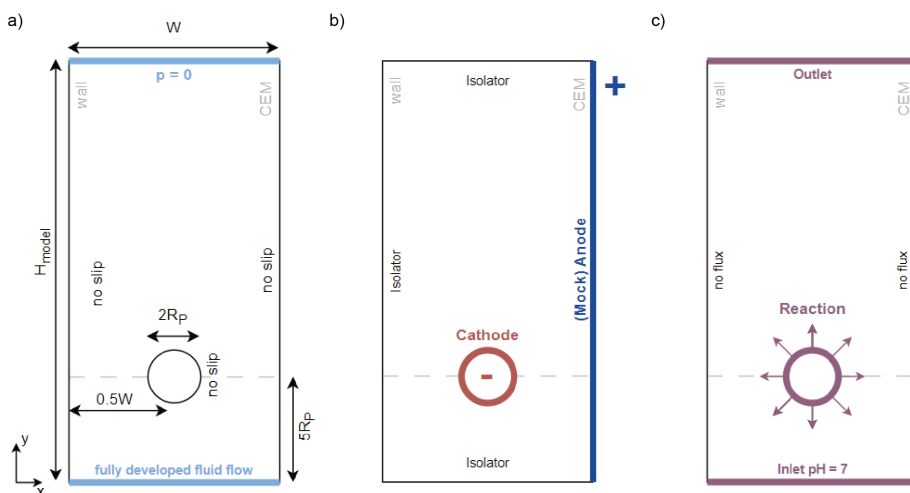


Figure S5.6: Diagram of the parameters and boundary conditions of the COMSOL model, showing a) the physical dimensions and momentum boundary conditions, b) charge boundary conditions, and c) species boundary conditions.

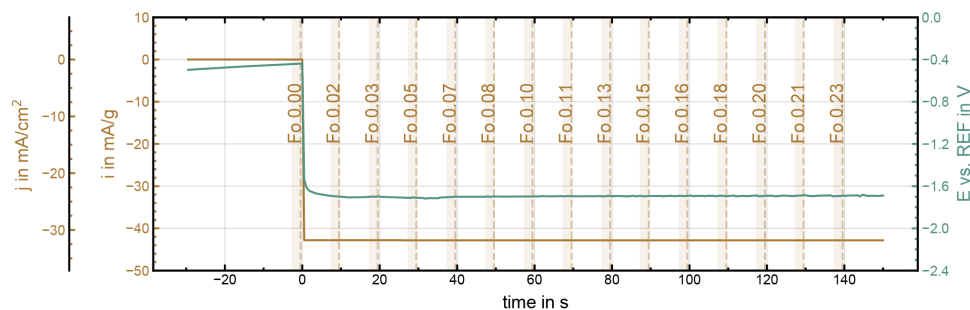


Figure S5.7: Applied current (orange) and resulting voltage (green) during transient recording of boundary layer formation and growth without flowing electrolyte. FLIM images were recorded with a frequency of 2 Hz and a moving average over 3 images was used to minimize noise. The orange shaded areas indicate the images that were averaged to obtain the time series in Figure S5.8 at the indicated Fourier (Fo) numbers.

images shown in the latter two series are recorded after the pH profile had developed completely and steady state had been reached.

A peak in OH^- concentration was observed away from the particle surface in all experiments. Figure S5.13 (top row) shows the difference with the bulk concentration on the right side of the particle along a horizontal plane in the middle of the particle for the experimental current (left), transient (middle), and flow series (right). These variables influence the peak height and location quite clearly (Figure S5.13, bottom row). The peak increases in height and shifts away from the particle with increasing current density and through time, while the peak decreases in height and shifts closer to the particle with increasing flow.

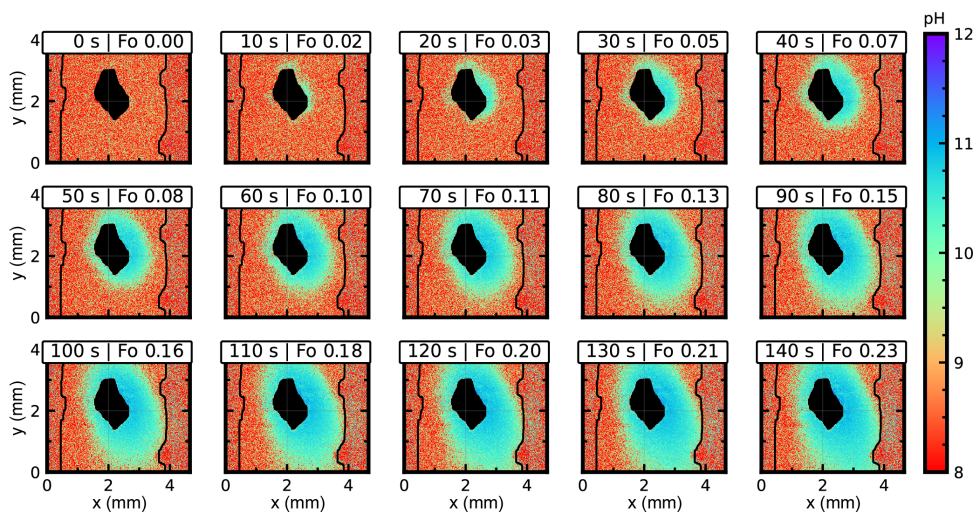


Figure S5.8: FLIM images of the pH profile through time and at the indicated Fo numbers, at a current of -43 mA/g (-32 mA/cm^2), without flow. Each result is obtained by averaging three FLIM images as previously indicated in Figure S5.7.

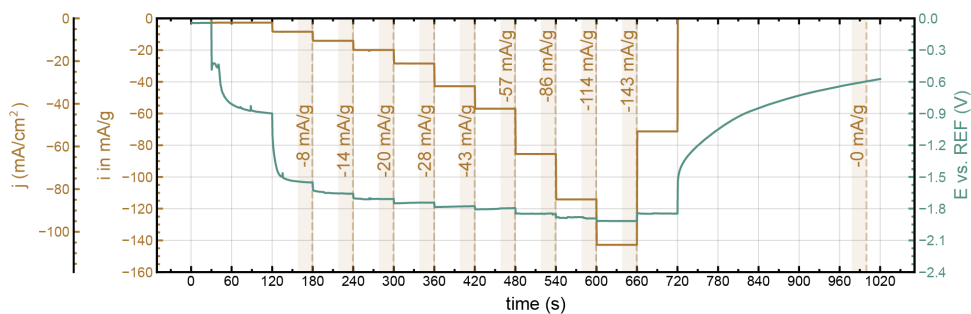


Figure S5.9: Applied current (orange) and resulting voltage (green) during FLIM of the single particle electrode at various current densities up to -143 mA/g (-106 mA/cm^2) at a constant flow velocity of 0.3 mm/s . FLIM images were recorded with a frequency of 1 Hz . Each current density was applied for 60 s and the FLIM recordings over the final 20 s (orange shaded areas) were averaged to obtain the images in Figure S5.10.

5.5.2.2 MECHANISM CONTRIBUTIONS DURING SELF-DISCHARGE

We mimicked the disconnection of a suspension particle from its current source by charging the EDL at a constant potential (“on” phase) and allowing the particle to discharge under Open Circuit Potential (OCP) (“off” phase). Figure S5.14 shows the contributions of the discharge mechanisms on the transient potential change for the tested charging potentials. Repeating the charge-discharge cycle influences the discharge contributions. In addition to the charging potential, as demonstrated in the manuscript, the mechanism contributions are also affected by changes in charging duration and cycling. [46] This is also observed in our system in Figure S5.15, which shows the discharge mechanism contributions after a second charging run of 30 s at the same charging potentials. At high charging potentials (-1.7 and -2.0 V vs SHE), the Faradaic contribution is increased in the second compared to the first charge-discharge cycle at the expense of charge redis-

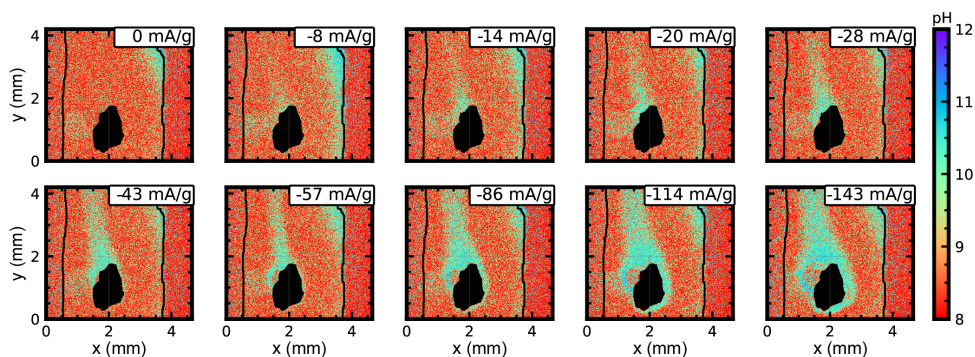


Figure S5.10: pH profiles around the single particle electrode after a steady state has been reached at various current densities, at a constant flow velocity of 0.3 mm/s with $Re_p = 0.27$. The indicated current densities were applied for 60 s, of which the FLIM recordings over the final 20 s were averaged, as indicated in Figure S5.9.

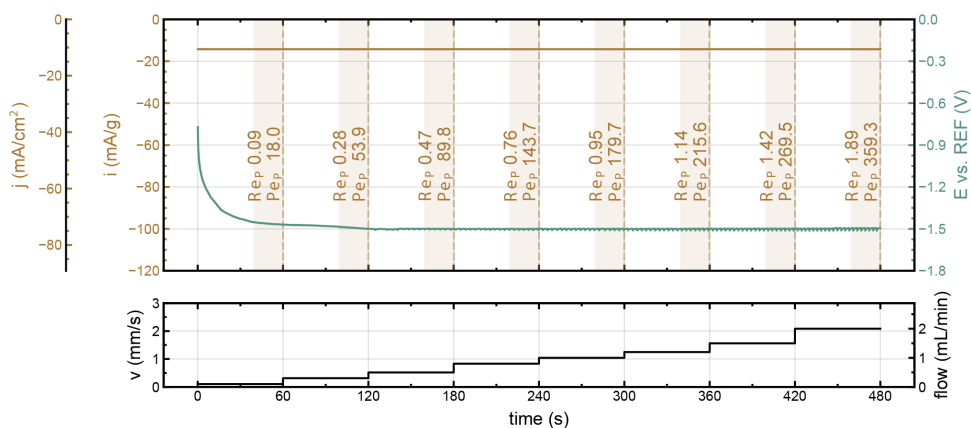


Figure S5.11: Applied current (orange, top panel) and resulting voltage (green, top panel) during FLIM of the single particle electrode at various flow velocities (bottom panel), at a constant current densities of -15 mA/g (-11 mA/cm²). FLIM images were recorded with a frequency of 1 Hz. Each flow velocity was applied for 60 s and the FLIM recordings over the final 20 s (orange shaded areas) were averaged to obtain the images in Figure S5.12 at the indicated Péclet (Pe_p) numbers.

tribution. The same effect can be seen in Figure S5.16, which shows the fractional contributions of the Faradaic reaction and charge redistribution during the first 30 s of the “off” phase in the first (solid lines) and second (dashed lines) cycles.

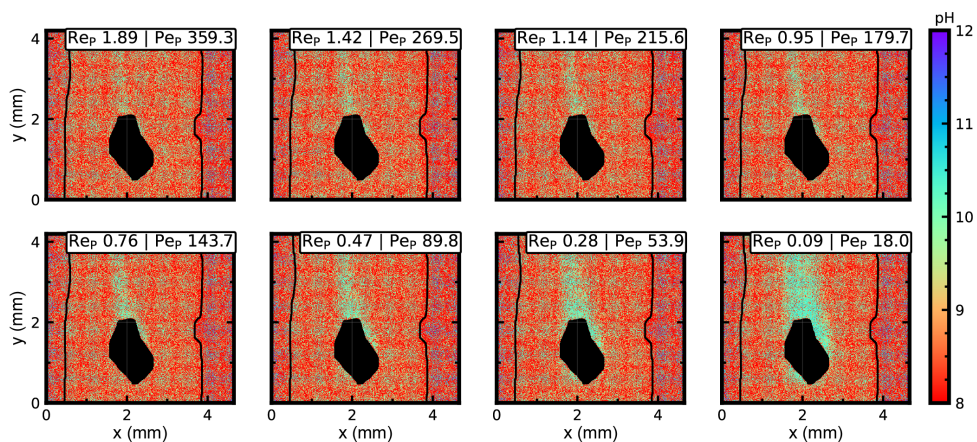


Figure S5.12: pH profiles around the single particle electrode after a steady state has been reached at various flow velocities (0.1-2.1 mm/s) and corresponding Reynolds numbers (Re_p 0.1-1.9), at a constant current density of -15 mA/g (-11 mA/cm²). Each flow velocity was applied for 60 s and the FLIM recordings over the final 20 s were averaged, as indicated in Figure S5.11.

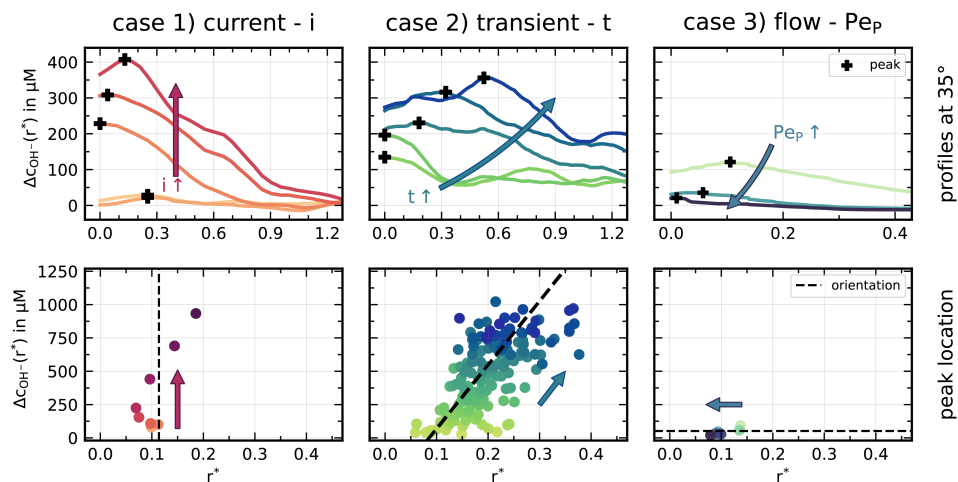


Figure S5.13: Influence of the current (left), time (middle), and flow (right) on the OH^- concentration peak location in the experimental results. The peak increases in height and shifts to the right (away from the particle surface) with increasing current and with time. The peak decreases in height and shifts to the left (towards the particle surface) with increased flow.

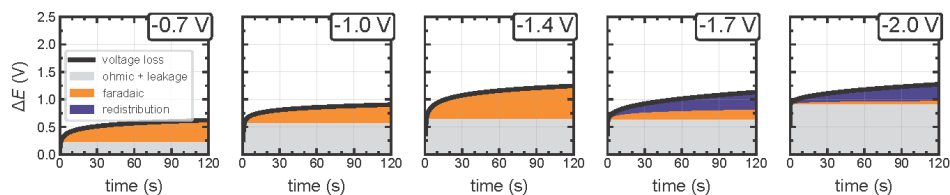


Figure S5.14: Contributions of the different discharge mechanisms to the potential change over time after charging at various potentials.

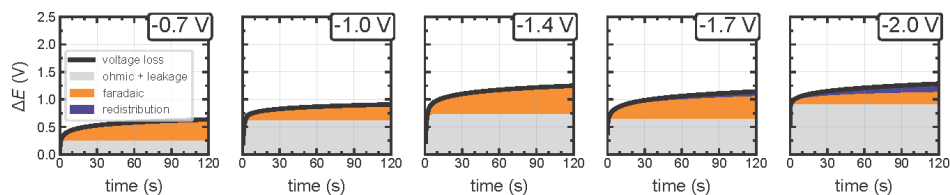


Figure S5.15: Contributions of the different discharge mechanisms during a second discharge run. The contribution of charge redistribution is clearly diminished and Faradaic charge transfer is more dominant than during the first discharge run.

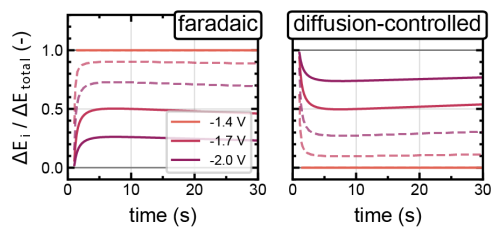


Figure S5.16: Visualization of the potential change fractions that can be attributed to Faradaic charge transfer and charge redistribution after charging at various charging potentials during the first (solid lines) and second (dashed lines) discharge runs. The Faradaic contribution is visibly enhanced, while the redistribution contribution is diminished accordingly.

REFERENCES

- [1] Gabriele Centi, Gaetano Iaquaniello, and Siglinda Perathoner. “Chemical engineering role in the use of renewable energy and alternative carbon sources in chemical production”. In: *BMC Chemical Engineering* 1.1 (2019), p. 5.
- [2] Geoffrey Hammond and Marcus Newborough. “Glasgow climate pact: a step on the way towards a lower carbon dioxide world”. In: *Proceedings of the Institution of Civil Engineers - Civil Engineering* 175.1 (2022), pp. 8–8.
- [3] Alexander Otto, Thomas Grube, Sebastian Schiebahn, and Detlef Stolten. “Closing the loop: captured CO₂ as a feedstock in the chemical industry”. In: *Energy & Environmental Science* 8.11 (2015), pp. 3283–3297.
- [4] Phil De Luna, Christopher Hahn, Drew Higgins, Shaffiq A. Jaffer, Thomas F. Jaramillo, and Edward H. Sargent. “What would it take for renewably powered electrosynthesis to displace petrochemical processes?” In: *Science* 364.6438 (2019), eaav3506.
- [5] Matthew Jouny, Wesley Luc, and Feng Jiao. “General Techno-Economic Analysis of CO₂ Electrolysis Systems”. In: *Industrial & Engineering Chemistry Research* 57.6 (2018), pp. 2165–2177.
- [6] Diya Agrawal, Navya Mahajan, Satyapaul A. Singh, and I. Sreedhar. “Green hydrogen production pathways for sustainable future with net zero emissions”. In: *Fuel* 359 (2024), p. 130131.
- [7] Sage Sebastian, Samantha Wijewardane, and Sessa Srinivasan. “Recent advances in hydrogen production, storage, and fuel cell Technologies with an emphasis on inventions, innovations, and commercialization”. In: *Solar Compass* 8 (2023), p. 100065.
- [8] Yoontaek Oh, Ji-Hyung Han, Hanki Kim, Namjo Jeong, David A. Vermaas, Jin-Soo Park, and Soryong Chae. “Active Control of Irreversible Faradic Reactions to Enhance the Performance of Reverse Electrodialysis for Energy Production from Salinity Gradients”. In: *Environmental Science & Technology* 55.16 (2021), pp. 11388–11396.
- [9] Hongning Chen, Yao Liu, Xuefeng Zhang, Quan Lan, Yue Chu, Yongliang Li, and Qixing Wu. “Single-component slurry based lithium-ion flow battery with 3D current collectors”. In: *Journal of Power Sources* 485 (2021), p. 229319.
- [10] Nicholas J. Matteucci, Christopher T. Mallia, Bertrand J. Neyhouse, Madhu V. Majji, and Fikile R. Brushett. “Toward electrochemical design principles of redox-mediated flow batteries”. In: *Current Opinion in Electrochemistry* 42 (2023), p. 101380.
- [11] David W. Keith, Geoffrey Holmes, David St. Angelo, and Kenton Heidel. “A Process for Capturing CO₂ from the Atmosphere”. In: *Joule* 2.8 (2018), pp. 1573–1594.
- [12] R. Sharifian, R. M. Wagterveld, I. A. Digdaya, C. Xiang, and D. A. Vermaas. “Electrochemical carbon dioxide capture to close the carbon cycle”. In: *Energy & Environmental Science* 14.2 (2021), pp. 781–814.
- [13] Carlos Alberto Martínez-Huitle and Marco Panizza. “Electrochemical oxidation of organic pollutants for wastewater treatment”. In: *Current Opinion in Electrochemistry* 11 (2018), pp. 62–71.

- [14] S. Porada, R. Zhao, A. van der Wal, V. Presser, and P. M. Biesheuvel. “Review on the science and technology of water desalination by capacitive deionization”. In: *Progress in Materials Science* 58.8 (2013), pp. 1388–1442.
- [15] M. E. Suss, S. Porada, X. Sun, P. M. Biesheuvel, J. Yoon, and V. Presser. “Water desalination via capacitive deionization: what is it and what can we expect from it?” In: *Energy & Environmental Science* 8.8 (2015), pp. 2296–2319.
- [16] Marjolein Vanoppen, Ella Criel, Griet Walpot, David A. Vermaas, and Arne Verliefe. “Assisted reverse electrodialysis—principles, mechanisms, and potential”. In: *npj Clean Water* 1.1 (2018), p. 9.
- [17] David M. Weekes, Danielle A. Salvatore, Angelica Reyes, Aoxue Huang, and Curtis P. Berlinguette. “Electrolytic CO₂ Reduction in a Flow Cell”. In: *Accounts of Chemical Research* 51.4 (2018), pp. 910–918.
- [18] Sahil Garg, Mengran Li, Adam Z. Weber, Lei Ge, Liye Li, Victor Rudolph, Guoxiong Wang, and Thomas E. Rufford. “Advances and challenges in electrochemical CO₂ reduction processes: an engineering and design perspective looking beyond new catalyst materials”. In: *Journal of Materials Chemistry A* 8.4 (2020), pp. 1511–1544.
- [19] Giulia Marcandalli, Mariana C. O. Monteiro, Akansha Goyal, and Marc T. M. Koper. “Electrolyte Effects on CO₂ Electrochemical Reduction to CO”. In: *Accounts of Chemical Research* 55.14 (2022), pp. 1900–1911.
- [20] Mariana C. O. Monteiro, Alex Mirabal, Leon Jacobse, Katharina Doblhoff-Dier, Scott Calabrese Barton, and Marc T. M. Koper. “Time-Resolved Local pH Measurements during CO₂ Reduction Using Scanning Electrochemical Microscopy: Buffering and Tip Effects”. In: *JACS Au* 1.11 (2021), pp. 1915–1924.
- [21] Lorenz M. Baumgartner, Aron Kahn, Maxime Hoogland, Jorrit Bleeker, Wolter F. Jager, and David A. Vermaas. “Direct imaging of local pH reveals bubble-induced mixing in a CO₂ electrolyzer”. In: *ACS Sustainable Chemistry & Engineering* 11.28 (2023), pp. 10430–10440.
- [22] J. W. Blake, J. T. Padding, and J. W. Haverkort. “Analytical modelling of CO₂ reduction in gas-diffusion electrode catalyst layers”. In: *Electrochimica Acta* 393 (2021), p. 138987.
- [23] Recep Kas, Andrew G. Star, Kailun Yang, Tim Van Cleve, Kenneth C. Neyerlin, and Wilson A. Smith. “Along the Channel Gradients Impact on the Spatioactivity of Gas Diffusion Electrodes at High Conversions during CO₂ Electroreduction”. In: *ACS Sustainable Chemistry & Engineering* 9.3 (2021), pp. 1286–1296.
- [24] Barun Kumar Chakrabarti, Evangelos Kalamaras, Abhishek Kumar Singh, Antonio Bertei, J. Rubio-Garcia, Vladimir Yufit, Kevin M. Tenny, Billy Wu, Farid Tariq, Yashar S. Hajimolana, Nigel P. Brandon, Chee Tong John Low, Edward P. L. Roberts, Yet-Ming Chiang, and Fikile R. Brushett. “Modelling of redox flow battery electrode processes at a range of length scales: a review”. In: *Sustainable Energy & Fuels* 4.11 (2020), pp. 5433–5468.
- [25] J. W. Haverkort. “A theoretical analysis of the optimal electrode thickness and porosity”. In: *Electrochimica Acta* 295 (2019), pp. 846–860.

- [26] M. S. Isaacson and Ain A. Sonin. "Sherwood Number and Friction Factor Correlations for Electrodialysis Systems, with Application to Process Optimization". In: *Industrial & Engineering Chemistry Process Design and Development* 15.2 (1976), pp. 313–321.
- [27] H. Rajaei, A. Rajora, and J. W. Haverkort. "Design of membraneless gas-evolving flow-through porous electrodes". In: *Journal of Power Sources* 491 (2021), p. 229364.
- [28] Alexandra Rommerskirchen, Anna Kalde, Christian J. Linnartz, Leon Bongers, Georg Linz, and Matthias Wessling. "Unraveling charge transport in carbon flow-electrodes: Performance prediction for desalination applications". In: *Carbon* 145 (2019), pp. 507–520.
- [29] Changyong Zhang, Jinxing Ma, Lei Wu, Jingyi Sun, Li Wang, Tianyu Li, and T. David Waite. "Flow Electrode Capacitive Deionization (FCDI): Recent Developments, Environmental Applications, and Future Perspectives". In: *Environmental Science & Technology* 55.8 (2021), pp. 4243–4267.
- [30] Monjur Mourshed, Seyed Mohammad Rezaei Niya, Ruchika Ojha, Gary Rosengarten, John Andrews, and Bahman Shabani. "Carbon-based slurry electrodes for energy storage and power supply systems". In: *Energy Storage Materials* 40 (2021), pp. 461–489.
- [31] Volker Presser, Christopher R. Dennison, Jonathan Campos, Kevin W. Knehr, Emin C. Kumbur, and Yury Gogotsi. "The Electrochemical Flow Capacitor: A New Concept for Rapid Energy Storage and Recovery". In: *Advanced Energy Materials* 2.7 (2012), pp. 895–902.
- [32] Lihi Amit, Danny Naar, Robert Gloukhovski, Gerardo Jose la O, and Matthew E. Suss. "A single-flow battery with multiphase flow". In: *ChemSusChem* 14.4 (2021), pp. 1068–1073.
- [33] C. Borsje, T. Sleutels, C. J. N. Buisman, and A. ter Heijne. "Improving the discharge of capacitive granules in a moving bed reactor". In: *Journal of Environmental Chemical Engineering* 9.4 (2021), p. 105556.
- [34] Alexandra Deeke, Tom H. J. A. Sleutels, Tim F. W. Donkers, Hubertus V. M. Hamelers, Cees J. N. Buisman, and Annemiek Ter Heijne. "Fluidized Capacitive Bioanode As a Novel Reactor Concept for the Microbial Fuel Cell". In: *Environmental Science & Technology* 49.3 (2015), pp. 1929–1935.
- [35] Jorrit Bleeker, Aron P. Kahn, Lorenz M. Baumgartner, Ferdinand C. Grozema, David A. Vermaas, and Wolter F. Jager. "Quinolinium-based fluorescent probes for dynamic pH monitoring in aqueous media at high pH using fluorescence lifetime imaging". In: *ACS Sensors* 8.5 (2023), pp. 2050–2059.
- [36] Andrzej Lewandowski, Pawel Jakobczyk, Maciej Galinski, and Marcin Biegun. "Self-discharge of electrochemical double layer capacitors". In: *Physical Chemistry Chemical Physics* 15.22 (2013), pp. 8692–8699.
- [37] Nathalie E. G. Ligthart, Gerard Prats Vergel, Johan T. Padding, and David A. Vermaas. "Practical potential of suspension electrodes for enhanced limiting currents in electrochemical CO₂ reduction". In: *Energy Advances* 3.4 (2024), pp. 841–853.

- [38] Matthias Kraume. *Transportvorgänge in der Verfahrenstechnik: Grundlagen und apparative Umsetzungen*. 3. Auflage. Springer Lehrbuch. Springer Vieweg, 2020. ISBN: 978-3-662-60012-2.
- [39] Gurudayal, David Perone, Saurabh Malani, Yanwei Lum, Sophia Haussener, and Joel W. Ager. “Sequential Cascade Electrocatalytic Conversion of Carbon Dioxide to C–C Coupled Products”. In: *ACS Applied Energy Materials* 2.6 (2019), pp. 4551–4559.
- [40] Xinyan Liu, Philomena Schlexer, Jianping Xiao, Yongfei Ji, Lei Wang, Robert B. Sandberg, Michael Tang, Kristopher S. Brown, Hongjie Peng, Stefan Ringe, Christopher Hahn, Thomas F. Jaramillo, Jens K. Nørskov, and Karen Chan. “pH effects on the electrochemical reduction of CO₍₂₎ towards C₂ products on stepped copper”. In: *Nature Communications* 10.1 (2019), p. 32.
- [41] Nitish Govindarajan, Aoni Xu, and Karen Chan. “How pH affects electrochemical processes”. In: *Science* 375.6579 (2022), pp. 379–380.
- [42] Alicia M. Oickle and Heather A. Andreas. “Examination of Water Electrolysis and Oxygen Reduction As Self-Discharge Mechanisms for Carbon-Based, Aqueous Electrolyte Electrochemical Capacitors”. In: *The Journal of Physical Chemistry C* 115.10 (2011), pp. 4283–4288.
- [43] A. A. Moya. “Nonlinear charge-voltage relationships in electric double layer capacitors performing under constant load resistance”. In: *Journal of Energy Storage* 71 (2023), p. 108136.
- [44] Heather A. Andreas. “Self-discharge in electrochemical capacitors: A perspective article”. In: *Journal of The Electrochemical Society* 162.5 (2015), A5047.
- [45] Heather A. Andreas, Jennifer M. Black, and Alicia A. Oickle. “Self-discharge in manganese oxide electrochemical capacitor electrodes in aqueous electrolytes with comparisons to Faradaic and charge redistribution models”. In: *Electrochimica Acta* 140 (2014), pp. 116–124.
- [46] Maximilian Kaus, Julia Kowal, and Dirk Uwe Sauer. “Modelling the effects of charge redistribution during self-discharge of supercapacitors”. In: *Electrochimica Acta* 55.25 (2010), pp. 7516–7523.

6

CONCLUSIONS

Intensification of electrochemical processes will be crucial in the transition towards a green and electrified industry, but is hampered by mass transfer limitations in aqueous electrochemical systems. In this thesis, we let go of the conventional methods for enhancing mass transfer, and instead we employ 3D volume-based electrodes to bring the catalyst to the reagent rather than relying on slow mass transport towards a planar electrode. We assess which strategies are suitable to expand the accessible electrolyte volume and increase the amount of available reagent.

We explored the possibilities and applicability of volume-based electrodes as an alternative approach for alleviating mass transfer limitations in robust and scalable systems. We studied two types of volume-based electrodes: a flow-through (foam-based) and a flow-with (suspension-based) configuration. While the flow-through configuration offers larger relative velocity between the electrode and electrolyte, as well as greater electrical conductivity, suspension electrodes offer easier bubble removal for gas-evolving conversions, and considerable capacitive features. We investigated which electrode properties should lead to an even reaction distribution across the entire electrolyte channel to give the best results in either 3D configuration (Ch. 2), considering the effective conductivity of the network and the stability of suspended catalytic material (Ch. 3). We studied the influence of electrode configuration on mass transfer on the microscale and assessed the limitations of volume-based electrodes in scaling aqueous systems (Ch. 4). Finally, we analyzed the development of the DBL and local concentration profiles around a single electrode element under different applied current densities and electrolyte flow velocities (Ch. 5). We used CO₂ and O₂ electrolyzers as representative diffusion-limited systems, and our finding can be extended to other mass transfer-limited processes.

We employed a large range of research methods, including a TLM and EIS to investigate the necessary electrical properties, and combined the data with rheology measurements to investigate the influence of particle properties in case of suspension electrodes. In addition, a large number of electrochemical experiments were performed as practical tests, and Sherwood correlations and microscopic imaging (FLIM) were used to study mass transfer and the influence on the local reaction environment. The latter was performed with HER as a proxy for any electrochemical reaction to produce a visible pH gradient.

The used TLM (Chapter 2) showed that the electrical properties are of great importance to control the distribution of the electrochemical reaction. We considered the various situations listed below with their corresponding results:

1. The charge transfer resistance (R_{ct}'') is dominant: this will give an even reaction distribution across the channel depth, regardless of the ratio between the solid (R'_S) and liquid (R'_L) phase resistances.
2. All three resistances are of similar magnitude: the R'_S/R'_L ratio gains importance and results in a higher current density closer to the current collector ($R'_S > R'_L$), or closer to the membrane ($R'_S < R'_L$).
3. The R_{ct}'' is significantly lower than R'_S and R'_L : this will always result in a localized reaction and eliminates the benefits of using a volume-based electrode.

Our measurements showed that the right conditions (situations 1 and 2) can be achieved with the dynamic conductive networks occurring in suspension electrodes, if a suitable particle type and volume fraction are selected. The solid phase conductivity should match the ionic conductivity, but is more challenging to enhance. The ionic conductivity can be increased to >100 mS/cm by raising the electrolyte concentration, while the solid phase conductivity is typically limited to 0.1-1 mS/cm because of the decreasing flowability with increasing particle loading.[1] Developing suspensions with better particle-particle contact and higher solid phase conductivity is therefore of great interest.

Although the TLM results show that several of the used suspensions possess sufficient solid phase conductivity and the correct properties to expect a homogeneous reaction distribution and good catalytic performance, the FE towards CO was unexpectedly low. The high activity towards HER shows that the large amount of suspended material needed to provide sufficient electrical conductivity and the enormous surface area the material carries lend the choice of microparticle material considerable importance. A wrong choice of suspended material has been shown to interfere negatively with the desired process in both the CO₂ reduction and the oxygen reduction experiments. The presence of metal contaminations and the immense amount of non-silver surface area seem to catalyze the HER during the CO₂ reduction experiments (Ch. 2), and the carbon material causes disproportionation of produced H₂O₂ during the ORR (Ch. 4). Therefore, great care should be taken to select particles with suitable chemical properties, in addition to favorable electrical properties, for each process. Ideally, the suspension would consist completely of material that catalyzes the intended reaction with good selectivity, offers high solid phase conductivity, and has a large specific surface area to provide large amount of catalytic sites and considerable capacitance.

As a foam can be interpreted as a network of solid elements that are permanently connected, incorporating a foam may be a pragmatic alternative that eliminates the contact resistance between the suspension particles. The static networks in foam-based electrodes result in a higher solid phase conductivity (approx. 3 S/cm) at very low solid volume fractions (typically <4%).[2, 3] Although a foam electrode lacks the movement of the electrode itself, the conditions in terms of resistance and resistance ratio should be feasible, and hence allow to realize high partial current densities in a flow-through configuration.

Replacing the carbon microparticles with a flow-through electrode indeed improved the CO current density significantly to >50 mA/cm² (Ch. 3) by providing a superior electrically conductive network, as well as removing the excessive carbon surface area and possible metal contaminations. These improved chemical properties eliminate the negative interferences observed in Chapters 2 and 4.

In addition, Chapter 3 reveals the importance of stabilizing agents when utilizing a suspension of catalytic material in electrolyte. Adding SDS significantly improved the CO current density by hindering particle aggregation and loss of catalytic surface area, and possibly improving bubble removal and protecting the Ag NP surfaces from degradation. Although the highest achieved current density of 56 mA/cm² is not yet close to the required 200 mA/cm², the initial results and insights

in this chapter are promising for optimization studies and should encourage further research into surfactant-assisted CO₂ reduction in aqueous flow-through electrolyzers. Especially the reaction location (*i.e.* deposited versus flowing Ag NPs) and the role of the surfactant (*i.e.* stabilization versus mass transfer enhancement) would be of interest.

Like CO₂ reduction, the ORR did not suffer from carbon-induced issues when the flow-through configuration was used, while it could still leverage the advantage of a large and easily accessible surface area with shortened mass transfer distances due to its porous nature. The electrode structure prevents the development of thick diffusion boundary layers and thereby raises the mass transfer coefficient and alleviates mass transfer limitations considerably, even at low flow velocities. The limiting current density showed a weaker dependence on flow velocity in the flow-through configuration than in the flow-by configuration, increases only slightly with increasing flow in the regime of low Reynolds numbers ($Re < 234$), and follows the expectations from Sherwood correlations nicely. As a result, employing a smart electrode configuration is more effective for alleviating mass transfer limitations than optimizing the flow velocity, at least in the range of flow rates relevant for electrochemical flow systems.

Although we have shown that mass transfer limitations on the microscale are alleviated in flow-through electrodes, the limitations on the macroscale are not and further system engineering will be necessary. Boosting the local current density results in significantly faster reagent consumption, which in turn leads to reagent depletion and a decreasing local current density (or product selectivity) along the length of the electrolyzer channel. This is especially severe for extremely poorly soluble reagents such as O₂ with a maximum concentration of 1.1 mM, versus CO₂ with a maximum concentration of 34 mM, under standard conditions. Therefore, the flow velocity should be adjusted to achieve a residence time that is suitable for the applied geometric current density and the consumption rate along the channel. So even though increasing the flow in the low Reynolds regime does not improve the mass transfer coefficient considerably, increasing the flow rate is necessary to improve the performance on the macroscale. Alternatively, one could investigate in-channel saturation methods similar to a gas-fed system, such as a bubble column or GDE, high-pressure electrolyzers[4], or shortening the path through the flow-through electrode by forcing the flow parallel to the current[5].

A more detailed study of the local pH around a single particle electrode using FLIM revealed the influence of the 3D character of an electrode on the shape of the DBL and the pH gradient inside it. The 3-dimensional shape of the particle electrode resulted in an asymmetrical DBL in both the horizontal and the vertical (plume formation) direction, with a pH gradient that differed from the linear gradient commonly known to form at planar electrodes. The regions with observed altered pH compared to the bulk indicate regions with reagent depletion and product accumulation. The extent of these regions and their influence on the local reaction environment (reagent availability and surface pH) should be considered during process design. The applied current density, flow velocity, and pore size and shape (in case of a flow-through electrode) or particle proximity and volume fraction (in case of a suspension electrode) can be adjusted to ensure the most favorable reaction conditions throughout the electrode.

Overall, we have shown that implementing volume-based electrodes can alleviate mass transfer limitations in various all-aqueous electrochemical conversion systems already at low electrolyte flow velocities. This thesis offers insight into the requirements and important design parameters for a volume-based strategy to achieve its full potential, as well as encountered challenges.

Despite the improvements, this strategy on its own cannot solve all limitations imposed by poor solubility in aqueous electrolytes and such systems will continue to suffer from low reagent availability at high current densities in larger electrolyzers. This can be mitigated by increasing the channel thickness to reach an even larger electrolyte volume, operating at higher pressures

when working with dissolved gases, or employing in-channel saturation methods and altered cell designs.

All in all, the principle of volume-based electrodes can be employed to boost the achievable current density to a limited but promising extent in a wide variety of mass transfer limited systems, such as CO₂ reduction and oxygen reduction as demonstrated in this thesis. This strategy can be applied in a similar manner in other applications such as fuel cells[6], or in nitrogen[7] and NO_x[8] reduction to ammonia, by adapting the electrode material. This provides an alternate and innovative route towards intensifying electrochemical processes in relatively simple and robust scalable systems that provide green alternatives to environmentally unfriendly industrial processes.

REFERENCES

- [1] G. J. Doornbusch, J. E. Dykstra, P. M. Biesheuvel, and M. E. Suss. “Fluidized bed electrodes with high carbon loading for water desalination by capacitive deionization”. In: *Journal of Materials Chemistry A* 4.10 (2016), pp. 3642–3647.
- [2] *Aritech - RVC Carbon Foam*. URL: <https://rvcfoams.com/product/rvc-carbon-foam/>.
- [3] *ERG - Carbon (RVC) Foam*. URL: <https://ergaerospace.com/carbon-rvc-foam-open-cell-material/>.
- [4] Liang Huang, Ge Gao, Chaobo Yang, Xiao-Yan Li, Rui Kai Miao, Yanrong Xue, Ke Xie, Pengfei Ou, Cafer T. Yavuz, Yu Han, Gaetano Magnotti, David Sinton, Edward H. Sargent, and Xu Lu. “Pressure dependence in aqueous-based electrochemical CO₂ reduction”. In: *Nature Communications* 14.1 (2023), p. 2958.
- [5] H. Rajaei, A. Rajora, and J. W. Haverkort. “Design of membraneless gas-evolving flow-through porous electrodes”. In: *Journal of Power Sources* 491 (2021), p. 229364.
- [6] Franz B. Spingler, Adam Phillips, Tobias Schuler, Michael C. Tucker, and Adam Z. Weber. “Investigating fuel-cell transport limitations using hydrogen limiting current”. In: *International Journal of Hydrogen Energy* 42.19 (2017), pp. 13960–13969.
- [7] Hengyuan Liu, Yingzhe Liu, Xude Yu, Xintong Huang, Jingwei Zhang, Zhuo Chen, and Jianhong Xu. “A Novel Bubble-based Microreactor for Enhanced Mass Transfer Dynamics toward Efficient Electrocatalytic Nitrogen Reduction”. In: *Small* 20.14 (2024), p. 2309344.
- [8] Harish Reddy Inta, Dinesh Dhanabal, Sridhar Sethuram Markandaraj, and Sangaraju Shanmugam. “Recent advances in electrocatalytic NO_x reduction into ammonia”. In: *EES Catalysis* 1.5 (2023), pp. 645–664.

SUMMARY

The negative environmental effects of large-scale use of fossil fuels, chemicals, and energy-intensive processes are forcing us to develop green alternatives to mitigate the climate crisis. Electrochemistry, powered by renewable energy, provides us with a direct way to produce precursors or materials from green electricity and benign reagents such as water, carbon dioxide (CO₂), or oxygen. A widely known example is water electrolysis to produce hydrogen as a green fuel and chemical building blocks for other chemicals. Alternatively, CO₂ can be fed to an electrolyzer to produce sustainable carbon-based materials - such as pharmaceuticals, paints, and synthetic fuels - that are otherwise obtained from fossil fuels. Electrochemistry is therefore a versatile and promising technology that could provide a strong foundation for sustainable alternatives to various environmentally unfriendly processes.

Because electrochemical systems are often studied as replacements for well-established and optimized industrial processes, the benchmarks to achieve an economically viable and competitive status are high. Most importantly, the processes must be efficient with materials and energy, resulting in requirements such as high current density, energy efficiency and product selectivity. These are hampered in many systems by poor solubility of reagents in water, such as the aforementioned CO₂ and oxygen. The low reagent concentration results in reagent depletion, intensified competition with parasitic side reactions, and low selectivity at industrially relevant current densities. Such systems are severely limited by the slow mass transport and availability of reagents towards and at the electrode surface.

In this thesis, we study the potential and limitations of volume-based electrodes to alleviate mass transfer limitations and boost limiting currents in aqueous systems with poorly soluble reagents. Extending the electrode into the electrolyzer channel improves the contact with the electrolyte and dissolved reagent, and expands the reaction volume to raise the amount of available reagent. The use of volume-based electrodes, with a large surface area, leads to lower local current densities, lower reagent depletion, and allows for higher total geometric current densities. We used two types of volume-based electrodes: 1) a flow-through (foam-based), and 2) a flow-with (suspension-based) electrode, which each offer their own advantages and challenges.

Chapter 2 studies the influence of electrical, morphological, and rheological properties on the applicability of a flow-with configuration in CO₂ electrolyzers. Theoretical modelling showed that the reaction is most evenly spread over the channel volume when the charge transfer resistance is significantly larger than the solid and liquid phase resistances, or of a similar magnitude. In contrast, the reaction will be localized and the advantage of the volume-based electrode will be lost if the charge transfer resistance is smaller than the solid and liquid phase resistances. Although this chapter considers suspension electrodes, these results are also relevant for flow-through configurations. We experimentally obtained resistance values, using electrical impedance spectroscopy, in suspensions electrodes with carbon loadings that are realistic for use in flow-with electrolyzers. Entering this data into the model showed that the criteria regarding the charge transfer, solid and liquid phase resistances to realize a homogeneous reaction distribution can be met in suspensions of activated carbon (AC) and carbon black (CB), but not in suspensions of spherical glassy carbon (GC) particles. Finally, assessing the relation between the electrical and rheological properties of suspensions of the differently shaped particles showed that the AC particles are the most promising for use in suspension electrodes.

Despite these positive results, the suspension electrode materials were found to interfere negatively with the desired process in the CO₂ electrolyzer, as well as in an oxygen reduction system. The large surface area and metal contaminations on the highly porous carbon microparticles appear to catalyze the hydrogen evolution reaction to such an extent that mostly hydrogen is formed and only low partial current densities for CO (2-3 mA/cm²) could be reached in the CO₂ electrolyzer. Similarly, the AC material causes disproportionation of all H₂O₂ produced during the oxygen reduction experiments on suspension electrodes. The chemical properties and purity of the suspension material prove to be critical for maintaining good catalytic selectivity and the positive impact of using a volume-based electrode.

Chapter 3 shows that replacing the carbon suspension material with a lower surface area and more conductive flow-through current collector significantly decreases the intensity of the hydrogen evolution reaction. The CO current density was increased even further to >50 mA/cm² by adding surfactants to moderate particle aggregation. The surfactants are suspected to also protect the catalyst surfaces from degradation and to promote bubble removal, preventing blockage of pores and enhancing bubble-induced mass transfer.

Chapter 4 compares both the flow-through and flow-with configurations with a flow-by system during electrochemical oxygen reduction and studies how the configurations affect mass transfer. The flow-through electrode boosted the limiting current density by a factor of 10-25 compared to the flow-by configuration. In addition to having a large and easily accessible surface area, the porous structure of the flow-through electrode alleviates mass transfer limitations by disrupting the development of a thick diffusion boundary layer and improves mass transfer already at low flow velocities. As expected from Sherwood correlations, increasing the flow velocity further does not increase the limiting current density much further inside the laminar flow regime typical for electrochemical systems. The effect of increased flow velocity is stronger in flow-by systems, but significantly less than changing the electrode configuration to a flow-through system. Therefore, more can be gained from optimizing the electrode design than from increasing the flow velocity.

Despite the ability of flow-through electrodes to alleviate mass transfer limitations on the microscale, aqueous systems will still be limited on the macroscale by poor solubility when scaling up to larger electrolyzers with longer electrodes. Logically, boosting the current density is paired with increased reagent consumption and eventual depletion further on in the channel, even in the bulk. Additional strategies should be applied to keep the bulk concentration sufficiently high through the entire length of the channel, for example by increasing the flow rate, increasing the pressure, or combining with an in-channel gas feed.

Chapter 5 examines the diffusion boundary layer around a particle electrode with fluorescence lifetime imaging microscopy (FLIM) and studies the influence of current density and flow velocity on the local reaction environment. We perform water electrolysis as a proxy for other electrochemical conversion reactions and consider the regions with high pH as regions that are prone to reagent depletion and product buildup. Increasing the current density at low flow velocities causes significant plume formation and an unfavorable reaction environment for any electrode element placed inside the plume region. Increasing the flow rate along with the current density is a good strategy to dissipate the plume over a shorter length scale and prevent affecting the performance of other electrode elements that are placed in close proximity. Alternatively the electrode design should incorporate large enough pores or suspension particle spacing to mitigate this effect. Overall, this chapter demonstrates how the current density, flow rate, and electrode design can be adjusted to improve the local reaction conditions.

Fitting a self-discharge model for electric double layer capacitors (EDLCs) to the discharge curve of a single capacitive particle, representing a suspension electrode particle, showed that the capacitance can drive a Faradaic reaction after contact with a current source is broken. The charging potential can be optimized to maximize the Faradaic contribution and to avoid the diffusion-

limited regime and other voltage dissipation processes such as charge redistribution.

In conclusion, this thesis shows the potential and limitations of volume-based electrodes in mass transfer-limited electrochemical system. A homogeneous reaction distribution can be achieved for both flow-through and flow-with configurations. The volume-based electrodes can be adjusted for different applications by selecting a suitable electrode material. The suspension electrodes have proven more challenging on this account than the flow-through configuration, at least for the conversion of CO_2 and O_2 , due to promotion of competing reactions. Any type of foam-based electrode can be incorporated into a flow channel to provide a suitable flow-through electrode for a wide variety of applications. Despite the ability of volume-based electrodes to alleviate mass transfer limitations on the microscale, reagent depletion remains a challenge on the macroscale in aqueous-based systems. In such cases, volume-based electrodes can still provide an improvement in terms of boosting the geometrical current density, but should likely be combined with other strategies to prevent reagent depletion higher up in the channel.

SAMENVATTING

Omwille van de klimaatcrisis zullen we het gebruik van fossiele brandstoffen, chemicaliën, en energie-intensieve processen fors moeten terugdringen en milieuvriendelijke alternatieven moeten ontwikkelen. Elektrochemie stelt ons in staat om synthetische materialen te produceren vanuit groene energie en onschadelijke stoffen, zoals water, kooldioxide (CO₂), en zuurstof. Een bekend voorbeeld hiervan is de productie van waterstof door middel van waterelektrolyse. De geproduceerde waterstof kan vervolgens gebruikt worden als duurzame brandstof, of als bouwsteen voor andere chemicaliën. Op dezelfde manier kan ook CO₂ door elektrolyse omgezet worden om precursors voor duurzame koolstofhoudende materialen – zoals medicijnen, verf, en synthetische brandstoffen – te produceren die momenteel uit fossiele brandstoffen gewonnen worden. De veelzijdigheid van elektrochemie maakt het een veelbelovende basis voor duurzame alternatieven voor een groot scala aan vervuilende processen.

Omdat elektrochemische systemen meestal ontwikkeld worden als vervanging voor reeds geoptimaliseerde industriële processen, zijn de vereisten om een proces economisch rendabel en competitief te maken behoorlijk hoog. Efficiënt gebruik van materialen en energie zijn hierin van groot belang, wat resulteert in een noodzaak voor goed functioneren op hoge stroomdichtheden, hoge efficiëntie in energieverbruik, en hoge selectiviteit naar het gewenste product. Dit is echter problematisch in vele systemen waarin reactanten gebruikt worden die zeer beperkt oplosbaar zijn in water, zoals CO₂ en zuurstof. De lage concentraties leiden tot snelle reactant depletie, versterkte competitie met nevenreacties, en verlaagde selectiviteit op de stroomdichtheden die relevant zijn voor industriële toepassing. Zulke systemen worden ernstig gelimiteerd door traag massatransport en de beperkte beschikbaarheid van reactanten aan het elektrode-oppervlak.

In dit proefschrift onderzoeken we de potentie en de limitaties van volume-elektroden in het verminderen van de limitaties door traag massatransport en het verhogen van de maximaal haalbare stroomdichtheid in elektrochemische systemen met elektrolyten op waterbasis en slecht oplosbare reactanten. Het uitbreiden van de elektrode naar het volledige vloeistof kanaal bevordert het contact met het elektrolyt en de opgeloste reactant, en vergroot zo het volume waar de reactie plaats kan vinden en de hoeveelheid beschikbaar reactant. Het gebruik van volume-elektroden met een groot contactoppervlak verlaagt de lokale stroomdichtheid, vermindert reactant depletie, en maakt zo het gebruik van hogere totale stroomdichtheden mogelijk. We maken gebruik van twee typen volume-elektroden: 1) flow-through (poreuze matrix), en 2) flow-with (suspensie) elektroden, die beiden hun eigen voordelen en uitdagingen meebrengen.

In hoofdstuk 2 wordt het belang van elektrische, morfologische, en rheologische eigenschappen voor de toepasbaarheid van de flow-with configuratie in CO₂ elektrolyse onderzocht. Uit modellering blijkt dat de reactie het meest gelijkmatig wordt uitgespreid over het volledige volume van het kanaal wanneer de weerstand tegen ladingsoverdracht significant hoger is dan de elektrische weerstanden van de vaste en vloeibare fasen, of van vergelijkbare grootte. In tegenstelling zal de reactie gelokaliseerd blijven als de ladingsoverdrachtsweerstand lager is dan de weerstanden van de vaste en vloeibare fasen. In deze situatie worden de beoogde voordelen van de volume-elektrode niet benut. Hoewel dit hoofdstuk toegespitst is op suspensie elektroden zijn deze inzichten ook relevant voor flow-through configuraties. We hebben weerstandswaarden in suspensie elektrodes met voor CO₂ elektrolyse relevante koolstofgehalten experimenteel verkregen door middel van elektrochemische impedantie spectroscopie. Het gebruik van deze waarden in het model heeft uitgewezen dan de criteria rondom de weerstand tegen ladingsoverdracht, en

de weerstand in de vaste en vloeibare fasen behaald kunnen worden in suspensies van activated carbon (AC) en carbon black (CB), maar niet in suspensies van glassy carbon (GC) deeltjes. Tenslotte bleek uit evaluatie van de relatie tussen de elektrische en rheologische eigenschappen van alle suspensies dat de AC deeltjes de meest gunstige eigenschappen hebben voor het gebruik in suspensie elektrodes.

Toch bleken de materialen in de suspensie elektroden CO₂ en zuurstof elektrolyse negatief te beïnvloeden. Het grote oppervlak van de poreuze koolstofdeeltjes en aanwezige metallische verontreinigingen blijken de waterstofevolutie reactie dermate te katalyseren dat er voornamelijk waterstof werd geproduceerd, waardoor slechts een lage gedeeltelijke stroomdichtheid naar de productie van CO (2-3 mA/cm²) kon worden gerealiseerd tijdens CO₂ reductie. Daarbij veroorzaakte het AC materiaal de disproportioneerende van geproduceerde waterstof peroxide (H₂O₂) tijdens de zuurstofreductie experimenten met suspensie elektroden. De chemische eigenschappen en zuiverheid van het suspensiemateriaal zijn dus essentieel voor het behouden van hoge katalytische selectiviteit en de positieve impact van het gebruik van volume-elektroden.

Hoofdstuk 3 laat zien dat het vervangen van de koolstofmateriaal in suspensie door een beter geleidende flow-through elektrode met een kleiner oppervlak de intensiteit van de waterstof evolutie reactie significant verlaagt. De partiële CO stroomdichtheid kon vervolgens nog verder verhoogd worden naar >50 mA/cm² door oppervlakte-actieve stoffen toe te voegen die aggregatie van katalytische suspensiedeeltjes tegengaan. Vermoedelijk beschermen deze oppervlakte-actieve stoffen het katalysatoroppervlak ook tegen degradatie, en versnellen ze de verwijdering van bubbels waardoor poriën minder vaak geblokkeerd worden en extra massatransport door bubbelstromen wordt bevorderd.

In hoofdstuk 4 vergelijken we de flow-through en flow-with configuraties met een flow-by systeem voor elektrochemische zuurstofreductie en bestuderen we hoe de elektrodeconfiguratie massatransport beïnvloedt. De flow-through configuratie verhoogde de maximale stroomdichtheid met een factor 10-25 ten opzichte van de flow-by configuratie. Naast dat de flow-through elektrode een groter en makkelijk te bereiken elektrode-oppervlak heeft, vermindert de poreuze structuur van de flow-through elektrode de massatransportlimitatie ook door de ontwikkeling van een dikke diffusiegrenslaag te verstoren. Dit effect is al te zien op lage stroomsnelheden. Zoals verwacht van Sherwood-relaties neemt de maximale stroomdichtheid niet veel verder toe met een verhoging van de stroomsnelheid binnen het laminaire stromingsregime wat relevant is voor elektrochemische systemen. Het verhogen van de stroomsnelheid heeft echter meer invloed in de flow-by systeem, maar aanzienlijk minder dan het wijzigen van elektrode-configuratie naar een flow-through systeem. Daarom is er meer winst te behalen door het elektrodeontwerp te optimaliseren dan door de stroomsnelheid te verhogen.

Alhoewel flow-through elektroden de massatransportlimitatie op microschaal kunnen verminderen, zullen watergebaseerde systemen op de macroschaal alsnog gelimiteerd worden door lage oplosbaarheid als er gebruik gemaakt wordt van grotere elektrolytische cellen met langere elektrodes. Dit komt doordat het verhogen van de stroomdichtheid gepaard gaat met een verhoogde consumptiesnelheid van reactanten, die uiteindelijk verder in het kanaal en zelfs in de bulk van het elektrolyt uitgeput zullen worden. Aanvullende strategieën zullen dan toegepast moeten worden om de bulk-concentratie voldoende hoog te houden over de gehele lengte van het kanaal. Dit kan bijvoorbeeld door de stroomsnelheid of druk te verhogen, of door de volume-elektrode te combineren met een extra gastoevoer binnenin het kanaal.

In hoofdstuk 5 bekijken we de diffusiegrenslaag rond een deeltjes-elektrode door middel van fluorescence lifetime imaging microscopy (FLIM), en onderzoeken we het effect van de stroomdichtheid en stroomsnelheid op de lokale reactiecondities. We gebruiken water elektrolyse als een proxy voor andere elektrochemische conversiereacties en beschouwen de gebieden waar zich een hoge pH ontwikkelt als gebieden die gevoelig zijn voor reactant depletie en productophoping. Het

verhogen van de stroomdichtheid op lage stroomsnelheden leidt tot de formatie van een aanzienlijke pluim van elektrolyt met een verhoogde pH en dus een ongunstige reactieomgeving voor eventuele andere elektrode-elementen die in dit gebied geplaatst worden. Het mee-verhogen van de stroomsnelheid is een goede methode om de pluim over een kleinere lengteschaal te doen verdwijnen en te voorkomen dat andere elektrode-elementen die zich dichtbij bevinden hier negatief door beïnvloed worden. Als alternatief kunnen er grotere poriën, of grotere afstanden tussen de suspensiedeeltjes, in de elektrode geïntegreerd worden. Over het geheel genomen toont dit hoofdstuk hoe de stroomdichtheid, stroomsnelheid, en het elektrode-ontwerp gebruikt kunnen worden om lokale reactiecondities te verbeteren.

Het fitten van een zelf-ontladingsmodel voor elektrische dubbellaagscondensatoren (EDLCs) aan een ontladings-curve van het enkele capacitieve deeltje, wat een deeltje in een suspensie-elektrode vertegenwoordigt, toonde aan dat de capaciteit een Faradische reacties enige tijd kan aandrijven nadat het contact met een stroombron is verbroken. Het oplaadpotentiaal kan geoptimaliseerd worden om de Faradische bijdrage te maximaliseren, en daarbij het diffusie-gelimiteerde regime te vermijden en andere ontladingsprocessen zoals ladingsredistributie te voorkomen.

Ter conclusie behandelt dit proefschrift de potentie en de limitaties van volume-elektroden in massatransport-gelimiteerde elektrochemische systemen. Flow-through en flow-with elektroden kunnen beiden een homogene reactiedistributie opleveren, en kunnen afgestemd worden op verschillende toepassing door een passend elektrodemateriaal te selecteren. Suspensie-elektroden blijken hierin meer uitdagingen mee te brengen voor toepassing in elektrochemische conversie CO₂ en zuurstof dan flow-through elektroden vanwege concurrerende nevenreacties. Vele soorten poreuze elektroden kunnen gemakkelijk geïntegreerd worden in stromingskanalen om een geschikte flow-through elektrode te creëren voor een breed scala aan toepassingen. Ondanks het vermogen van volume-elektrodes om de beperkingen door massatransport op de microschaal te verlichten, zal depletie van reactanten op de macroschaal een uitdaging blijven en zal dit nog steeds overwogen moeten worden in watergebaseerde elektrochemische cellen. In deze gevallen kunnen volume-elektrodes alsnog verbetering opleveren met betrekking tot het verhogen van de geometrische stroomdichtheid, maar zullen naar alle waarschijnlijkheid gecombineerd moeten worden met andere methoden om uitputting van reactanten hoger in het kanaal te voorkomen.

ACKNOWLEDGEMENTS

Completing this thesis has been a great challenge and would not have been possible without the help of many people. I want to thank you all for your valuable contributions!

First of all, I thank my promotors **David** and **Johan** for all of their time, feedback, and discussions. Thank you for standing by me during these four years of learning and research. David, thank you for helping me explore the world of chemical engineering. Your insights and feedback always helped me to push the research one step further. I always enjoyed your creativity, whether it was related to any scientific topic we were discussing or a silly pun you came up with. Johan, you started out as the most involved co-promotor I have ever heard of and you are now very well deserved officially appointed as promotor. Thank you for always being kind and supportive with your positive attitude, and for guiding me through all kinds of crazy estimations and calculations with unequaled enthusiasm and interest.

I also want to thank the members of my PhD defence committee. **Prof. dr. Valeria Garbin**, **Prof. dr. ir. Ruud van Ommen**, **Dr. Ruud Kortlever**, **Prof. dr. Volker Presser**, and **Dr. Ben Erné** thank you for your interest in my thesis and for taking part in this committee.

A special thank you goes to the students who joined me on this carbon adventure. Thank you **Laura** for being my very first student and starting Team Slurry together. I had just started the project when you joined and we both had a lot to learn at that point, but we got through it successfully and we had the best time. **Xiao**, thank you for your hard work in making so many beautiful nanoparticles and microscopy images, and for doing so with such a positive attitude. It was a joy to work with you. Thank you **Martijn** for being brave enough to work with carbon suspensions during your first-ever laboratory project. I don't think you ever managed to guess both of my middle names, I'm sure you can find them somewhere in this thesis though. **Mohammed**, **Gerard**, and **Julius**, you made a great team as the Particle Peeps. Thank you for your efforts during your projects and for continuing to help me after you had already graduated. I learned a lot from all of you and I greatly enjoyed working with you.

Thank you to the **Electrochemical Flow Systems (EFS)** group for all the ideas, discussions, and relaxed working atmosphere: **Ai-Yu**, **Rose**, **Minu**, **Aron**, **Matthäa**, and **Andrey**. **Kaustub**, I was so happy to make beautiful colours with you in the lab. **Lorenz**, thank you for making the electrolyzer setup and for being an example of true productivity. Thank you **Kosta**, **Vojtěch**, **Jan-Willem** and **Yu-Fan** for creating a fun and relaxed atmosphere in the office through your jokes and the occasional round of office olympics. **Jan-Willem**, thank you for never tiring of my questions about FTV and COMSOL. Thank you **Marijn** for setting up the EFS socials together, and **Christel** for continuing this with me. I enjoyed writing (and mostly chatting) with you during our Socials meetings and making our EFS page a success. Fittingly, I am sure you sent me the most reels of anyone, ever. Thank you **Jorrit** for completing this trajectory alongside me with the biggest smile and so many homemade cookies. And to both Christel and Jorrit, thank you for your enthusiasm at being my paranymphs. I greatly appreciate your help throughout the whole PhD trajectory, right up to the defence.

I also want to thank the Delft University of Technology and the Department of Chemical Engineering their hospitality and fun activities throughout the years. And a special thank you to the **Transport Phenomena (TP)** group for providing a good working environment with plenty of lively discussions during the weekly seminar. Thank you **Sandra** for organizing all the fun TP activities throughout the years and for keeping the group well-organized and running smoothly.

Thank you to all the technicians for the help in the lab. **Stefan**, thank you for getting things done so quickly. Even in busy times, you would always help me within a few days. **Kevin**, thank you for making the most beautiful slurry flow cell. It is the only design I could run without clogging almost immediately. Thank you **Christiaan** for helping me with anything I could come up with and doing that with such a positive attitude.

Phebe and **Dennis**, it has been a joy to work with you and to visit your electrochemistry lab. It was very valuable to gain insights from a different perspective and university.

Thank you **Tom** for always making time when I needed someone to talk to, for cheering me on, and for boosting my confidence when I needed it.

Bedankt **Gerard, Mariska, Pjotr, Yannick, Adrie, Ida, opa Cees** en **oma Sophie**, en vrienden voor alle leuke momenten, etentjes, kopjes koffie, en de morele steun.

Léon, de afgelopen jaren waren vol pieken en dalen, maar samen is het ons gelukt. Bedankt voor alle mooie momenten en je onvoorwaardelijke steun.

*Nathalie
Leiden, January, 2025*

CURRICULUM VITÆ

Nathalie Elsa Gertrude LIGTHART

- 1995 Born in Leiden, The Netherlands.
- 2014–2017 **B.Sc. Chemistry**
Department of Chemistry
Utrecht University, The Netherlands
- 2017–2020 **M.Sc. Nanomaterials Science**
Department of Chemistry
Utrecht University, The Netherlands
- 2020–2024 **PhD. Chemical Engineering**
Transport Phenomena
Department of Chemical Engineering
Faculty of Applied Sciences
Delft University of Technology, The Netherlands
Thesis: Volume-based electrodes for enhancing limiting currents in electrochemical conversion reactions
Promotor: Prof. dr. ir. J. T. Padding
Promotor: Dr. ir. D. A. Vermaas
- 2024–present **Data Analyst**
Stedin, The Netherlands

LIST OF PUBLICATIONS

7. **Nathalie E. G. Ligthart***, Julius Sommer*, Jorrit Bleeker, Lorenz M. Baumgartner, Johan T. Padding, David A. Vermaas, *Imaging local pH at boundary layers in electrochemical flow systems with complex shapes*, submitted for publication. (* Shared co-first authorship)
6. **Nathalie E. G. Ligthart**, Mohammed Khan, Johan T. Padding, David A. Vermaas, *3D current collectors enable partial current densities beyond 50 mA/cm² in aqueous CO₂ electrolysis*, submitted for publication.
5. Phebe H. van Langevelde, **Nathalie E. G. Ligthart**, Pim G. J. van Duren, David A. Vermaas, Dennis G. H. Hetterscheid, *Molecular electrocatalysts facilitate H₂O₂ synthesis at a large scale in flow cells using gas diffusion electrodes*, in preparation for publication.
4. **Nathalie E. G. Ligthart**, Phebe H. van Langevelde, Johan T. Padding, Dennis G. H. Hetterscheid, David A. Vermaas, *20-Fold increased limiting currents in oxygen reduction with Cu-tmpa by replacing flow-by with flow-through electrodes*, *ACS Sustainable Chemistry & Engineering* **12**, 12909-12918 (2024).
3. **Nathalie E. G. Ligthart**, Gerard Prats Vergel, Johan T. Padding, David A. Vermaas, *Practical Potential of Suspension Electrodes for Enhanced Limiting Currents in Electrochemical CO₂ Reduction*, *Energy Advances* **3**, 841-853 (2024).
2. Ruben W. Verweij, Pepijn G. Moerman, Loes P. P. Huijnen, **Nathalie E. G. Ligthart**, Indrani Chakraborty, Jan Groenewold, Willem K. Kegel, Alfons van Blaaderen, Daniela J. Kraft, *Conformations and diffusion of flexibly linked colloidal chains*, *Journal of Physics: Materials* **4**, 035002 (2021).
1. Ruben W. Verweij*, Pepijn G. Moerman*, **Nathalie E. G. Ligthart**, Loes P. P. Huijnen, Jan Groenewold, Willem K. Kegel, Alfons van Blaaderen, Daniela J. Kraft, *Flexibility-induced effects in the Brownian motion of colloidal trimers*, *Physical Review Research* **2**, 033136 (2020). (* Shared co-first authorship)

